



**Forschungszentrum  
Dresden Rossendorf**



**TECHNISCHE  
UNIVERSITÄT  
DRESDEN**

# **Magnetostatics and Dynamics of Ion Irradiated NiFe/Ta Multilayer Films Studied by Vector Network Analyzer Ferromagnetic Resonance**

**D I S S E R T A T I O N**

**zur Erlangung des akademischen Grades**

**Doctor rerum naturalium  
(Dr. rer. nat.)**

**vorgelegt**

**der Fakultät Mathematik und Naturwissenschaften  
der Technischen Universität Dresden**

**von**

**Dipl.-Phys. Daniel Markó**

**geboren am 12.12.1981 in Sebnitz**

**Eingereicht am 17.08.2010**

Die Dissertation wurde in der Zeit von 12/2006 bis 06/2010 im Institut für Ionenstrahlphysik und Materialforschung am Forschungszentrum Dresden-Rossendorf e.V. angefertigt.

1. Gutachter: Prof. Dr. J. Faßbender, Forschungszentrum Dresden-Rossendorf e.V.
2. Gutachter: Prof. Dr. J. Wosnitza, Forschungszentrum Dresden-Rossendorf e.V.

Datum der Verteidigung: 25.11.2010

## Abstract

In the present work, the implications of ion irradiation on the magnetostatic and dynamic properties of soft magnetic Py/Ta (Py = Permalloy:  $\text{Ni}_{80}\text{Fe}_{20}$ ) single and multilayer films have been investigated with the main objective of finding a way to determine their saturation magnetization. Both polar magneto-optical Kerr effect (MOKE) and vector network analyzer ferromagnetic resonance (VNA-FMR) measurements have proven to be suitable methods to determine  $\mu_0 M_S$ , circumventing the problem of the unknown effective magnetic volume that causes conventional techniques such as SQUID or VSM to fail. Provided there is no perpendicular anisotropy contribution in the samples, the saturation magnetization can be determined even in the case of strong interfacial mixing due to an inherently high number of Py/Ta interfaces and/or ion irradiation with high fluences.

Another integral part of this work has been to construct a VNA-FMR spectrometer capable of performing both azimuthal and polar angle-dependent measurements using a magnet strong enough to saturate samples containing iron. Starting from scratch, this comprised numerous steps such as developing a suitable coplanar waveguide design, and writing the control, evaluation, and fitting software.

With both increasing ion fluence and number of Py/Ta interfaces, a decrease of saturation magnetization has been observed. In the case of the  $10\times$ Py samples, an immediate decrease of  $\mu_0 M_S$  already sets in at small ion fluences. However, for the  $1\times$ Py and  $5\times$ Py samples, the saturation magnetization remains constant up to a certain ion fluence, but then starts to rapidly decrease. Ne ion irradiation causes a mixing and broadening of the interfaces. Thus, the Py/Ta stacks undergo a transition from being polycrystalline to amorphous at a critical fluence depending on the number of interfaces. The saturation magnetization is found to vanish at a Ta concentration of about 10–15 at.% in the Py layers. The samples possess a small uniaxial anisotropy, which remains virtually unaffected by the ion fluence, but slightly reduces with an increasing number of Py/Ta interfaces.

In addition to magnetostatics, the dynamic properties of the samples have been investigated as well. The Gilbert damping parameter  $\alpha$  increases with both increasing number of Py/Ta interfaces and higher ion fluences, with the former having a stronger influence. The inhomogeneous linewidth broadening  $\Delta B_0$  increases as well with increasing number of Py/Ta interfaces, but slightly decreases for higher ion fluences.



## Kurzfassung

In dieser Dissertation ist der Einfluss von Ionenbestrahlung auf die magnetostatischen und dynamischen Eigenschaften von weichmagnetischen Py/Ta-Einzel- und Multilagen (Py = Permalloy:  $\text{Ni}_{80}\text{Fe}_{20}$ ) untersucht worden, wobei das Hauptziel gewesen ist, eine Methode zur Bestimmung der Sättigungsmagnetisierung zu finden. Sowohl polare magneto-optische Kerr-Effektmessungen (MOKE) als auch ferromagnetische Resonanzmessungen mittels eines Vektornetzwerkanalysators (VNA-FMR) haben sich als geeignet erwiesen, um  $\mu_0 M_S$  zu bestimmen, wobei das Problem des unbekanntes effektiven magnetischen Volumens umgangen wird, welches bei der Verwendung von Techniken wie SQUID oder VSM auftreten würde. Unter der Voraussetzung, dass die Proben keinen senkrechten magnetischen Anisotropiebeitrag besitzen, kann die Sättigungsmagnetisierung selbst im Fall starker Grenzflächendurchmischung infolge einer großen Anzahl an Py/Ta-Grenzflächen und/oder Ionenbestrahlung mit hohen Fluenzen bestimmt werden.

Ein weiterer wesentlicher Bestandteil dieser Arbeit ist die Konstruktion eines VNA-FMR-Spektrometers gewesen, welches vollautomatisiert ist, polare und azimutale Winkelabhängigkeiten messen kann und einen Magneten besitzt, der Proben, die Eisen beinhalten, sättigen kann. Von Grund auf beginnend umfasste dies zahlreiche Schritte wie z. B. die Entwicklung eines geeigneten koplanaren Wellenleiterdesigns sowie das Schreiben von Steuerungs-, Auswertungs- und Fitprogrammen.

Mit steigender Fluenz und Zahl an Py/Ta-Grenzflächen ist eine Abnahme der Sättigungsmagnetisierung beobachtet worden. Im Fall der  $10\times$ Py-Proben findet diese bereits bei kleinen Fluenzen statt. Im Gegensatz dazu bleibt  $\mu_0 M_S$  der  $1\times$ Py- und  $5\times$ Py-Proben bis zu einer bestimmten Fluenz konstant, bevor sie sich dann umso schneller verringert. Die Bestrahlung mit Ne-Ionen verursacht eine Durchmischung und Verbreiterung der Grenzflächen. Infolgedessen erfahren die Py/Ta-Proben bei einer kritischen Fluenz, die von der Zahl der Grenzflächen abhängig ist, einen Phasenübergang von polykristallin zu amorph. Die Sättigungsmagnetisierung verschwindet ab einer Ta-Konzentration von etwa 10–15 Atom-% in den Py-Schichten. Die Proben besitzen eine kleine uniaxiale Anisotropie, die praktisch unbeeinflusst von der Fluenz ist, sich jedoch mit steigender Zahl an Py/Ta-Grenzflächen leicht verringert.

Neben den statischen sind auch die dynamischen magnetischen Eigenschaften der Proben untersucht worden. Der Gilbert-Dämpfungsparameter  $\alpha$  erhöht sich sowohl mit steigender Zahl an Py/Ta-Grenzflächen als auch mit höheren Fluenzen, wobei Erstere einen größeren Einfluss hat. Die inhomogene Linienverbreiterung  $\Delta B_0$  nimmt ebenfalls mit steigender Zahl an Py/Ta-Grenzflächen zu, verringert sich jedoch bei größeren Fluenzen leicht.



# Contents

<b>Abstract</b>	<b>iii</b>
<b>Kurzfassung</b>	<b>v</b>
<b>List of Figures</b>	<b>x</b>
<b>List of Tables</b>	<b>xi</b>
<b>1 Introduction and Motivation</b>	<b>1</b>
<b>2 Theory of Magnetostatics and Dynamics in Ferromagnets</b>	<b>5</b>
2.1 Magnetic Interactions . . . . .	5
2.1.1 Exchange Interaction . . . . .	5
2.1.2 Spin-Orbit Interaction . . . . .	6
2.1.3 Magnetic Dipolar Interaction . . . . .	6
2.2 Energetics of a Ferromagnet . . . . .	7
2.2.1 Exchange Energy . . . . .	7
2.2.2 Zeeman Energy . . . . .	8
2.2.3 Magnetic Anisotropy Energy . . . . .	8
2.2.4 Demagnetizing Energy . . . . .	10
2.3 Magnetization Dynamics . . . . .	12
2.3.1 Equation of Motion . . . . .	12
2.3.2 Dynamic Susceptibility . . . . .	15
2.3.3 Smit and Beljers Formulation . . . . .	18
2.3.4 Magnetic Excitations . . . . .	21
2.3.5 Magnetization Damping . . . . .	22
<b>3 Basics of Microwave Engineering</b>	<b>25</b>
3.1 Theory of Transmission Lines . . . . .	25
3.1.1 The Telegrapher's Equations . . . . .	25
3.1.2 Characteristic Impedance . . . . .	27
3.1.3 Propagation Constant . . . . .	27
3.2 Propagation Modes of Electromagnetic Waves . . . . .	28
3.3 Types of Transmission Lines . . . . .	28
3.3.1 Coaxial Line . . . . .	29
3.3.2 Coplanar Waveguide . . . . .	30
3.4 Network Analysis . . . . .	33
3.4.1 Two-Port Networks . . . . .	33

3.4.2	Scattering Parameters . . . . .	33
3.4.3	Scattering Transmission Parameters . . . . .	36
3.5	Vector Network Analyzer . . . . .	38
3.5.1	Introduction . . . . .	38
3.5.2	Principle of Operation . . . . .	38
3.5.3	Calibration and Error Correction . . . . .	40
<b>4</b>	<b>The Experimental VNA-FMR Setups</b>	<b>43</b>
4.1	Conventional Ferromagnetic Resonance . . . . .	43
4.2	Vector Network Analyzer Ferromagnetic Resonance . . . . .	44
4.3	Construction and Components of the VNA-FMR Spectrometers . . . . .	44
4.3.1	Magnet Systems . . . . .	45
4.3.2	Coplanar Waveguides . . . . .	47
4.3.3	Sample Holders for Angle-Dependent Measurements . . . . .	51
4.3.4	Automation and Control Software . . . . .	53
<b>5</b>	<b>Data Evaluation: From S-Parameters to Magnetic Susceptibility</b>	<b>55</b>
5.1	Full Two-Port Data Evaluation . . . . .	55
5.1.1	Raw Data: S-Parameter . . . . .	55
5.1.2	Correction of Sample Position . . . . .	57
5.1.3	De-embedding . . . . .	58
5.1.4	Extraction of Reflection Coefficient and Propagation Constant . . . . .	59
5.1.5	Calculation of Permittivity and Permeability . . . . .	59
5.2	Evaluation Software . . . . .	62
5.3	Other Evaluation Methods . . . . .	62
5.3.1	Methods only using $S_{21}$ . . . . .	62
5.3.2	Methods only using $S_{11}$ . . . . .	64
5.4	Accuracy of the Different Evaluation Methods . . . . .	64
<b>6</b>	<b>Magnetostatics and Dynamics of Ion Irradiated Py/Ta Multilayers</b>	<b>65</b>
6.1	Sample Preparation and Composition . . . . .	66
6.2	Structural Investigation and Simulation of the Interfacial Mixing . . . . .	66
6.3	Static Magnetic Characterization . . . . .	68
6.4	Dynamic Magnetic Characterization . . . . .	71
6.5	Linewidth and Damping . . . . .	74
6.6	Conclusion . . . . .	75
<b>7</b>	<b>Summary and Outlook</b>	<b>77</b>
	<b>Bibliography</b>	<b>79</b>
	<b>Publications</b>	<b>89</b>
	<b>Acknowledgements</b>	<b>93</b>



# List of Figures

1.1 An Ancient Compass from China . . . . .	1
2.1 Demagnetizing Field for In- and Out-of-Plane Magnetization . . . . .	11
2.2 Undamped and Damped Precessional Motion . . . . .	13
2.3 Calculated Example of the Complex Dynamic Susceptibility $\chi_{yy}$ . . . . .	17
2.4 Spherical Coordinate System . . . . .	19
2.5 Uniform FMR Mode and Spin Wave Mode . . . . .	21
2.6 Schematic Representation of Relaxation Processes . . . . .	22
3.1 Transmission Line Model . . . . .	26
3.2 Components and TEM Mode Field Pattern of a Coaxial Cable . . . . .	29
3.3 Geometry and Field Pattern of a Coplanar Waveguide . . . . .	31
3.4 Black-Box Representation of a Two-Port Device . . . . .	34
3.5 S-Parameter Definition of a Two-Port Network . . . . .	35
3.6 Cascade Connection of Two Two-Port Networks . . . . .	37
3.7 Fundamental Architecture of a VNA . . . . .	39
3.8 Two-Port Error Correction Model . . . . .	41
4.1 VNA-FMR Spectrometers constructed within this Thesis . . . . .	45
4.2 Magnet System of VNA-FMR Setup 2 . . . . .	46
4.3 CPWs employed in the two VNA-FMR Setups . . . . .	48
4.4 Transmission Parameters of CPW Type 1 . . . . .	50
4.5 Reflection Parameters of CPW Type 1 . . . . .	50
4.6 Front and Rear View of the Polar Sample Holder . . . . .	52
4.7 Sample Holder for Azimuthal Measurements . . . . .	52
4.8 Screenshot of the Control Software of VNA-FMR Setup 2 . . . . .	53
5.1 CPW loaded with a Magnetic Sample. . . . .	56
5.2 Comparison of a Measured and a De-embedded Transmission Parameter. . . . .	58
5.3 Effective Permeability and Dynamic Susceptibility of a Py/Ru/Co Trilayer . . . . .	60
5.4 Influence of the Sample Length on the Dynamic Susceptibility . . . . .	61
5.5 Screenshots of the VNA-FMR Data Evaluation Software . . . . .	63
6.1 Structure of the Py/Ta Stacks . . . . .	66
6.2 Cross-sectional TEM Images of Selected Py/Ta Samples . . . . .	67
6.3 TRIDYN Simulations of the Effect of Ion Irradiation . . . . .	69
6.4 Easy Axis and Hard Axis Hysteresis Loops of Selected Py/Ta Samples . . . . .	70
6.5 Frequency Dependence of the Resonance Field of the Py/Ta Samples . . . . .	71
6.6 Angle-dependent FMR Measurements of an Irradiated $1 \times \text{Py}$ Sample . . . . .	72

6.7 Saturation Magnetization of the Py-Ta Samples . . . . .	73
6.8 Frequency and Field Linewidth of the Py-Ta Samples . . . . .	75

# List of Tables

3.1 S- and T-Matrices of Selected Circuit Components. . . . .	38
6.1 Saturation Magnetization and Anisotropy Field of the Py/Ta Samples . .	73
6.2 Damping Parameter and Linewidth Broadening of the Py/Ta Samples . .	75



# 1 Introduction and Motivation

The first historical mention of magnetism dates back to about 800 BC, when Greek philosopher Thales of Miletus reflected upon the wondrous property of magnetite, the magnetic iron ore  $\text{Fe}_3\text{O}_4$  and famed lodestone, to attract other pieces of the same material and iron [1]. The name magnet may refer to the district of Magnesia in the southeast of Thessaly, Greece where it is believed that the first lodestone was mined. Lodestone was also known in China at that time, where it was called “love stone”. The very first magnetic device, the compass (see Fig. 1.1), was invented by the Chinese most likely during the Qin dynasty (221–206 BC) who used it for navigation by the 12th century [2].



**Fig. 1.1:** A primitive, ancient compass from China consisting of a spoon-shaped magnetic object with a smooth bottom, set on a polished copper surface. When pushed, it rotated freely and usually came to rest with the handle pointing to the South. It was likely used first to orient buildings and later to navigate.

Since then, the technological importance of magnetic materials has grown to such a great extent, that they have become an indispensable part of our daily life. Magnetic materials are used ubiquitously nowadays in fields as diverse as, e.g., electrical energy transport, high-power electro-motors and generators, telecommunication systems, navigation equipment, aviation and space operations, micromechanical automation, medicine, magnetocaloric refrigeration, and high density magnetic recording.

Particularly the latter has made tremendous progress over the past two decades and is one of few areas, in which ground-breaking, fundamental discoveries and inventions are commercially used within shortest time. Among the examples are the exploitation of the giant magnetoresistance (GMR) effect [3, 4] in hard disk drives as well as magnetic tunnel junctions (MTJs) [5–7] for magnetic random access memory (MRAM) [8].

The effect used for magnetic storage of binary information is the magnetic anisotropy, which is connected to an energy barrier between two opposite orientations of the magnetization representing “0” and “1”. This energy, called magnetic anisotropy energy, is given by the product  $K_u V$ , where  $K_u$  is the anisotropy constant and  $V$  the volume of a group of grains of the recording media storing one bit. High anisotropy media are required in order to further decrease the volume of the grains and thus to increase the areal density, but also to prevent thermally excited magnetization reversals. However, as the switching field  $H_c$  is proportional to  $K_u$  and inversely proportional to the saturation magnetization  $M_S$ , a high value of  $K_u$  implies higher writing fields [9]. Therefore, possibilities to engineer or tailor the magnetic anisotropy down to the nanoscale are essential.

With the introduction of and the increasing demand for ultrafast magnetic devices such as MRAM, the investigation of magnetic damping processes has also significantly gained scientific interest. In order to optimize precessional magnetization switching, a systematic control of the magnetic damping parameter is of utmost importance.

The magnetic properties of ultrathin metallic films and multilayers, as they are used in spin valves, MTJs, and recording media, often depend strongly on their surface and interface structure. Moreover, chemical composition, crystallinity, grain sizes and their distribution govern the magnetic behavior. All these structural properties can be modified by light-ion irradiation in an energy range of 5–150 keV [10].

In 1998, Chappert *et al.* [11] first reported on the modification of magnetic properties in magnetic thin films and multilayers by means of ion irradiation. Since then, this technique has been applied to a wide range of materials covering soft and hard magnetic systems as well as amorphous, crystalline, or epitaxial films. However, the underlying physical mechanisms are always a local energy deposition, vacancy creation, or change in the atomic composition. Examples of ion-induced modifications include magnetic anisotropies [12, 13], magnetic damping [14], exchange bias, interlayer exchange coupling [15–18], and phase-transitions [19].

Typically, the entire sample is irradiated and thus its integral magnetic properties are modified. However, it is also possible to only irradiate specific areas by using lithographically produced masks, which allows to pattern magnetic properties on various length scales. In this way, thin film structures exhibiting magnetic properties neither present in non-implanted nor in homogeneously implanted films can be realized [13, 20]. For reviews on magnetic patterning by means of ion irradiation and implantation, see Refs. [10, 21].

Many of the magnetic properties modified by ion irradiation can be investigated by ferromagnetic resonance (FMR), a technique particularly suited for the high-frequency characterization of magnetic thin films and multilayers. From the angular, the frequency, and the temperature dependence of the resonance field and the linewidth, not only anisotropies and damping properties, but also interlayer exchange coupling as well as numerous other material parameters can be extracted [22]. In addition to the uniform mode, FMR also allows to study fundamental magnetic excitations such as spin waves.

In recent years, a modern version of FMR, the so-called vector network analyzer ferromagnetic resonance (VNA-FMR), has evolved, which quickly gained popularity.

---

In contrast to conventional FMR, this novel technique employs a high-bandwidth coplanar waveguide (CPW) to generate the magnetic excitation field instead of a microwave cavity limited to a fixed resonance frequency. This allows for measurements not only in field-swept mode as in conventional FMR, but also in frequency-swept mode across a frequency range of typically several tens of GHz. The latter is particularly advantageous for investigating samples whose magnetic domain state should be conserved. Furthermore, broadband measurements of the resonance linewidth are imperative to separate intrinsic from extrinsic damping contributions [23]. Another interesting aspect of VNA-FMR is the possibility to investigate arrays of micron-sized elements such as dots, rings, or ellipses, which can be directly patterned on the CPW [24–32].

The aims of this Ph.D. thesis were to build such a broadband VNA-FMR spectrometer, which included its mechanical and electrical construction, elaborating the CPW design as well as writing control and evaluation software, and to investigate the magnetostatic and dynamic properties of ion irradiated NiFe/Ta thin film and multilayer systems.

The present Ph.D. thesis is organized as follows:

**Chapter 2** provides the necessary theoretical background for the understanding of ferromagnetic resonance measurements. It starts with the interactions and the corresponding energies in ferromagnets. In the following, various types of the equation of motion of the magnetization are introduced, from which the resonance conditions and the dynamic susceptibility, the quantity measured with FMR, are derived. Moreover, magnetic excitations will be treated and finally, magnetic damping processes are discussed.

**Chapter 3** is devoted to some fundamental aspects of microwave engineering. Apart from the theory of electromagnetic propagation and the characteristic quantities for its description, the two types of transmission lines used within this thesis are discussed. Furthermore, the concept of network analysis is introduced and the mode of operation of a VNA is explained.

In **Chapter 4** the mainly employed experimental technique, VNA-FMR, is presented. The chapter begins with a comparison of conventional FMR and VNA-FMR. In the following, an extensive description of the two VNA-FMR spectrometers built within this thesis is given.

**Chapter 5** is dedicated to the data evaluation and describes all the necessary steps for the conversion of the measured two-port S-parameters into the dynamic magnetic susceptibility. Furthermore, alternative evaluation methods are briefly discussed and a comparison of their accuracy is given.

In **Chapter 6** the implications of ion irradiation on the magnetic properties of NiFe/Ta single and multilayers are discussed. It is shown that ion irradiation affects the magnetic properties in the same way as splitting up the single NiFe layer into several NiFe multilayers separated by Ta spacers and thus increasing the number of NiFe/Ta interfaces. With both increasing number of interfaces and increasing ion fluence, a decrease of saturation magnetization and an increase of damping is observed. Moreover, it is shown that it is possible to determine the saturation

magnetization of these samples from polar magneto-optical Kerr effect (MOKE) and VNA-FMR measurements, which is inaccessible by conventional magnetometry.

The thesis closes with a summary and an outlook on future experiments is given.



# 2 Theory of Magnetostatics and Dynamics in Ferromagnets

This chapter provides the necessary theoretical background for the understanding of ferromagnetic resonance measurements. It starts with the interactions and the corresponding energies in ferromagnets. In the following, various types of the equation of motion of the magnetization are introduced, from which the resonance conditions and the dynamic susceptibility, the quantity measured with FMR, are derived. Moreover, magnetic excitations will be treated and finally, magnetic damping processes are discussed.

## 2.1 Magnetic Interactions

*Ferromagnets* are materials in which elementary, permanent magnetic moments below a critical temperature, the *Curie temperature*  $T_C$ , spontaneously align. The interactions giving rise to this spontaneous alignment, namely the exchange, spin-orbit, and dipolar interactions will be discussed in this section.

### 2.1.1 Exchange Interaction

The exchange interaction is the result of the interplay between the Coulomb energy and the Pauli exclusion principle. The latter states that two fermions cannot occupy the same quantum state simultaneously, i.e., have an identical set of quantum numbers. For a two-electron system this is accomplished by an antisymmetric form of its total wave function. As a consequence, the Coulomb energy of two electrons differs for a parallel or antiparallel alignment of their spins  $\mathbf{s}_i$  and  $\mathbf{s}_j$ , with the former case having a lower energy. In the Heisenberg model, the corresponding exchange energy for an assembly of  $N$  spins is given by [33]

$$E_{\text{ex}} = - \sum_{i \neq j}^N J_{ij} \mathbf{s}_i \cdot \mathbf{s}_j = -2 \sum_{i < j}^N J_{ij} \mathbf{s}_i \cdot \mathbf{s}_j, \quad (2.1)$$

where  $J_{ij}$  is the exchange integral. In the case of  $J_{ij} > 0$ , the energy minimum is attained by a parallel alignment of the spins which corresponds to ferromagnetic ordering. For  $J_{ij} < 0$  an antiparallel alignment of the spins is energetically favorable leading to antiferromagnetic ordering. In general,  $J_{ij}$  is negative, which is why there are only few elemental ferromagnets near room temperature, namely Ni, Fe, Co, and Gd.

Since the exchange integral depends on the degree of overlap between the single-electron wave functions,  $J_{ij}$  generally decreases very rapidly with the separation of the spins  $\mathbf{s}_i$  and  $\mathbf{s}_j$ . Therefore, only nearest-neighbor terms are considered in the summation of Eq. (2.1). Despite being rather short-range, the exchange interaction is the largest magnetic interaction with a magnitude in the order of  $10^{-2}$  eV. As a consequence, it is the origin of the long-range, spontaneous magnetic ordering and accounts for the alignment of the permanent magnetic moments below a critical temperature. As the exchange integral is independent of the relative alignment of the electrons, the exchange energy is isotropic and leads to a homogeneous magnetization of the material.

### 2.1.2 Spin-Orbit Interaction

Each electron  $i$  in a given atom possesses an orbital angular momentum  $\mathbf{l}_i$  and a spin angular momentum  $\mathbf{s}_i$ , which in turn give rise to an orbital magnetic moment  $\mu_l$  and a spin magnetic moment  $\mu_s$ . By means of Coulomb energy and exchange interaction the spins of individual electrons couple to a resultant spin  $\mathbf{S} = \sum_i \mathbf{s}_i$  and their individual orbital momenta to a resultant orbital momentum  $\mathbf{L} = \sum_i \mathbf{l}_i$ . The role of the spin-orbit interaction is to couple  $\mathbf{L}$  and  $\mathbf{S}$  to a new total angular momentum  $\mathbf{J} = \mathbf{L} + \mathbf{S}$  which becomes a conserved quantity. This so-called *Russell–Saunders* or *L–S coupling* scheme leads to an energetic splitting of the electron states which for hydrogen-like atoms is given by [33]

$$E_{\text{LS}} = -\frac{Z^4 e^2}{8\pi\epsilon_0 m_e^2 c^2 r^3} \mathbf{L} \cdot \mathbf{S}, \quad (2.2)$$

where  $Z$  is the atomic number and  $\mathbf{L}$  and  $\mathbf{S}$  are in units of  $\hbar$ . The magnitude of the energy splitting due to the spin-orbit interaction is of the order of  $10^{-5}$  to  $10^{-3}$  eV and is thus considerably weaker than the exchange energy.

If the orbital of an electron is not spherically symmetric, the energy of the state will depend on the orientation of the angular magnetic moments with respect to the crystal lattice. For an orbital moment that prefers to lie along a specific bonding or crystallographic axis, the energy given by Eq. (2.2) then corresponds to the difference between the favored ( $\mathbf{L} \parallel \mathbf{S}$ ) and unfavored ( $\mathbf{L} \perp \mathbf{S}$ ) spin directions. This orientation-dependent energy, which reflects the same symmetry as the crystal, is called *magneto-crystalline anisotropy* (MCA) and is the very result of the spin-orbit coupling. Moreover, spin-orbit coupling represents a path for energy transfer between the spin and lattice system, which is essential for intrinsic magnetic damping.

### 2.1.3 Magnetic Dipolar Interaction

The long-range magnetic dipolar interaction describes the direct interaction between a magnetic dipole  $\boldsymbol{\mu}_i$  and the magnetic field  $\mathbf{H}_j$  generated by another dipole  $\boldsymbol{\mu}_j$ . The

corresponding energy is given by

$$E_{\text{dip}} = - \sum_{i < j} \boldsymbol{\mu}_i \cdot \mathbf{H}_j = \frac{\mu_0}{4\pi r_{ij}^3} \sum_{i < j} \left[ \boldsymbol{\mu}_i \cdot \boldsymbol{\mu}_j - \frac{3}{r_{ij}^2} (\boldsymbol{\mu}_i \cdot \mathbf{r}_{ij})(\boldsymbol{\mu}_j \cdot \mathbf{r}_{ij}) \right]. \quad (2.3)$$

This expression indicates that the energy is lowest when the moment is aligned with the magnetic field. As it decreases with  $r^3$ , the magnetic dipolar interaction is the weakest of all three magnetic interactions with typical values of the order of  $10^{-6}$  to  $10^{-5}$  eV for two neighboring atomic moments. The importance of the magnetic dipolar interaction lies mainly in the possibility to align the magnetization of a ferromagnet along its energetically unfavored hard axis by overcoming the spin-orbit coupling, which determines the MCA. In addition, the magnetic dipolar interaction leads to effects such as spin waves and demagnetizing field.

## 2.2 Energetics of a Ferromagnet

The alignment of the magnetization in a ferromagnet is determined by its striving towards the state with the lowest energy. For a static magnetization distribution to be at equilibrium, the torque exerted on  $\mathbf{M}$  by the effective magnetic field  $\mathbf{H}_{\text{eff}}$  must vanish everywhere:

$$\mathbf{M} \times \mathbf{H}_{\text{eff}} = 0. \quad (2.4)$$

$\mathbf{H}_{\text{eff}}$  is comprised of the applied external and demagnetizing fields as well as fields originating from exchange interaction and anisotropy. The effective magnetic field, which is derived from the variation of the total energy density  $\epsilon_{\text{tot}} = E_{\text{tot}}/V$  in a ferromagnetic volume element  $V$  with respect to the normalized magnetization  $\mathbf{m}(\mathbf{r}) = \mathbf{M}(\mathbf{r})/M_S$ , is given by

$$\mathbf{H}_{\text{eff}} = - \frac{1}{\mu_0 M_S} \frac{\partial \epsilon_{\text{tot}}}{\partial \mathbf{m}}. \quad (2.5)$$

In the following, the several contributions to the total energy  $E_{\text{tot}}$  of a magnetic system, namely the magnetic anisotropy energy  $E_{\text{ani}}$ , the demagnetizing energy  $E_{\text{dem}}$ , the exchange energy  $E_{\text{ex}}$ , and the Zeeman energy  $E_{\text{zee}}$  will be discussed with emphasis on the first two.

### 2.2.1 Exchange Energy

An equivalent form of the exchange energy given by Eq. (2.1) can be derived from the continuum approximation. Instead of considering the individual spins of the atoms, this approach describes the local average of the spin magnetic moments by the magnetization  $\mathbf{M}(\mathbf{r})$ . Assuming that the magnitude of the magnetization, the saturation magnetization  $M_S$ , remains constant, a normalized magnetization  $\mathbf{m}(\mathbf{r}) = \mathbf{M}(\mathbf{r})/M_S$  with  $|\mathbf{m}| = 1$  is introduced. The exchange energy is then given

by [34]

$$E_{\text{ex}} = A \int (\nabla \mathbf{m})^2 dV = A \int [(\nabla m_x)^2 + (\nabla m_y)^2 + (\nabla m_z)^2] dV, \quad (2.6)$$

where

$$m_x = \frac{M_x}{M_S}, \quad m_y = \frac{M_y}{M_S}, \quad m_z = \frac{M_z}{M_S}, \quad (2.7)$$

are the components of the normalized magnetization  $\mathbf{m}(\mathbf{r})$  along the three crystallographic/coordinate axes.  $A$ , the exchange constant, is a macroscopic measure for the coupling stiffness of the spin system. It is a material constant, is generally temperature-dependent, and is related to the exchange integral  $J$  by

$$A = \frac{2nJ\mathbf{S}^2}{a^2}, \quad (2.8)$$

where  $a$  is the lattice constant and  $n$  is the number of sites per unit cell. Literature values for the exchange stiffness constant of the ferromagnets Ni, Fe, and Co are  $A_{\text{Ni}} = 0.8 \times 10^{-11}$  J/m [35],  $A_{\text{Fe}} = 2.0 \times 10^{-11}$  J/m [36], and  $A_{\text{Co}} = 3.0 \times 10^{-11}$  J/m [37], respectively.

### 2.2.2 Zeeman Energy

The interaction of the magnetization  $\mathbf{M}$  with a uniform or spatially varying external magnetic field  $\mathbf{H}_{\text{ext}}$  is described by the Zeeman energy

$$E_{\text{zee}} = -\mu_0 \int_V \mathbf{M} \cdot \mathbf{H}_{\text{ext}} dV. \quad (2.9)$$

In analogy with the exchange energy, this energy is minimized by a parallel alignment of the magnetization in the direction of the external magnetic field.

### 2.2.3 Magnetic Anisotropy Energy

As mentioned in the first section of this chapter, the spin-orbit coupling gives rise to the *magneto-crystalline anisotropy*, which describes the preference of the magnetization  $\mathbf{M}$  to lie along one or several major crystallographic axes. The energy required to rotate  $\mathbf{M}$  from an easy axis to a hard axis, which correspond to a minimum and maximum of energy, respectively, is called magnetic anisotropy energy  $E_{\text{ani}}$ .

Uniaxial anisotropy can result from stress, from epitaxial growth of thin films, or from an anisotropic crystal structure such as in hcp Co, and is characterized by the presence of a single easy or hard axis. Since the uniaxial anisotropy energy  $E_{\text{Ku}}$  must not be affected by reversing  $\mathbf{M}$  along the anisotropy axis, it must be a function of

even powers of the angle  $\vartheta$  enclosed by  $\mathbf{M}$  and a unique axis of the sample,

$$E_{\text{Ku}} = \sum_i K_{2i\parallel} \sin^{2i} \vartheta, \quad (2.10)$$

where  $K_{2i\parallel}$  are the anisotropy constants of unit  $[\text{J}/\text{m}^3]$ . Rarely more than the first two significant terms have to be considered, since on the one hand the magnitude of the anisotropy constants generally strongly decreases with higher order and on the other hand thermal fluctuations of the spins tends to average out these contributions. This simplifies Eq. (2.10) to

$$E_{\text{Ku}} = K_{2\parallel} \sin^2 \vartheta + K_{4\parallel} \sin^4 \vartheta, \quad (2.11)$$

where  $K_{0\parallel}$  has been omitted as it is independent of the orientation of  $\mathbf{M}$  and thus has no meaning for the anisotropy. Large positive values of  $K_{2\parallel}$  lead to an easy axis perpendicular to the surface, whereas large negative values of  $K_{2\parallel}$  give rise to an easy plane perpendicular to the anisotropy axis. For intermediate values, i.e., under the condition  $0 > K_{2\parallel}/K_{4\parallel} > -2$ , the magnetization preferably aligns along a cone around the anisotropy axis. Uniaxial anisotropies can be very strong, reaching up to several  $10^7 \text{ J}/\text{m}^3$  for rare-earth transition metals [34]. Literature values for Co at room temperature [38] are  $K_{2\parallel} = 4.1 \times 10^5 \text{ J}/\text{m}^3$  and  $K_{4\parallel} = 1.5 \times 10^5 \text{ J}/\text{m}^3$ , indicating a preference for magnetization along the  $z$  axis. It is often convenient to express the anisotropy energy in terms of the magnetization components as defined by Eq. (2.7), which then gives

$$E_{\text{Ku}} = K_{2\parallel}(1 - m_z^2) + K_{4\parallel}(1 - m_z^4). \quad (2.12)$$

The effect of the magnetic anisotropy can be modeled by introducing an effective anisotropy field  $\mathbf{H}_{\text{Ku}}$ , since the presence of a magnetic field also causes an orientation-dependent energy. Using Eq. (2.5) and only taking into account the lowest-order anisotropy term, it can be calculated as

$$\mathbf{H}_{\text{Ku}} = \frac{2K_{2\parallel}}{\mu_0 M_S} \sin \theta \mathbf{e}_z. \quad (2.13)$$

$\mathbf{H}_{\text{ku}}$  corresponds to the external magnetic field needed to rotate the magnetization from the easy to the hard axis. Therefore, the same expression can be obtained by equating Eq. (2.9) and (2.12).

In cubic magnetic materials such as fcc Ni or bcc Fe, the anisotropy energy must be invariant under the interchange of any two axes due to the symmetry of the crystal. In terms of the components of the normalized magnetization, the two lowest-order contributions to the corresponding cubic anisotropy energy  $E_{\text{Kc}}$  can be expressed as

$$E_{\text{Kc}} = K_{c1} (m_x^2 m_y^2 + m_x^2 m_z^2 + m_y^2 m_z^2) + K_{c2} (m_x^2 m_y^2 m_z^2). \quad (2.14)$$

Using the trigonometric functions of spherical coordinates, Eq. (2.14) can then be

written as

$$E_{Kc} = (K_{c1} + K_{c2} \sin^2 \vartheta) \cos^4 \vartheta \sin^2 \phi \cos^2 \phi + K_{c1} \sin^2 \vartheta \cos^2 \vartheta. \quad (2.15)$$

At room temperature,  $K_{c1} = 4.8 \times 10^4 \text{ J/m}^3$  and  $K_{c2} = -1.0 \times 10^4 \text{ J/m}^3$  for Fe, whereas  $K_{c1} = -4.5 \times 10^3 \text{ J/m}^3$  and  $K_{c2} = -2.3 \times 10^3 \text{ J/m}^3$  for Ni [38]. For  $K_{c1} > 0$  the  $\langle 100 \rangle$  axes, i.e. the cube edges, are the easy axes of magnetization. In the case of  $K_{c1} < 0$ , the  $\langle 111 \rangle$  axes, i.e., the body diagonals, are the easy axes of magnetization.

Apart from the volume anisotropies described above, there is another anisotropic energy term, which only occurs in very thin films and multilayers of these, the so-called surface anisotropy energy. Owing to missing bonds, an incompletely quenched orbital moment, and a reduced symmetry, the magnetic anisotropy at the surface of a ferromagnet substantially differs from the bulk. In the case of a structurally isotropic sample, the surface anisotropy energy  $E_s$  can be expressed to second order as

$$E_s = \frac{1}{t} (K_{s1} m_z^2 + K_{s2} m_z^4), \quad (2.16)$$

where  $t$  is the thickness of the film. Depending on the sign of  $K_{s1}$ , a magnetization perpendicular to the surface ( $K_{s1} < 0$ ) or in the plane of the surface ( $K_{s1} > 0$ ) is favored. The order of magnitude of  $K_s$  ( $10^{-4}$  to  $10^{-3} \text{ J/m}^3$ ) is often much larger than the values obtained from multiplying regular anisotropy constants with the thickness of a single atomic layers [34].

## 2.2.4 Demagnetizing Energy

The long-range magnetic dipolar interaction is the source of another magnetic anisotropy called *shape anisotropy*, which is typically much smaller than the *magneto-crystalline anisotropy*. It leads to a non-local energy contribution, which is connected to the magnetic field generated by a magnetic sample itself. By combining the Maxwell equation

$$\nabla \cdot \mathbf{B} = 0 \quad (2.17)$$

with the relation

$$\mathbf{B} = \mu_0 (\mathbf{H} + \mathbf{M}) \quad (2.18)$$

to

$$\nabla \cdot \mathbf{H} = -\nabla \cdot \mathbf{M}, \quad (2.19)$$

it can be seen that the divergence of the magnetization  $\mathbf{M}$  generates a magnetic field  $\mathbf{H}$ . Inside the magnetic material, this field is called *demagnetizing field*  $\mathbf{H}_d$  because it is oriented opposite to  $\mathbf{M}$ . Outside the material, this field reflects the *stray field*  $\mathbf{H}_s$  as it loops around the sample. The demagnetizing energy, given by

$$E_d = -\frac{1}{2} \int_V \mathbf{H}_d \cdot \mathbf{M} \, dV, \quad (2.20)$$

is always positive as  $\mathbf{H}_d$  is opposed to  $\mathbf{M}$ .

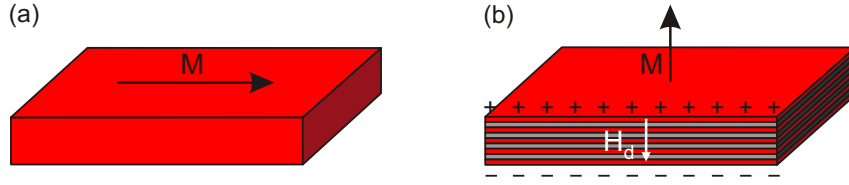


**Fig. 2.1:** (a) In magnetic films with a thickness of several nanometers the easy magnetization direction is typically in-plane due to the dominance of the magneto-static or shape anisotropy. Since the surface charges located on the left and right edges of the sample are far apart, the demagnetizing field  $\mathbf{H}_d$  in this configuration can be neglected. (b) In multilayer systems, consisting of alternating magnetic and nonmagnetic layers of subnanometer thickness, such as Co and Au, the easy axis may be out-of-plane due to the dominance of the spin-orbit derived magneto-crystalline anisotropy. In this case, magnetic charges at the top and bottom film surfaces generate a strong demagnetizing field  $\mathbf{H}_d$  inside the magnetic material oriented opposite to the magnetization  $\mathbf{M}$ .

Since the demagnetizing field depends on the shape of the magnetic sample as well as the symmetry of the crystal and is generally not homogeneous over the whole sample, its calculation is mostly difficult. However, in the case of a uniformly magnetized ellipsoid it can be expressed as

$$\mathbf{H}_d = -\overset{\leftrightarrow}{N} \mathbf{M}, \quad (2.21)$$

where  $\overset{\leftrightarrow}{N}$  is the dimensionless demagnetizing tensor. When orienting the coordinate system along the principal axes of the ellipsoid,  $\overset{\leftrightarrow}{N}$  can be diagonalized and is given by

$$\overset{\leftrightarrow}{N} = \begin{pmatrix} N_x & 0 & 0 \\ 0 & N_y & 0 \\ 0 & 0 & N_z \end{pmatrix}. \quad (2.22)$$

Its non-zero elements  $N_x, N_y,$  and  $N_z$  with  $N_x + N_y + N_z = 1$  are the demagnetizing factors. They are dependent on the ratios of the axes of the ellipsoid  $a, b,$  and  $c$  and can be calculated numerically or analytically.

The particular case of an infinitely extended thin film, which represents a good approximation of an oblate, i.e., disc-shaped, ellipsoid, is illustrated in Fig. 2.1. With the  $z$  axis pointing perpendicular to the film plane, the demagnetizing factors are  $N_x = N_y = 0$  and  $N_z = 1$ . For in-plane magnetization (Fig. 2.1a), the magnitude of the demagnetizing field  $\mathbf{H}_d$  is nearly zero due to the infinitely separated boundaries. However, for out-of-plane magnetization (Fig. 2.1b), the magnetic poles at the surfaces lead to a maximum demagnetizing field

$$\mathbf{H}_d = -M_S (m_z \cdot \mathbf{e}_z). \quad (2.23)$$

The corresponding demagnetizing energy is given by

$$E_d = \frac{M_S^2}{2} \int_V m_z^2 dV \quad (2.24)$$

and has the form of a uniaxial anisotropy energy. The minimization of the demagnetizing or stray field energy is also the driving factor for the formation of magnetic domains.

## 2.3 Magnetization Dynamics

The key difference between magnetostatics and dynamic magnetic phenomena is the timescale on which stimulus and response of a magnetic system occur. Under the influence of quasi-static magnetic fields, the magnetization always seems to be in equilibrium, since dynamic processes take place on the nanosecond timescale or even faster. However, when applying short magnetic pulses or alternating magnetic fields, the magnetization configuration is disturbed from its equilibrium. Particularly interesting is the process called ferromagnetic resonance (FMR), in which the magnetization is resonantly excited by rf or microwave fields, whose frequency matches the resonance frequency of the magnetic system. In combination with a static magnetic field applied perpendicular to the excitation field, this leads to a precessional motion of the magnetization. The energy required to sustain the precession is absorbed from the microwave radiation. The underlying physical concepts and the theoretical description of FMR as well as the dynamic response of the magnetization are illustrated in this section.

### 2.3.1 Equation of Motion

The equation of motion of the magnetization can best be derived from a semiclassical treatment. In this case, the motion of an electron in an atomic orbital under the influence of a magnetic field can be considered as a small current loop with a magnetic moment

$$\mathbf{m} = IAn\mathbf{n}, \quad (2.25)$$

where  $\mathbf{n}$  is the unit vector perpendicular to the area  $A$  enclosed by the loop and  $I$  is the current in the loop. The magnetic moment is connected to the total angular momentum by

$$\mathbf{m} = \gamma\mathbf{J}, \quad (2.26)$$

where the constant of proportionality  $\gamma$ , which is referred to as *gyromagnetic ratio*, is given by

$$\gamma = \frac{g|e|\hbar}{2m_e}. \quad (2.27)$$

$g$  is called *Landé  $g$  factor* and has the value of approximately 2 for pure spin and 1 for pure angular momenta. For mixtures of  $\mathbf{L}$  and  $\mathbf{S}$ , it takes on other values



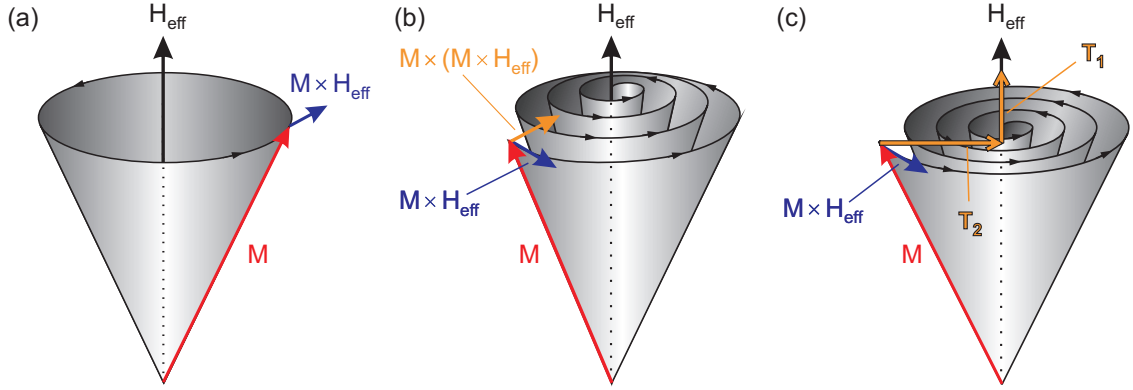


**Fig. 2.2:** (a) Undamped precession of the magnetization  $\mathbf{M}$  around the effective magnetic field  $\mathbf{H}_{\text{eff}}$ . (b) When introducing Gilbert-type damping, the magnetization follows a spiral trajectory to its equilibrium position where it becomes aligned with  $\mathbf{H}_{\text{eff}}$ . (c) Bloch-Bloembergen damping with two independent dissipation processes characterized by the relaxation times  $T_1$  and  $T_2$ .

representing the projection of  $\mathbf{m}$  along the direction of  $\mathbf{J}$ . Since the rate of change of the total angular momentum  $d\mathbf{J}/dt$  is proportional to the torque  $\mathbf{m} \times \mathbf{B}_{\text{eff}}$ , the equation of motion for a single magnetic moment can be written as

$$\frac{d\mathbf{m}}{dt} = \gamma\mu_0\mathbf{m} \times \mathbf{H}_{\text{eff}}, \quad (2.28)$$

where the relation  $\mathbf{B}_{\text{eff}} = \mu_0\mathbf{H}_{\text{eff}}$  has been used. The effective magnetic field  $\mathbf{H}_{\text{eff}}$  is introduced in order to account for exchange, anisotropy, and dipolar fields acting on the magnetic moment in addition to the external field  $\mathbf{H}_{\text{ext}}$ . Since a magnetic system typically consists of a large number of atoms, whose magnetic moments are coupled via exchange interaction, the sum over all magnetic moments in the volume can be expressed by the magnetization  $\mathbf{M}$ . This leads to the classical equation of motion

$$\frac{d\mathbf{M}}{dt} = -\gamma\mu_0\mathbf{M} \times \mathbf{H}_{\text{eff}}, \quad (2.29)$$

which describes the precession of the magnetization  $\mathbf{M}$  around the direction of the effective magnetic field  $\mathbf{H}_{\text{eff}}$ , as shown in Fig. 2.2a. Assuming the magnetic field to be time-independent, multiplying Eq. (2.29) successively by  $\mathbf{M}$  and  $\mathbf{H}_{\text{eff}}$  leads to

$$\frac{d}{dt}[\mathbf{M}]^2 = 0, \quad \frac{d}{dt}[\mathbf{M} \cdot \mathbf{H}_{\text{eff}}] = 0. \quad (2.30)$$

Eq. (2.30) states that the modulus of the magnetization remains unchanged during motion and that the angle between  $\mathbf{M}$  and  $\mathbf{H}_{\text{eff}}$  remains constant as a function of time. According to Eq. (2.29), once the magnetization is misaligned, it is never able to reach the lowest energy configuration with  $\mathbf{M}$  parallel to  $\mathbf{H}_{\text{eff}}$ . However, this does not correspond to the experimental observation showing that the magnetization aligns after finite time in the direction of the effective field, i.e.,  $\mathbf{M}$  reaches its equilibrium

position. Therefore, an additional damping torque, which is perpendicular to the precessional torque and perpendicular to  $\mathbf{M}$ , has to be added to the right-hand side of Eq. (2.29). One possible choice introduced by Landau and Lifshitz in 1935 [39] is a term proportional to  $-\mathbf{M} \times (\mathbf{M} \times \mathbf{H}_{\text{eff}})$ :

$$\frac{d\mathbf{M}}{dt} = -\gamma\mu_0\mathbf{M} \times \mathbf{H}_{\text{eff}} - \frac{\lambda}{M_S^2}\mathbf{M} \times (\mathbf{M} \times \mathbf{H}_{\text{eff}}). \quad (2.31)$$

The prefactor of the damping term contains the phenomenologically introduced damping constant  $\lambda$ , which corresponds to the inverse of the relaxation time  $\tau$ . Equation (2.31) is known as the Landau-Lifshitz (LL) equation.

An alternative form of Eq. (2.31), referred to as the Landau-Lifshitz-Gilbert (LLG) equation, has been proposed by Gilbert in 1955 [40]:

$$\frac{d\mathbf{M}}{dt} = -\gamma\mu_0\mathbf{M} \times \mathbf{H}_{\text{eff}} + \frac{G}{\gamma M_S^2} \left( \mathbf{M} \times \frac{d\mathbf{M}}{dt} \right). \quad (2.32)$$

It consists of the same precessional term as the LL equation, but contains a modified dissipation term. The latter models a viscous damping, which is proportional to the time derivative of the magnetization and introduces the Gilbert damping parameter  $G$ . In modern literature, it is most common to indicate the dimensionless damping parameter  $\alpha = G/\gamma M_S$ . The effect of damping is illustrated in Fig. 2.2b. The motion of the magnetization follows a spiral trajectory until it becomes aligned with the effective magnetic field at which point both the precessional and the damping torque acting on  $\mathbf{M}$  vanish. As in the case of the LL equation, the magnitude of the magnetization remains constant. If both  $\lambda$  and  $\alpha$  are small so that the direction of  $d\mathbf{M}/dt$  is only slightly perturbed by the presence of the damping term, the Landau-Lifshitz and Gilbert forms are mathematically equivalent. However, when large damping is considered, profound differences arise between the two forms [41, 42]. The LL equation results in

$$\frac{d\mathbf{M}}{dt} \rightarrow \infty \quad \text{for} \quad \lambda \rightarrow \infty, \quad (2.33)$$

whereas the LLG equation yields

$$\frac{d\mathbf{M}}{dt} \rightarrow 0 \quad \text{for} \quad \alpha \rightarrow \infty. \quad (2.34)$$

As the behavior described by the LL equation is physically implausible, this form of the equation of motion is only valid in the case of small damping. In contrast, the LLG equation reflects the proper physics for both small and large damping and should therefore be used preferably. Moreover, it is mathematically more convenient with respect to the separation of longitudinal and transversal components of the magnetization  $\mathbf{M}$  as it will be shown in the following subsection.

A third form to describe the damped motion of the magnetization has been proposed by Bloch and Bloembergen (BB) in 1946 [43, 44] and was originally used

for nuclear magnetic resonance. The corresponding BB equation is given by

$$\frac{d\mathbf{M}}{dt} = -\gamma\mu_0\mathbf{M} \times \mathbf{H}_{\text{eff}} - \frac{M_x}{T_2}\mathbf{e}_x - \frac{M_y}{T_2}\mathbf{e}_y - \frac{M_z - M_S}{T_1}\mathbf{e}_z, \quad (2.35)$$

where the equilibrium direction of the magnetization is aligned with the  $z$ -axis. Instead of a single damping parameter, two independent relaxation times are introduced, which characterize two different dissipation paths. One of the damping mechanisms affecting the magnetization component  $M_z$  along the effective field direction is due to spin-flip transitions. It is characterized by the so-called *longitudinal* or *spin-lattice relaxation time*  $T_1$ . The second damping mechanism arises from the interactions between different magnetic moments, in particular the loss of their phase coherence as they precess around  $\mathbf{H}_{\text{eff}}$ . This spin de-phasing mechanism affects the components  $M_x$  and  $M_y$  and is described by the *transverse* or *spin-spin relaxation time*  $T_2$ . A more detailed description of both damping processes will be given in Section 2.3.5. For  $T_2 \ll T_1$ , which is generally the case, the relaxation in the  $x$ - $y$ -plane is independent of the relaxation along the  $z$ -axis. The change of the Zeeman energy given by Eq. (2.9) is only caused by the change of  $M_z$ , but not by the decay of  $M_x$  and  $M_y$ . Consequently, the magnitude of  $\mathbf{M}$  changes with time and the trajectory of  $\mathbf{M}$  follows an inward spiral towards  $\mathbf{H}_{\text{eff}}$ , as sketched in Fig. 2.2c. Only if  $T_1 \leq T_2$ , the magnitude of the magnetization is conserved and the Landau-Lifshitz relaxation occurs.

### 2.3.2 Dynamic Susceptibility

In this subsection, an expression for the dynamic susceptibility is derived, which describes the dynamic magnetic response of a ferromagnet to small time-varying rf or microwave fields associated with typical magnetic resonance experiments. For this purpose, the LLG equation (2.32) is analytically solved under the following assumptions which reflect the situation in the FMR measurements carried out throughout this thesis:

- The sample is an infinitely extended magnetic thin-film located in the  $x$ - $y$ -plane. Its demagnetizing factors thus correspond to  $N_x = N_y = 0$  and  $N_z = 1$ .
- The sample is assumed to have a uniaxial magnetocrystalline anisotropy with an easy-axis in  $x$ -direction, where the anisotropy field  $H_{\text{uni}} \ll M_S$ .
- A uniform magnetic field  $\mathbf{H}_{\text{ext}}$  applied along the  $x$ -axis leads to a homogeneous magnetization  $\mathbf{M}$  in the same direction.
- A small alternating rf excitation field  $\mathbf{h}_{\text{rf}}(t) \ll \mathbf{H}_{\text{ext}}$  pointing along the  $y$ -direction, i.e., perpendicular to  $\mathbf{H}_{\text{ext}}$ , gives rise to a uniform small-amplitude precession of the magnetization  $\mathbf{M}$  in the  $y$ - $z$ -plane.

The last point allows to separate the magnetization into a static part and small time-dependent components as

$$\mathbf{M} = M_S\mathbf{m} \approx M_S\mathbf{e}_x + m_y(t)\mathbf{e}_y + m_z(t)\mathbf{e}_z, \quad (2.36)$$

where  $m_y, m_z \ll M_S$  are the precessing rf components of the magnetization. The effective magnetic field acting on the sample also includes the small excitation field  $\mathbf{h}_{\text{rf}}$  and is given by

$$\mathbf{H}_{\text{eff}} = (\mathbf{H}_{\text{ext}} + \mathbf{H}_{\text{uni}})\mathbf{e}_x + h_{\text{rf}}(t)\mathbf{e}_y - m_z(t)\mathbf{e}_z. \quad (2.37)$$

Inserting Eq. (2.36) and (2.37) into the LLG equation (2.32) yields

$$0 = -\gamma\mu_0(-m_y m_z - m_z h_{\text{rf}}) + \frac{\alpha}{M_S} \left( m_y \frac{dm_z}{dt} - m_z \frac{dm_y}{dt} \right), \quad (2.38)$$

$$\frac{dm_y}{dt} = -\gamma\mu_0(m_z(H_{\text{ext}} + H_{\text{uni}}) + M_S m_z) - \alpha \frac{dm_z}{dt}, \quad (2.39)$$

$$\frac{dm_z}{dt} = -\gamma\mu_0(M_S h_{\text{rf}} - m_y(H_{\text{ext}} + H_{\text{uni}})) + \alpha \frac{dm_y}{dt}. \quad (2.40)$$

The next step consists of linearizing the aforementioned three equations, i.e., only terms linear in  $h_{\text{rf}}$ ,  $m_y$  and  $m_z$  are considered. If the time dependence of  $\mathbf{h}_{\text{rf}}(t)$  and  $\mathbf{m}(t)$  is taken to be of the form  $e^{i\omega t}$ , the resulting equations expressed in matrix representation read

$$\omega_M \begin{pmatrix} h_{\text{rf}} \\ 0 \end{pmatrix} = \begin{bmatrix} \omega_H + i\omega\alpha & -i\omega \\ i\omega & \omega_H + \omega_M + i\omega\alpha \end{bmatrix} \begin{pmatrix} m_y \\ m_z \end{pmatrix}, \quad (2.41)$$

where the following convenient abbreviations are used

$$\omega_H = \gamma\mu_0(H_{\text{ext}} + H_{\text{uni}}), \quad (2.42)$$

$$\omega_M = \gamma\mu_0 M_S. \quad (2.43)$$

The *Polder susceptibility tensor*  $\overset{\leftrightarrow}{\chi}$  [45] is identified by inverting Eq. (2.41) to obtain

$$\begin{pmatrix} m_y \\ m_z \end{pmatrix} = \mathbf{m} = \overset{\leftrightarrow}{\chi} \mathbf{h}_{\text{rf}} = \begin{bmatrix} \chi_{yy} & \chi_{yz} \\ \chi_{zy} & \chi_{zz} \end{bmatrix} \begin{pmatrix} h_{\text{rf}} \\ 0 \end{pmatrix}. \quad (2.44)$$

As the damping constant  $\alpha$  is generally of the order of  $10^{-3} - 10^{-2}$ , only terms linear in  $\alpha$  are considered and  $1 + \alpha^2 \approx 1$  is used to simplify the calculation. The complex element  $\chi_{yy}$  of the susceptibility tensor, which relates the rf excitation field  $h_{\text{rf}}$  and the magnetization component  $m_y$ , is then given by

$$\chi_{yy} = \chi'_{yy} - i\chi''_{yy} = \frac{\omega_M(\omega_H + \omega_M + i\omega\alpha)}{[\omega_{\text{res}}^2 - \omega^2] + i\alpha\omega(2\omega_H + \omega_M)}, \quad (2.45)$$

where the resonance frequency  $\omega_{\text{res}}$  is defined by

$$\omega_{\text{res}}^2 = \omega_H(\omega_H + \omega_M). \quad (2.46)$$

This expression is a special case of the Kittel equation [46], which gives the resonance condition of a ferromagnetic sample in the case of small damping. Eq. (2.45) can be

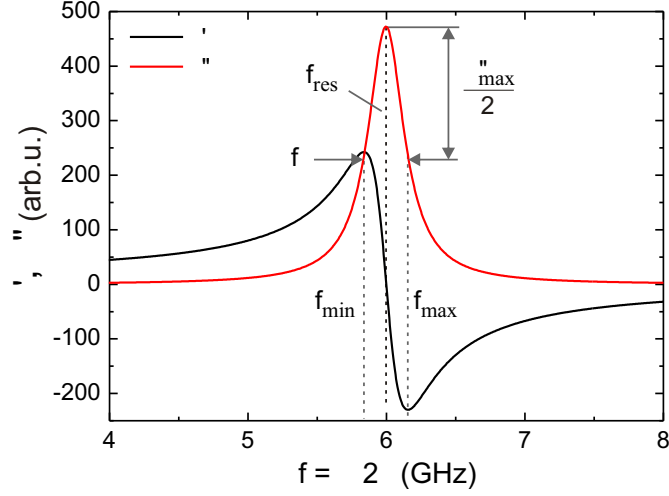


**Fig. 2.3:** Real (black line) and imaginary (red line) part of the complex rf susceptibility  $\chi_{yy}$  calculated using the following parameters:  $\gamma = 184.8$  GHz/T,  $\mu_0 M_S = 1$  T,  $\mu_0(H_{\text{ext}} + H_{\text{uni}}) = 0.04$  T, and  $\alpha = 0.01$ .

split in a real and an imaginary part by multiplying both the numerator and the denominator with the complex conjugate of the denominator. This leads to

$$\chi'_{yy} = \frac{\omega_M(\omega_H + \omega_M)(\omega_{\text{res}}^2 - \omega^2) + \alpha^2\omega^2(2\omega_H + \omega_M)^2}{(\omega_{\text{res}}^2 - \omega^2)^2 + \alpha^2\omega^2(2\omega_H + \omega_M)^2}, \quad (2.47)$$

$$\chi''_{yy} = \frac{\alpha\omega\omega_M[(\omega_{\text{res}}^2 - \omega^2) + (\omega_H + \omega_M)(2\omega_H + \omega_M)]}{(\omega_{\text{res}}^2 - \omega^2)^2 + \alpha^2\omega^2(2\omega_H + \omega_M)^2}. \quad (2.48)$$

A calculated example of the susceptibility  $\chi_{yy}$  is shown in Fig. 2.3. The real part  $\chi'_{yy}$ , representing the dispersion, is antisymmetric around  $\omega_{\text{res}}$  and has a zero crossing at this frequency. The imaginary part  $\chi''_{yy}$  reflects the absorption of the energy provided by the excitation field  $h_{\text{rf}}$ .  $\chi''_{yy}$  has a Lorentzian line shape and reaches a maximum at  $\omega_{\text{res}}$ , which is given by

$$\text{Max}(\chi''_{yy}) = \frac{\omega_M}{\alpha\sqrt{\omega_H(\omega_M + 2\omega_H)}}. \quad (2.49)$$

In the low-frequency limit, the imaginary part of  $\chi_{yy}$  approaches zero, whereas its real part simplifies to

$$\chi_{\text{static}} = \chi'_{\text{static}} = \frac{\omega_M}{\omega_H} = \frac{M_S}{H_{\text{ext}} + H_{\text{uni}}}, \quad (2.50)$$

which represents the well-known static susceptibility.

The frequency linewidth  $\Delta\omega$ , defined as the full width at half maximum (FWHM) of the imaginary part of the susceptibility, is given by

$$\Delta\omega = \alpha(2\omega_H + \omega_M). \quad (2.51)$$

From the direct proportionality to the damping constant  $\alpha$  it can be seen, that higher damping manifests itself in an increased linewidth. Eq. (2.51) is valid for frequency-swept techniques such as VNA-FMR which will be discussed in subsection 4.2. Alternatively,  $\Delta\omega$  can be obtained from the difference of the frequencies at which the real part of the susceptibility is maximum and minimum and is then referred to as peak-to-peak linewidth  $\Delta\omega_{\text{pp}}$ . This method is often more convenient, since determining the frequencies of the two extrema is generally easier than fitting Eq. (2.48).

However, it is much more common to discuss the (FWHM) field linewidth  $\Delta H$ , obtained from field-swept techniques such as conventional FMR (see subsection 4.1), which is related to  $\alpha$  by [47]

$$\mu_0\Delta H = \frac{2}{\sqrt{3}} \frac{\alpha}{\gamma} \omega_{\text{res}}. \quad (2.52)$$

Although  $\Delta\omega$  and  $\Delta H$  are not directly comparable, it is possible to convert one type of linewidth into the other one [48].

### 2.3.3 Smit and Beljers Formulation

In the previous subsection, the ferromagnetic resonance frequency  $\omega_{\text{res}}$  was derived from the solution of the LLG equation of motion. An alternative approach allowing to directly derive the resonance frequency from the sample's total energy density  $\epsilon_{\text{tot}}$  has been formulated by Smit and Beljers [49]. This ansatz, which was also found independently by Suhl [50] and Gilbert [40], is especially useful in the case of complex anisotropies and for investigating the angular dependence of the resonance frequency.

For the derivation of the resonance equation, the damping term in Eq. (2.29) is neglected and spherical coordinates (see Fig. 2.4) will be used, whose unit vectors are given by

$$\mathbf{e}_\rho = \begin{pmatrix} \sin\theta \cos\phi \\ \sin\theta \sin\phi \\ \cos\theta \end{pmatrix}, \quad \mathbf{e}_\theta = \begin{pmatrix} \cos\theta \cos\phi \\ \cos\theta \sin\phi \\ -\sin\theta \end{pmatrix}, \quad \mathbf{e}_\phi = \begin{pmatrix} -\sin\phi \\ \cos\phi \\ 0 \end{pmatrix}. \quad (2.53)$$

Assuming that  $M_S = \text{const.}$ , the magnetization can then be written as

$$\mathbf{M} = M_S \mathbf{m} = M_S(m_x \mathbf{e}_x + m_y \mathbf{e}_y + m_z \mathbf{e}_z) \quad (2.54)$$

$$= M_S(\sin\theta \cos\phi \mathbf{e}_x + \sin\theta \sin\phi \mathbf{e}_y + \cos\theta \mathbf{e}_z) \quad (2.55)$$

$$= M_S \mathbf{e}_\rho. \quad (2.56)$$

With this expression Eq. (2.29) becomes

$$-\sin\phi \dot{\phi} \sin\theta + \cos\phi \cos\theta \dot{\theta} = -\gamma\mu_0(H_z \sin\phi \sin\theta - H_y \cos\theta), \quad (2.57)$$

$$\cos\phi \dot{\phi} \sin\theta + \sin\phi \cos\theta \dot{\theta} = \gamma\mu_0(H_x \cos\theta - H_z \sin\theta \cos\phi), \quad (2.58)$$

$$\dot{\theta} = \gamma\mu_0(H_y \cos\phi - H_x \sin\phi). \quad (2.59)$$

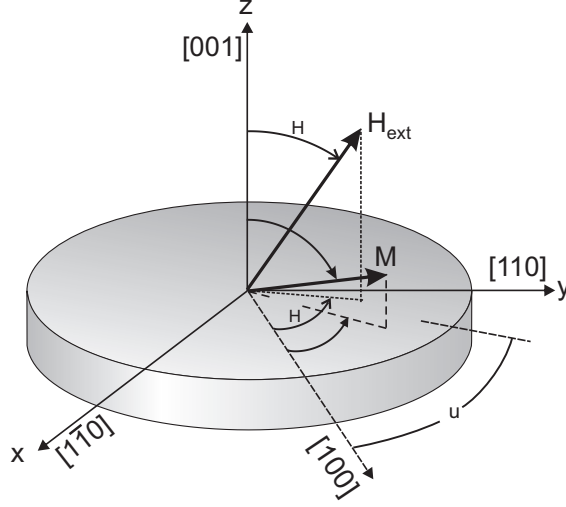


**Fig. 2.4:** Spherical coordinate system.

Inserting Eq. (2.59), which is the equation of motion for the polar angle  $\theta$ , into Eq. (2.57) yields

$$\dot{\phi} \sin \theta = -\gamma \mu_0 (H_x \cos \phi \cos \theta + H_y \sin \phi \cos \theta - H_z \sin \theta), \quad (2.60)$$

$$\dot{\theta} = \gamma \mu_0 (-H_x \sin \phi + H_y \cos \phi). \quad (2.61)$$

The right hand side of both equations contains the components of the effective magnetic field  $\mathbf{H}_{\text{eff}}$  along the unit vectors  $\mathbf{e}_\theta$  and  $\mathbf{e}_\phi$ , respectively. With this, Eq. (2.60) and Eq. (2.61) simplify to

$$\dot{\phi} \sin \theta = -\gamma \mu_0 H_\phi, \quad (2.62)$$

$$\dot{\theta} = \gamma \mu_0 H_\theta. \quad (2.63)$$

At equilibrium, the total energy density is at a minimum and fulfills the conditions

$$\epsilon_\theta = \left. \frac{\partial \epsilon_{\text{tot}}}{\partial \theta} \right|_{\theta=\theta_0} = 0 \quad \text{and} \quad \epsilon_\phi = \left. \frac{\partial \epsilon_{\text{tot}}}{\partial \phi} \right|_{\phi=\phi_0} = 0, \quad (2.64)$$

from which the equilibrium angles  $\theta_0$  and  $\phi_0$  of the magnetization can be determined. The equilibrium condition also means that  $\mathbf{M}$  is parallel to  $\mathbf{H}_{\text{eff}}$  resulting in the latter only having a component in direction of  $\mathbf{M}$  at equilibrium. Writing the differential operator in Eq. (2.5) in spherical coordinates, the effective magnetic field can be expressed as

$$\mathbf{H}_{\text{eff}} = -\frac{1}{\mu_0} \frac{\partial \epsilon_{\text{tot}}}{\partial \mathbf{M}} = -\frac{1}{\mu_0} \left( \frac{\partial \epsilon_{\text{tot}}}{\partial M} \mathbf{e}_M + \frac{1}{M \sin \theta} \frac{\partial \epsilon_{\text{tot}}}{\partial \phi} \mathbf{e}_\phi + \frac{1}{M} \frac{\partial \epsilon_{\text{tot}}}{\partial \theta} \mathbf{e}_\theta \right) \quad (2.65)$$

$$= H_M \mathbf{e}_M + H_\theta \mathbf{e}_\theta + H_\phi \mathbf{e}_\phi \quad (2.66)$$

In non-equilibrium, i.e., when  $\mathbf{M}$  deviates from its equilibrium position by small

angle deflections, which are given by

$$\theta(t) = \theta_0 + \delta\theta(t), \quad \delta\theta \ll \theta_0, \quad (2.67)$$

$$\phi(t) = \phi_0 + \delta\phi(t), \quad \delta\phi \ll \phi_0, \quad (2.68)$$

the conditions in Eq. (2.64) do not longer hold. The total energy density can then be expanded around the equilibrium to

$$\epsilon_\theta = \epsilon_{\theta\theta}\delta\theta + \epsilon_{\theta\phi}\delta\phi, \quad (2.69)$$

$$\epsilon_\phi = \epsilon_{\phi\theta}\delta\theta + \epsilon_{\phi\phi}\delta\phi, \quad (2.70)$$

where  $\epsilon_{ij}$  are the second partial derivatives of  $\epsilon_{\text{tot}}$  with respect to  $i$  and  $j$  at equilibrium. Combining the equation of motion (2.63) with Eq. (2.65) for the effective field  $\mathbf{H}_{\text{eff}}$  leads to the following set of linear differential equations describing small oscillations of  $\mathbf{M}$  around its equilibrium positions:

$$\frac{M_S}{\gamma} \sin \theta_0 \frac{\partial \theta}{\partial t} = \epsilon_{\phi\theta}\delta\theta + \epsilon_{\phi\phi}\delta\phi, \quad (2.71)$$

$$-\frac{M_S}{\gamma} \sin \theta_0 \frac{\partial \phi}{\partial t} = \epsilon_{\theta\theta}\delta\theta + \epsilon_{\theta\phi}\delta\phi. \quad (2.72)$$

With a time dependence of the form  $\delta\theta(t), \delta\phi(t) \propto \exp(i\omega t)$ , the homogeneous system of equations can be written as

$$0 = \left( \epsilon_{\phi\theta} + i\omega \frac{M_S \sin \theta_0}{\gamma} \right) \delta\theta + \epsilon_{\phi\phi}\delta\phi, \quad (2.73)$$

$$0 = \epsilon_{\theta\theta}\delta\theta + \left( \epsilon_{\theta\phi} + i\omega \frac{M_S \sin \theta_0}{\gamma} \right) \delta\phi. \quad (2.74)$$

It has nontrivial periodic solutions if the determinant vanishes, which yields the following expression for the resonance frequency:

$$\omega_{\text{res}} = \frac{\gamma}{M_S \sin \theta_0} \sqrt{\frac{\partial^2 \epsilon_{\text{tot}}}{\partial \phi^2} \frac{\partial^2 \epsilon_{\text{tot}}}{\partial \theta^2} - \left( \frac{\partial^2 \epsilon_{\text{tot}}}{\partial \phi \partial \theta} \right)^2} \Bigg|_{\theta=\theta_0, \phi=\phi_0}. \quad (2.75)$$

Eq. (2.75) is called Smit and Beljers resonance equation and is the standard method to determine the precessional frequency. It shows that in a FMR measurement, the curvature of the surface of the total energy, given by the second derivatives, is probed. In contrast to the derivation of  $\omega_{\text{res}}$  in the previous subsection, this method only requires that an expression for the total energy density  $\epsilon_{\text{tot}}$  of the system as well as the equilibrium positions of  $\mathbf{M}$  are known. This allows for easily including any type of anisotropy or other contribution to the total energy density.

Although the general form of the resonance equation (2.75) is mathematically correct, it is physically not quite satisfying since it cannot be solved for  $\theta = 0$ , i.e., when  $\mathbf{M}$  is oriented perpendicular to the sample plane. This problem can be



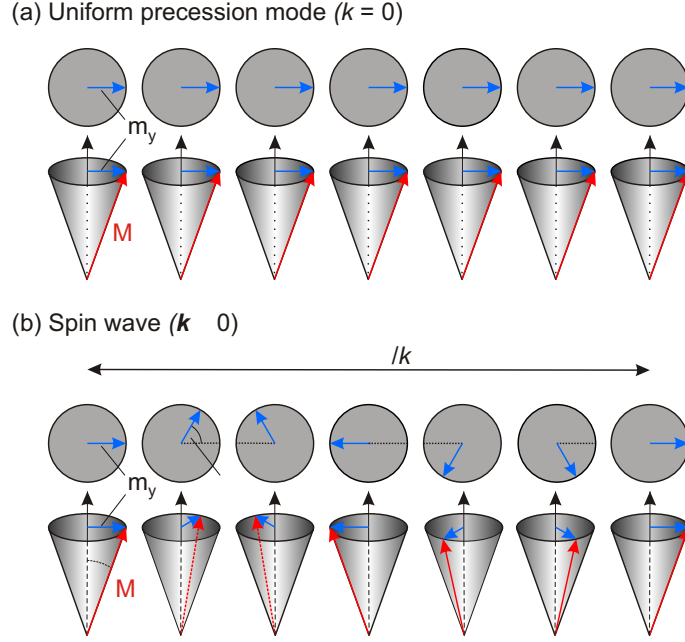


**Fig. 2.5:** Illustration of (a) the uniform precession mode with wave vector  $k = 0$  and (b) a finite wavelength spin wave mode with  $\mathbf{k}$ .  $\theta$  is the polar tilting angle of  $\mathbf{M}$  away from equilibrium and  $\varphi$  is the azimuthal phase angle of the transverse dynamic moment  $\mathbf{m}$ .

circumvented by using the extended equation provided by Baselgia *et al.* [51], which includes terms proportional to the first derivatives of  $\epsilon_{\text{tot}}$  with respect to  $\theta$  and  $\phi$ , respectively:

$$\left(\frac{\omega_{\text{res}}}{\gamma}\right)^2 = \frac{1}{M_S^2} \left[ \epsilon_{\theta\theta} \left[ \frac{\epsilon_{\phi\phi}}{\sin^2 \theta} + \frac{\cos \theta}{\sin \theta} \epsilon_{\theta} \right] - \left[ \frac{\epsilon_{\theta\phi}}{\sin \theta} - \frac{\cos \theta}{\sin^2 \theta} \epsilon_{\phi} \right]^2 \right]. \quad (2.76)$$

### 2.3.4 Magnetic Excitations

In FMR experiments only modes are excited for which the total momentum is zero, i.e., the wave vector  $\mathbf{k} = 0$ , and which do not transfer any momentum. For a zero wave vector mode with modulus  $k = 0$  ( $\lambda = \infty$ ), amplitude, phase, and frequency are constant throughout the entire sample. Correspondingly, this mode, illustrated in Fig. 2.5a, is called *uniform* mode. However, thermal activation, non-uniform excitation fields, and defects in the sample give rise to another type of magnetic excitation. In this case, *standing spin waves* can be excited, which are finite wavelength modes with modulus  $k \neq 0$  ( $\lambda < \infty$ ). *Spin waves*, or *magnons*, are the fundamental excitations of a magnetic system and provide the basis to describe the spatial and temporal evolution of the magnetization. A typical spin wave is depicted in Fig. 2.5b. Here,  $\theta$  is the polar tilting angle of  $\mathbf{M}$  away from equilibrium and  $\varphi$  is the azimuthal phase angle of the transverse dynamic magnetization  $\mathbf{m}$ . Contrary to the uniform mode with spatially constant amplitude and phase, standing spin waves are characterized by a spatially varying amplitude  $\theta(\mathbf{r})$  and a spatially constant

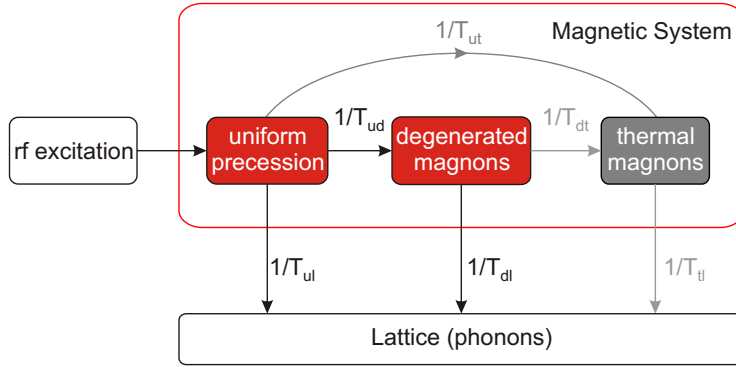


**Fig. 2.6:** Schematic representation of relaxation processes after Fletcher-LeCraw-Spencer [53]. Spin-spin processes redistribute the energy between the different modes of the magnetic system, whereas spin-lattice processes transfer energy to the lattice. The involved relaxation processes are:

$1/T_{ud}$	two-magnon	$1/T_{dl}$	see $1/T_{ul}$
$1/T_{ul}$	magnon-phonon, eddy currents, ...	$1/T_{dt}$	three-magnon
$1/T_{ut}$	three-magnon, four-magnon	$1/T_{tl}$	magnon-phonon

phase  $\varphi(\mathbf{r})$ . Consequently, these modes contain contributions of different order from exchange and dipolar energies and can therefore be classified into exchange- or dipolar-dominated depending on their wavelength [52]. For short wavelengths the spin wave properties are dominated by exchange interaction and the corresponding excitations are called *exchange spin wave* or simply *spin wave*. For long wavelengths the exchange interaction becomes negligible and the magnetic dipolar interaction dominates. In this case, the corresponding excitations are referred to as *dipolar spin waves* or *magnetostatic waves*.

### 2.3.5 Magnetization Damping

In Chapter 2.3, the equation of motion was extended by a damping term in order to account for the relaxation of the precessional motion of the magnetization. However, Gilbert-like damping, as described by a single phenomenological damping constant  $\alpha$ , is only one among a variety of dissipation processes.

Some of the processes involved in the relaxation of the precession are shown in Fig. 2.6. First, the uniform precession mode excited by an rf or microwave field is considered. This mode can directly transfer its energy to the lattice by scattering of phonons at the spin system, by scattering with conduction electrons, or by modulation of the dipolar interaction due to lattice vibrations. These processes can be well described by the spin-lattice relaxation term of the BB equation (2.35), but also with the LLG equation (2.32).

A second relaxation path involves intermediate states, in which the uniform precession mode with  $\mathbf{k} = 0$  is scattered to a degenerated spin wave mode ( $\mathbf{k} \neq 0$  magnon) in a process referred to as *two-magnon scattering*. This process as well as the scattering among non-uniform modes by three- and four-magnon processes

redistribute the energy between the different modes of the magnetic system. Since the magnitude of the magnetization  $\mathbf{M}$  is not conserved in these processes, the LLG equation is unsuitable for their description. Instead, the spin-spin relaxation term of the Bloch-Bloembergen ansatz can be used. In the end, also the degenerated and thermal magnons release their energy to the lattice.

In the following, two examples of damping processes will be outlined: Eddy currents, an intrinsic unavoidable contribution, and two-magnon scattering as an extrinsic contribution arising from structural inhomogeneities in the sample as well as defects.

### Eddy Currents

In metallic thin films the magnetic damping can be influenced by eddy currents. These are characterized by the skin depth  $\delta$ , that is defined as the distance below the surface of a conductor at which the amplitude of an electromagnetic wave or current density decreases by a factor of  $1/e$ . It is given by

$$\delta = \sqrt{\frac{2}{\sigma\omega\mu_r\mu_0}}, \quad (2.77)$$

where  $\sigma$  is the electrical conductivity and  $\mu_r = \mu/\mu_0 = 1 + \chi$  is the relative magnetic permeability.

The classical skin depth for nonmagnetic conductors can be derived from the frequency-independent static susceptibility  $\chi_{\text{static}}$ , given by Eq. (2.50), such that  $\mu_r = 1 + \chi_{\text{static}}$ . However, this simplification is only valid for frequencies below 1 GHz. The FMR skin depth is calculated using the dynamic susceptibility  $\chi_{yy} = \chi'_{yy} - i\chi''_{yy}$  as defined by Eqs. (2.47) and (2.48), which results in  $\mu_r$  and  $\delta$  to be complex numbers.

For typical transition metals, the classical skin depth at 10 GHz is in the order of 1  $\mu\text{m}$  [54]. However, near the ferromagnetic resonance frequency, the relative permeability drastically increases, which in turn reduces the skin depth.

The damping contribution from eddy currents decreases rapidly with the film thickness  $d$ , as it is proportional to  $d^2$  [47]. For instance, for Fe films below 25 nm and NiFe films below 100 nm, the role of eddy currents is negligible. In the case of thick films with  $d > \delta \approx 100$  nm at FMR, the linewidth broadening by eddy currents is proportional to  $\sqrt{\sigma A}$ , where  $A$  is the exchange constant. This expression describes the so-called exchange-conductivity mechanism, introduced by Ament and Rado [55], which leads to a finite linewidth even in the absence of intrinsic damping. As an example, for an Fe film of 200 nm thickness, an increase in FMR linewidth by a factor of 7 compared to the intrinsic Gilbert damping contribution has been observed [47].

### Two-Magnon Scattering

Two-magnon scattering was proposed several decades ago as an extrinsic contribution to the FMR linewidth in the ferromagnetic insulator yttrium iron garnet (YIG) [56,57]. In recent years, this linewidth broadening mechanism was, especially in the field

of ultrathin magnetic films, the subject of extensive research both experimentally [23, 58–67] and theoretically [64, 68–70].

In the two-magnon scattering process, the uniform precession mode ( $\mathbf{k} = 0$ ) relaxes by scattering into nonuniform modes ( $\mathbf{k} \neq 0$ ), which are degenerate in frequency. However, this type of relaxation is just a mode conversion, as the number of magnons excited in the system remains unchanged. The longitudinal component of the rf magnetization is not changed, whereas its transverse component decreases since the final state magnon has a finite wave vector. Thus, two-magnon scattering is a dephasing process, which contributes to the transverse relaxation time  $T_2$ . In contrast, the longitudinal relaxation time  $T_1$ , related to the relaxation of the  $\mathbf{k} \neq 0$  magnons to the lattice, is left unaffected. For this reason, two-magnon scattering is best described by the BB equation (2.35), but not by the LLG equation.

Arias and Mills [69] have developed a detailed theory of two-magnon scattering in in-plane magnetized ultrathin films, which is assumed to be activated by surface defects such as island and/or pits in the shape of platelets. These defects lead to Zeeman and dipolar perturbations giving rise to spin waves. Finite wave vector modes, that are degenerate with the FMR mode, exist for  $|\phi_{k\parallel}| < \phi_C$ , where  $\phi_{k\parallel}$  is the angle between the direction of propagation of the spin wave and the magnetization, and  $\phi_C = \sin^{-1} \sqrt{H_0 / (H_0 + \mu_0 M_{\text{eff}})}$ . If the external in-plane dc magnetic field  $H_0$  is decreased to zero, the critical angle  $\phi_C$  vanishes, and no spin wave modes are degenerate with the FMR mode. Consequently, as the resonance frequency approaches zero, two-magnon scattering shuts off.

Another interesting situation occurs if an out-of-plane component of  $H_0$  is present as discussed by Erickson and Mills [68]. When the magnetization is subsequently tipped out-of-plane, finite wave vector modes are degenerate with the FMR mode only as long as  $\eta < 45^\circ$ , where  $\eta$  is the angle between the magnetization and the film surface. For larger values of  $\eta$ , the contribution of two-magnon scattering disappears. This is an important criterion allowing to test its applicability in the interpretation of extrinsic damping as the FMR linewidth in perpendicular configuration,  $\Delta H_\perp$ , should be smaller than the one in parallel configuration,  $\Delta H_\parallel$ , i.e., two-magnon scattering is switched off.

The damping contribution of two-magnon scattering is not Gilbert-like, i.e., the field linewidth  $\Delta H$  is not proportional to the resonance frequency, but shows a frequency dependence resembling a root function. However, as pointed out by Lenz *et al.* [23], if the linewidth is only investigated across a limited frequency range, it can be wrongly fitted with a linear frequency dependence and a constant zero-frequency linewidth, which usually accounts for sample inhomogeneities. Therefore, it is imperative to investigate the linewidth over a broad frequency range and to perform angle-dependent measurements in order to have clear evidence for the presence of two-magnon scattering.

# 3 Basics of Microwave Engineering

In this chapter, an overview on some basic aspects and concepts of microwave engineering is given, which are necessary to understand the physics and technology behind the measurement principle of VNA-FMR used in this thesis.

## 3.1 Theory of Transmission Lines

A transmission line is a medium transmitting electrical signals, such as acoustic waves or electromagnetic waves, as well as electrical power between one point to another. Types of transmission lines include wires, coaxial cables, dielectric slabs, striplines, optical fibers, electric power lines, and waveguides. In the following, the telegrapher's equations, a pair of linear differential equations describing the temporal and spatial propagation of voltage and current on an electrical transmission line, will be derived. This can be realized by two different approaches: Maxwell's equations or basic circuit theory, with the latter one being more practical for the present purpose. In addition, the physical quantities necessary for the characterization of transmission lines will be introduced.

### 3.1.1 The Telegrapher's Equations

The simplest type of transmission line is shown in Fig. 3.1a. It consists of two parallel wires of small length  $\Delta z$  that are insulated from each other. The infinitesimally short segment  $\Delta z$  can be modeled as a lumped-element circuit, depicted in Fig. 3.1b, consisting of the series resistance  $R$ , the series inductance  $L$ , the shunt conductance  $G$ , and the shunt capacitance  $C$ . These four quantities are defined per unit length and are called the primary transmission line constants. The series resistance  $R$  represents the resistance due to the finite conductivity of the conductors, and the shunt conductance  $G$  is due to dielectric loss in the material between the conductors. The series inductance  $L$  arises due to the total self-inductance of the two conductors, and the shunt capacitance  $C$  appears due to the close proximity of the two conductors. The series impedance  $Z$  is then given by  $Z = R + j\omega L$ , and the shunt admittance  $Y$  is given by  $Y = G + j\omega C$ .

Applying Kirchhoff's voltage law and current law to the circuit in Fig. 3.1b gives

$$V(z, t) - R\Delta z I(z, t) - L\Delta z \frac{\partial I(z, t)}{\partial t} - V(z + \Delta z, t) = 0, \quad (3.1)$$

$$I(z, t) - G\Delta z V(z + \Delta z, t) - C\Delta z \frac{\partial V(z + \Delta z, t)}{\partial t} - I(z + \Delta z, t) = 0. \quad (3.2)$$

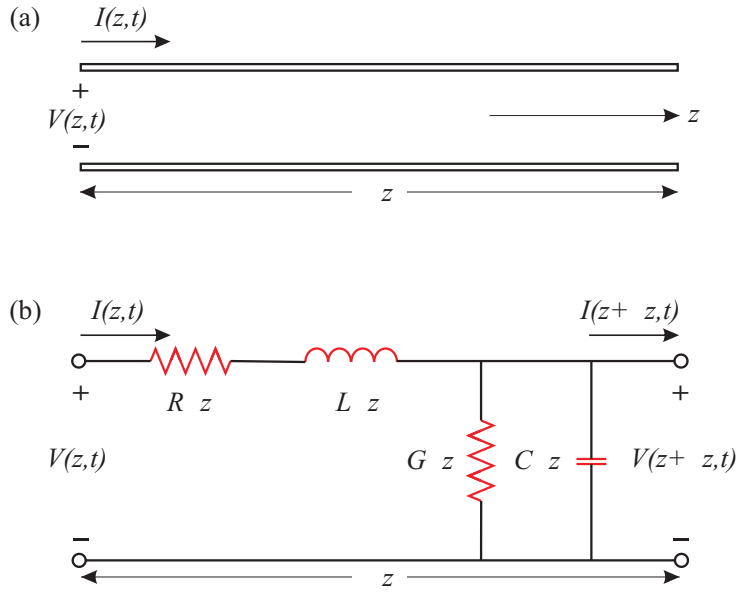


**Fig. 3.1:** A transmission line (a) and its equivalent circuit (b), consisting of the series resistance  $R$ , the series inductance  $L$ , the shunt conductance  $G$ , and the shunt capacitance  $C$ . (Adapted from Ref. [71].)

Dividing Eqs. (3.1) and (3.2) by  $\Delta z$  and taking the limit  $\Delta z \rightarrow 0$  gives the following pair of coupled linear differential equations:

$$\frac{\partial V(z,t)}{\partial t} = -RI(z,t) - L\frac{\partial I(z,t)}{\partial t}, \quad (3.3)$$

$$\frac{\partial I(z,t)}{\partial t} = -GV(z,t) - C\frac{\partial V(z,t)}{\partial t}. \quad (3.4)$$

Assuming a sinusoidal time dependence which can be written in complex notation as

$$V(z,t) = \text{Re}[V(z)e^{j\omega t}], \quad (3.5)$$

$$I(z,t) = \text{Re}[I(z)e^{j\omega t}], \quad (3.6)$$

allows to separate the space and time dependence. Eliminating  $t$  from the previous two equations gives

$$\frac{dV(z)}{dz} = -(R + j\omega L)I(z), \quad (3.7)$$

$$\frac{dI(z)}{dz} = -(G + j\omega C)V(z). \quad (3.8)$$

Equations (3.7) and (3.8) are differentiated with respect to  $z$  and combined, so that

$$\frac{d^2V(z)}{dz^2} = \gamma^2V(z), \quad (3.9)$$

$$\frac{d^2I(z)}{dz^2} = \gamma^2I(z), \quad (3.10)$$

where

$$\gamma = \sqrt{(R + j\omega L)(G + j\omega C)} = \sqrt{ZY} \quad (3.11)$$

is the propagation constant, which is a function of frequency. The general solutions for voltage and current can be written as

$$V(z) = V_0^+ e^{-\gamma z} + V_0^- e^{\gamma z}, \quad (3.12)$$

$$I(z) = I_0^+ e^{-\gamma z} + I_0^- e^{\gamma z}, \quad (3.13)$$

and are linear combinations of waves traveling along the transmission line in opposite directions. The  $e^{-\gamma z}$  term represents wave propagation in the  $+z$  direction (incident wave), and the  $e^{\gamma z}$  term represents wave propagation in the  $-z$  direction (reflected wave).  $V_0^+$ ,  $V_0^-$ ,  $I_0^+$ , and  $I_0^-$  are arbitrary integration constants that can be determined from boundary conditions.

### 3.1.2 Characteristic Impedance

Differentiating Eq. (3.12) one gets

$$\frac{dV(z)}{dz} = -\gamma V_0^+ e^{-\gamma z} + \gamma V_0^- e^{\gamma z}. \quad (3.14)$$

From Eqs. (3.7) and (3.14) one obtains

$$-(R + j\omega L)I(z) = -\gamma V_0^+ e^{-\gamma z} + \gamma V_0^- e^{\gamma z},$$

which can be rewritten in the following form:

$$I(z) = \frac{1}{Z_0} (V_0^+ e^{-\gamma z} - V_0^- e^{\gamma z}), \quad (3.15)$$

where

$$Z_0 = \frac{R + j\omega L}{\gamma} = \sqrt{\frac{R + j\omega L}{G + j\omega C}} = \sqrt{\frac{Z}{Y}} \quad (3.16)$$

is the characteristic impedance of the transmission line. Comparing Eqs. (3.13) and (3.15), it can be seen that  $Z_0$  is related to the amplitudes of voltage and current at either end of the transmission line as

$$Z_0 = \frac{V_0^+}{I_0^+} = -\frac{V_0^-}{I_0^-}. \quad (3.17)$$

### 3.1.3 Propagation Constant

Like the characteristic impedance  $Z_0$ , the propagation constant  $\gamma$ , introduced in Eq. (3.11), is a complex quantity. It is defined per unit length and can be written as

$$\gamma = \alpha + j\beta, \quad (3.18)$$

where  $\alpha$  is the attenuation constant and  $\beta$  is the phase constant.  $Z_0$ ,  $\alpha$ , and  $\beta$  are also called secondary constants of a transmission line. Using Eqs. (3.12) and (3.18), one of the general solutions of the wave equation can be expressed as

$$V(z, t) = V_0^+ e^{-\alpha z} e^{j(\omega t - \beta z)} + V_0^- e^{\alpha z} e^{j(\omega t + \beta z)}. \quad (3.19)$$

The wave amplitude is progressively reduced because of the factor  $e^{\pm\alpha z}$ , whereas the term  $e^{j(\omega t \pm \beta z)}$  leads to a phase change per unit length of propagation.

## 3.2 Propagation Modes of Electromagnetic Waves

On transmission lines and waveguides, different types and modes of wave propagation exist. Transmission lines consisting of at least two conductors, e.g., coaxial lines, support transverse electromagnetic (TEM) waves. TEM waves are characterized by their electric and magnetic fields being perpendicular to the direction of propagation and by the lack of longitudinal field components ( $E_z = H_z = 0$ ). TEM waves are non-dispersive and have a uniquely defined current, voltage, and characteristic impedance. Waveguides, often consisting of only a single conductor, support transverse electric (TE) and transverse magnetic (TM) modes of propagation. TE waves are characterized by  $E_z = 0$  and  $H_z \neq 0$ , whereas TM waves are characterized by  $H_z = 0$  and  $E_z \neq 0$ . In contrast to TEM waves, TE and TM waves are dispersive and do not have a uniquely defined voltage and current. Thus, their characteristic impedance may be defined in different ways.

TE and TM waves can occur in modes of different order which, except for the fundamental mode, exhibit a cutoff phenomenon since their phase constant  $\beta$  is both a function of frequency and the geometry of the line or guide. At a given frequency  $f$ , only modes with  $f > f_c$  will propagate. At frequencies below the cutoff frequency  $f_c$  of a given mode, the propagation constant is purely imaginary, leading to a rapid exponential decay of all field components [71]. Such modes are referred to as cutoff or evanescent modes. The mode with the lowest cutoff frequency is called the dominant mode. The cutoff frequency  $f_c$  is given by

$$f_c = \frac{ck_c}{2\pi\sqrt{\mu_r\epsilon_r}}, \quad (3.20)$$

where  $k_c = \sqrt{k^2 - \beta^2}$  is the cutoff wavenumber. If more than one mode is propagating, the transmission line or waveguide is said to be *overmoded*.

## 3.3 Types of Transmission Lines

In this section, the two types of transmission lines used in the VNA-FMR setups are discussed in detail: the *coaxial line* and the *coplanar waveguide*.



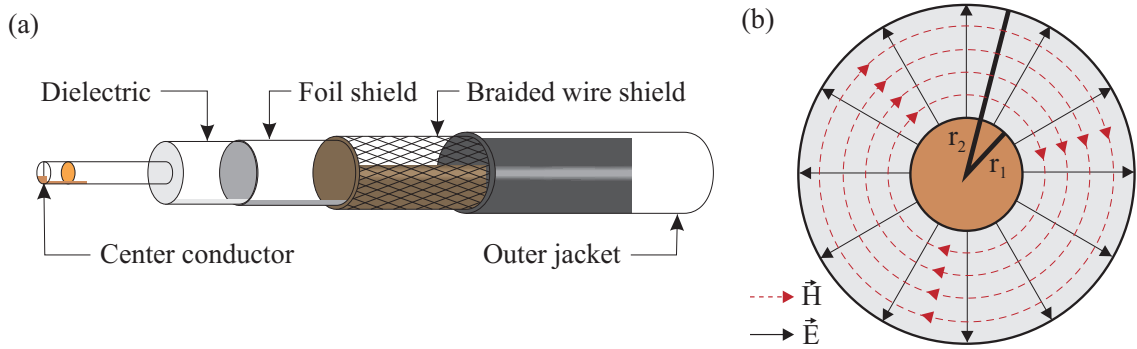


**Fig. 3.2:** (a) Components and (b) TEM mode field pattern of a coaxial cable.

### 3.3.1 Coaxial Line

A coaxial line is an electrical cable consisting of an inner conductor surrounded by a tubular insulating or dielectric material, all of which are surrounded by a conductive layer, and finally covered with a thin insulating layer on the outside. The term coaxial comes from the inner conductor and the outer shield sharing the same geometric axis. A schematic representation of a coaxial cable is shown in Fig. 3.2a.

The center conductor is responsible for the signal transmission and is typically made of pure copper, copper- or silver-plated iron, or aluminum. The insulator surrounding the inner conductor physically holds it in the center of the cable. The dielectric may be solid plastic, foam plastic, or air with spacers supporting the inner wire. Common choices are foamed polyethylene (FPE), polytetrafluoroethylene (PTFE), polyethylene (PE), polypropylene (PP), and polyvinyl chloride (PVC). The outer conductor, or shield, typically consists of braided copper wire which allows the cable to be flexibly bended, protects the signal from electromagnetic interference, and restricts the electromagnetic field to the space between the two conductors. The field pattern of the TEM mode is displayed in Fig. 3.2b. The electric field is oriented radially, whereas the magnetic field runs in concentric circles between the two conductors. To prevent the outer conductor itself from radiating, it is connected to ground. For optimum shielding performance, it is nowadays more common to put an additional thin aluminum foil shield between insulator and wire braid. Other shield designs, e.g., solid metal tubes, lead to better performance, but sacrifice flexibility as those cables cannot take sharp bends. The insulating outer jacket is generally made out of flexible PVC and protects the entire cable against dust, water, and corrosion.

For applications up to few GHz, the primary propagation mode carrying most of the microwave power is TEM. At even higher frequencies, non-TEM modes start to propagate. The cutoff frequencies of these higher-order modes depend on the diameters of the two conductors. For example, the cutoff frequency of the  $TE_{11}$  mode is given by [71]

$$f_c = \frac{2c}{\pi(r_1 + r_2)\sqrt{\mu_r \epsilon_r}}. \quad (3.21)$$

The electrical properties of a coaxial line are determined by the radii  $r_1$  and  $r_2$

of the inner and outer conductor, as well as the permittivity  $\epsilon = \epsilon_0\epsilon_r = \epsilon' + j\epsilon''$  and magnetic permeability  $\mu = \mu_0\mu_r = \mu' + j\mu''$  of the dielectric. The characteristic circuit parameters  $L, C, R$ , and  $G$  can be calculated as [71]

$$L = \frac{\mu}{2\pi} \ln \frac{r_2}{r_1}, \quad (3.22)$$

$$C = \frac{2\pi\epsilon}{\ln \frac{r_2}{r_1}}, \quad (3.23)$$

$$R = \frac{R_s}{2\pi} \left( \frac{1}{r_1} + \frac{1}{r_2} \right), \quad (3.24)$$

$$G = \frac{2\pi\omega\epsilon}{\ln \frac{r_2}{r_1}}, \quad (3.25)$$

where  $R_s$  is the surface resistance of the inner and outer conductor. Using Eq. (3.16), the characteristic impedance  $Z_0$  of a lossless coaxial line is given by

$$Z_0 = \sqrt{\frac{L}{C}} = \frac{1}{2\pi} \sqrt{\frac{\mu}{\epsilon}} \ln \frac{r_2}{r_1} = \frac{1}{2\pi} \sqrt{\frac{\mu_0}{\epsilon_0}} \sqrt{\frac{\mu_r}{\epsilon_r}} \ln \frac{r_2}{r_1}. \quad (3.26)$$

Replacing the quantity  $\sqrt{\mu_0/\epsilon_0}$ , the so-called impedance of free space, with its numerical value of  $376.7 \Omega$ , one gets

$$Z_0 \simeq 60 \Omega \sqrt{\frac{\mu_r}{\epsilon_r}} \ln \frac{r_2}{r_1}. \quad (3.27)$$

The most common impedances are  $Z_0 = 50 \Omega$  and  $Z_0 = 75 \Omega$ , although other impedances are available for specific applications.  $50 \Omega$  coaxial cables are widely used for broadband telecommunication applications, whereas  $75 \Omega$  coaxial cables are mostly employed for transmitting radio or cable television signals.

The impedances of an air dielectric coaxial cable ( $\epsilon_r = \mu_r = 1$ ) for maximum power transmission, highest breakdown voltage, and minimum attenuation have been determined to be  $30 \Omega$ ,  $60 \Omega$ , and  $76.7 \Omega$ , respectively [72]. Thus, a  $50 \Omega$  characteristic impedance represents a compromise between maximum power capacity and minimum attenuation.

The propagation constant of the lossless line ( $\alpha = 0$ ) is given by

$$\beta = \omega \sqrt{\mu\epsilon} = \omega \sqrt{\mu_0\epsilon_0} \sqrt{\mu_r\epsilon_r} = \frac{\omega}{c} \sqrt{\mu_r\epsilon_r}, \quad (3.28)$$

and the phase velocity is

$$v_p = \frac{\omega}{\beta} = \frac{c}{\sqrt{\mu_r\epsilon_r}}. \quad (3.29)$$

### 3.3.2 Coplanar Waveguide

A coplanar waveguide (CPW), proposed by C. P. Wen in 1969 [73], is a type of planar transmission line mainly used in microwave integrated circuits (MICs) as well as

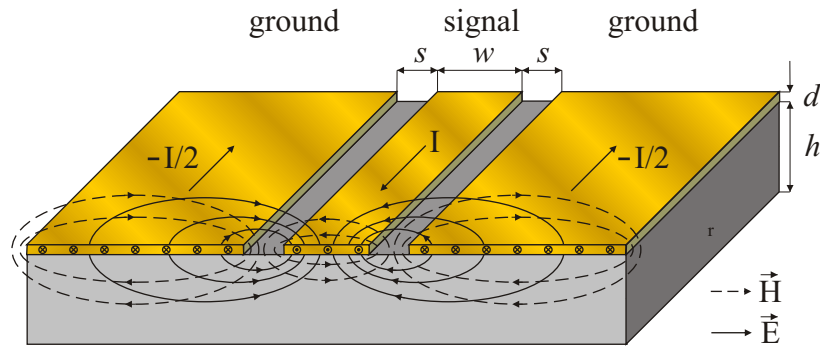


**Fig. 3.3:** Geometry and field pattern of a coplanar waveguide.

in monolithic microwave integrated circuits (MMICs). The unique feature of this transmission line is its uniplanar construction, which means that all of the conductors are on the same side of the substrate. This attribute simplifies manufacturing and allows fast and inexpensive characterization using on-wafer techniques up to frequencies of several tens of GHz [74].

A CPW consists of a dielectric substrate of thickness  $h$  and relative permittivity  $\epsilon_r$  with three metallic conductors of thickness  $d$  on the top surface. The center conductor, or signal line, of width  $w$  is separated by narrow gaps of width  $s$  from two ground planes on either side. In this respect, a CPW can be thought of as a slotline with a third conductor centered in the slot region. The geometry and field pattern of a coplanar waveguide are shown in Fig. 3.3. Modifications of this conventional CPW design include, e.g., a conductor backed or grounded CPW (GCPW), with an additional ground plane at the bottom surface of the dielectric substrate, or an asymmetric CPW with ground planes of different width.

The center conductor carries a current  $I$ , whereas the two ground planes each carry a current of  $-I/2$ . Therefore, the generated magnetic fields are oriented in opposite directions. At the center of a conductor the magnetic field is transversal in-plane, whereas near the conductor edges it is perpendicular to the air-dielectric interface. In the air regions the magnetic field lines curve and return to the slot at half-wavelength intervals. Consequently, a wave propagating along the CPW has an elliptically polarized magnetic field. In addition, electric fields are created, which perpendicularly intersect the magnetic field lines and extend across the slot. A CPW has one half of its electromagnetic field lines in the dielectric substrate and the other half in the air above the conductors. For this reason, the wave propagation mode in a CPW is not a pure TEM mode since the phase velocities of the waves in the dielectric region and the air region differ from each other. However, in most practical applications, the dielectric substrate is electrically very thin ( $h \ll \lambda$ ) resulting in the longitudinal field component being considerably smaller than the transversal ones, so that the propagation mode is quasi-TEM with low dispersion [75].

As CPW-type transmission lines possess three separate conductors, they will support two independent quasi-TEM modes. For symmetric CPWs, these modes are called even or CPW mode and odd or coupled slotline mode [76]. In general, either of these two modes can propagate along the CPW independently if they are excited,

and they are coupled to each other at discontinuities. In the case where an even mode is excited, the electrical fields in the two gaps are oriented in same direction, whereas for an odd mode excitation, they are oriented in the opposite direction [71].

In most practical applications, a supporting metal plane on the substrate backside exists which is formed, for instance, by the chuck of a wafer-prober station. This geometry is equivalent to a GCPW and exhibits an additional fundamental mode, the parallel-plate line (PPL) mode [77]. Without mode suppression techniques, all of these three dominant modes which have no cutoff frequencies, as well as higher-order modes may be excited, resulting in a deterioration of the broadband performance due to overmoding and leakage. Leakage occurs when the phase velocity of the parasitic PPL mode is slower than the phase velocity of the CPW mode [78]. To maintain only the desired CPW mode of propagation, the CPW can be equipped with air bridges connecting its two upper ground planes, microwave absorbers, or low height side walls which together with the conductor backing constitute a structure termed channelized coplanar waveguide (CCPW) [74]. However, effectiveness and feasibility of these solutions are often limited. An alternative approach often found in practice is to connect the top ground planes to the bottom ground plane of the GCPW by means of metal-filled holes called vias [74]. The vias act as lateral microwave walls similar to the side walls of the CCPW and eliminate the excitation of the PPL mode as this one is closely related to the voltage difference between the top and bottom ground planes. The cutoff frequencies of higher-order modes can be raised by reducing the spacing of the via rows [79]. Moreover, the high-frequency performance of the vias is determined by their number, diameter, and spacing, which should be optimized by E-M simulation software.

The dimensions of the center conductor, the gap to the ground planes, as well as the thickness and permittivity of the dielectric substrate determine the effective dielectric constant, characteristic impedance, and the propagation constant of the CPW. As for the coaxial line,  $Z_0$  and  $v_p$  can be calculated using  $L$  and  $C$ . According to [80],  $L$  and  $C$  are given by

$$L = \frac{\mu_0}{4} f(s, w, h), \quad (3.30)$$

$$C = \frac{4\epsilon_0\epsilon_{\text{eff}}}{f(s, w, h)}, \quad (3.31)$$

where  $f(s, w, h)$  is a complicated function of complete elliptical integrals depending on the geometry of the CPW, and  $\epsilon_{\text{eff}}$  is the effective permittivity of the CPW.  $\epsilon_{\text{eff}}$  can be interpreted as the dielectric constant of a homogeneous medium replacing the dielectric substrate of the CPW and its surrounding air. Since the field lines are not contained entirely in the dielectric, but also extend in the air, the effective permittivity satisfies the relation

$$1 < \epsilon_{\text{eff}} < \epsilon_r.$$

In practice, the substrate thickness  $h$  is much bigger than the conductor width  $w$

and the slot width  $s$ , and the effective permittivity is estimated by

$$\epsilon_{\text{eff}} = \frac{\epsilon_r + 1}{2}, \quad (3.32)$$

which is equal to the average of the dielectric constant of the substrate and that of the free space. The characteristic impedance  $Z_0$  is then given by

$$Z_0 = \sqrt{\frac{L}{C}} = \frac{1}{4} \sqrt{\frac{\mu_0}{\epsilon_0 \epsilon_{\text{eff}}}} f(s, w, h) \simeq \frac{30\pi \Omega}{\sqrt{\epsilon_{\text{eff}}}} f(s, w, h), \quad (3.33)$$

where  $\sqrt{\mu_0/\epsilon_0}$  is approximated by  $120\pi$ . For a given thickness  $h$  and relative permittivity  $\epsilon_r$  of the substrate, the characteristic impedance  $Z_0$  of the CPW is determined by the ratio of  $s/(s + 2w)$ . Thus, it is possible to scale the size of the CPW while keeping the impedance constant, e.g., at  $50 \Omega$ .

The phase velocity and propagation constant can be expressed as

$$v_p = \frac{1}{\sqrt{LC}} = \frac{1}{\sqrt{\mu_0 \epsilon_0 \epsilon_{\text{eff}}}} = \frac{c}{\sqrt{\epsilon_{\text{eff}}}} \quad (3.34)$$

$$\beta = k_0 \sqrt{\epsilon_{\text{eff}}}, \quad (3.35)$$

where  $k_0 = 2\pi/\lambda$  is the wavenumber in free space. The attenuation constant  $\alpha$ , which can be split into contributions arising from the conductor ( $\alpha_c$ ) and the dielectric ( $\alpha_d$ ) depends mainly on the geometry of the CPW. In general, losses decrease with both increasing center conductor width  $w$  and substrate thickness  $h$ .

## 3.4 Network Analysis

### 3.4.1 Two-Port Networks

A network, in the context of electronics, is an interconnection of electrical devices such as resistors, inductors, capacitors, transistors, filters, mixers, amplifiers, transmission lines, voltage sources, current sources, and switches. Network analysis is the process of finding the voltages across and the currents through every component in the network.

For this purpose, devices and networks are generally represented as black boxes. A pair of terminals providing access to a component is called port if the port condition is fulfilled: the current entering one terminal is equal to the current leaving the other. In this thesis, it is exclusively dealt with devices which have two pairs of terminals both meeting the port condition, so-called two-port networks. Fig. 3.4 shows such a two-port network.

### 3.4.2 Scattering Parameters

To describe a linear device or network, various types of alternative parameter sets are available. In the low-frequency domain, one can choose from impedance para-

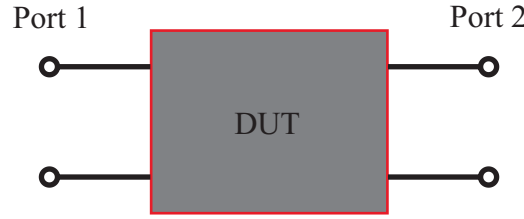


**Fig. 3.4:** Black-box representation of a two-port device under test (DUT).

parameters (Z-parameters), admittance parameters (Y-parameters), hybrid parameters (H-parameters), inverse hybrid parameters (G-parameters), and ABCD-parameters. These are usually expressed in matrix notation, and establish relations between the total voltages and currents at the ports. However, at rf or microwave frequencies, their application is inappropriate for several reasons. First, above frequencies of 300 MHz, the phase of voltage or current changes significantly over the physical extent of a component because the wavelength becomes comparable to the device dimensions. Second, ideal open ( $Z = \infty$ ) and short ( $Z = 0$ ) circuits required for the measurement cannot be realized at rf frequencies. Moreover, undesired antenna effects have to be considered.

Consequently, another approach is applied, which is based on complex power waves at  $50 \Omega$  terminations: the scattering parameter, or S-parameter, approach. Impedances of  $50 \Omega$  cannot only be realized much easier than open or short circuit terminations, but also represent a good compromise between both extremes. Most rf and microwave hardware is currently designed and specified for  $50 \Omega$  operation [81].

S-parameters are complex, frequency-dependent quantities that can be measured conveniently using state-of-the-art network analyzers which will be discussed in detail in section 3.5. Fig. 3.5 shows a two-port network with incident and reflected power waves at each port, as well as the corresponding signal flow graph, which provides a graphical illustration of the network behavior. According to Ref. [82], the incident and reflected complex power waves  $a_i$  and  $b_i$  at port  $i$  are defined as

$$a_i = \frac{V_i + Z_i I_i}{2\sqrt{|\operatorname{Re}(Z_i)|}}, \quad (3.36)$$

$$b_i = \frac{V_i - Z_i^* I_i}{2\sqrt{|\operatorname{Re}(Z_i)|}}, \quad (3.37)$$

where  $V_i$  and  $I_i$  are the voltage and current flowing into port  $i$ , and  $Z_i$  is the reference impedance at port  $i$  (the asterisk denotes the complex conjugate). For most measurements, it is convenient to assume that there is only a single positive real impedance at all ports,  $Z_0 = 50 \Omega$ , which simplifies the definition of the incident and reflected waves to

$$a_i = \frac{V_i + Z_0 I_i}{2\sqrt{Z_0}}, \quad (3.38)$$

$$b_i = \frac{V_i - Z_0 I_i}{2\sqrt{Z_0}}. \quad (3.39)$$

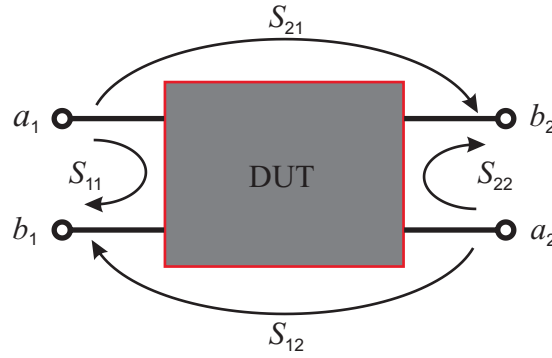


**Fig. 3.5:** Relation between the S-parameters and the complex power waves  $a_i$  and  $b_i$  of a two-port network.

The unit of the waves  $a_i$  and  $b_i$  is  $\sqrt{W}$ . Therefore, the incident and reflected power at any port  $i$  is given by  $|a_i|^2$  and  $|b_i|^2$ , respectively.

The relationship between the reflected waves  $b_i$ , the incident waves  $a_j$ , and the scattering parameters  $S_{ij}$  for a  $N$ -port network is given by the following equation:

$$b_i = \sum_{j=1}^N S_{ij} a_j \quad (i = 1, \dots, N). \quad (3.40)$$

Therefore, the reflected waves at any port can be described as a linear combination of the incident waves at all ports. Using a matrix representation, this set of  $N$  linear equations can be summarized as

$$[b] = [S] [a], \quad (3.41)$$

where  $[b]$  and  $[a]$  are  $N$ -dimensional column vectors, and  $[S]$ , the scattering matrix, is a  $N \times N$  matrix consisting of  $N^2$  scattering parameters. Each S-parameter is defined as the ratio of the outgoing wave  $b_i$  at port  $i$  to the incident wave  $a_j$  at port  $j$  under the condition that any other port  $k \neq j$  is terminated into a non-reflecting load matching the characteristic impedance  $Z_0$  (i.e.,  $a_k = 0$ ):

$$S_{ij} = \left. \frac{b_i}{a_j} \right|_{a_k=0 \text{ for } k \neq j} \quad (i, j = 1, \dots, N). \quad (3.42)$$

Thus,  $S_{ii}$  is the reflection coefficient at port  $i$ , and  $S_{ij}$  is the transmission coefficient from port  $j$  to port  $i$  when all ports other than the port of the input signal are terminated into matched loads, respectively.

A full set of S-parameters completely characterizes any linear device under test (DUT). A one-port network is hence described by only one S-parameter, a two-port network by four S-parameters, and a three-port network by nine S-parameters.

Using Eq. (3.40), a two-port network is described by the two linear equations

$$b_1 = S_{11}a_1 + S_{12}a_2 \quad (3.43)$$

$$b_2 = S_{21}a_1 + S_{22}a_2, \quad (3.44)$$

which can be expressed in matrix notation as

$$\begin{bmatrix} b_1 \\ b_2 \end{bmatrix} = \begin{bmatrix} S_{11} & S_{12} \\ S_{21} & S_{22} \end{bmatrix} \begin{bmatrix} a_1 \\ a_2 \end{bmatrix}. \quad (3.45)$$

The respective scattering matrix consists of four elements: the input and output reflection coefficients  $S_{11}$  and  $S_{22}$ , as well as the forward and reverse transmission coefficients  $S_{12}$  and  $S_{21}$ .

Networks can have the following characteristics which can be used to simplify their analysis [71]:

- A device or network is said to be reciprocal if interchanging a pair of input and output ports does not change the respective transmission properties. In this case, the scattering matrix  $[S]$  is symmetric which means  $S_{ij} = S_{ji}$ , or  $[S] = [S]^T$  where  $[S]^T$  is the transpose to  $[S]$ . In general, a network will be reciprocal if it consists entirely of linear passive components such as resistors, capacitors, or inductors. Non-reciprocal networks contain active components such as transistors, or magnetically biased ferrites or plasmas.
- A network is termed symmetrical if input and output ports can be interchanged without altering the voltages or currents at each port. Therefore, for symmetrical networks  $S_{ii} = S_{jj}$ .
- For a lossless network, the total incident power is equal to the total reflected power, or  $\sum |a_i|^2 = \sum |b_i|^2$ . The scattering matrix of a lossless network is unitary which means  $[I] - [S][S]^H = 0$ , where  $[S]^H$  is the conjugate transpose of  $[S]$ , and  $[I]$  the identity matrix.
- A network is said to be lossy if the total reflected power is less than the total incident power. The difference is the power dissipated in the network. In this case,  $\sum |b_i|^2 < \sum |a_i|^2$  and  $[I] - [S][S]^H \geq 0$ .

### 3.4.3 Scattering Transmission Parameters

The Z-, Y-, and S-parameter representations can be used to characterize networks with an arbitrary number of ports, whereas G-, H-, and ABCD-parameters are limited to two ports. In practice, however, many networks consist of cascaded two-port networks in which the output waves of one network are identical to the input waves of the next. In this case, it is convenient to define a  $2 \times 2$  transmission matrix for each two-port network. The transmission matrix of all cascaded two-port networks can then be found by multiplying the transmission matrices of each individual two-port network.



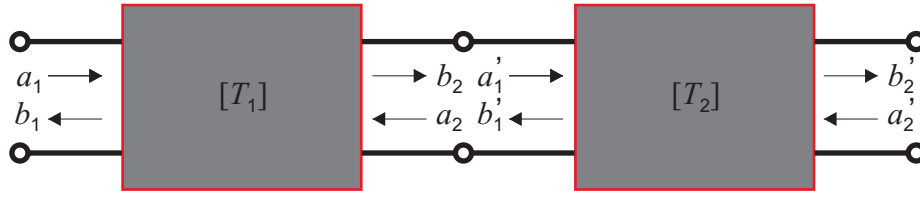


**Fig. 3.6:** Cascade connection of two two-port networks.

For describing rf or microwave networks, scattering transfer parameters, or T-parameters, are used which, like scattering parameters, are defined in terms of incident and reflected power waves as

$$\begin{bmatrix} b_1 \\ a_1 \end{bmatrix} = \begin{bmatrix} T_{11} & T_{12} \\ T_{21} & T_{22} \end{bmatrix} \begin{bmatrix} a_2 \\ b_2 \end{bmatrix}. \quad (3.46)$$

The difference is that T-parameters relate the waves at Port 1 to the waves at Port 2 whereas S-parameters relate the reflected waves to the incident waves. In this respect, T-parameters fill the same role as ABCD-parameters which are used for the description of networks operating at low-to-moderate frequencies.

In the cascade connection of two two-port networks shown in Fig. 3.6, the first two-port network is described by Eq. (3.46) and the second one by

$$\begin{bmatrix} b'_1 \\ a'_1 \end{bmatrix} = \begin{bmatrix} T'_{11} & T'_{12} \\ T'_{21} & T'_{22} \end{bmatrix} \begin{bmatrix} a'_2 \\ b'_2 \end{bmatrix}. \quad (3.47)$$

As it can be seen, the power waves at the output port of the first network are identical to the ones at the input port of the second network which allows to substitute Eq. (3.47) in Eq. (3.46). The T-matrix of the overall network is then given by

$$[T] = [T_1] [T_2], \quad (3.48)$$

where  $[T_1]$  and  $[T_2]$  are the T-matrices of the individual networks. This procedure can be extended to any number of cascaded two-port networks. The order of multiplication of the T-matrices must be the same as the order in which the networks are arranged, since matrix multiplication is, in general, not commutative.

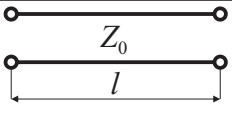

T-parameters are not that easy to measure like S-parameters which can be directly obtained from network analyzers. However, T-parameters can be easily converted into S-parameters and vice versa using the following equations [83]:

$$\begin{bmatrix} T_{11} & T_{12} \\ T_{21} & T_{22} \end{bmatrix} = \begin{bmatrix} \frac{S_{12}S_{21} - S_{11}S_{22}}{S_{21}} & \frac{S_{11}}{S_{21}} \\ -\frac{S_{22}}{S_{21}} & \frac{1}{S_{21}} \end{bmatrix}, \quad (3.49)$$

$$\begin{bmatrix} S_{11} & S_{12} \\ S_{21} & S_{22} \end{bmatrix} = \begin{bmatrix} \frac{T_{12}}{T_{22}} & \frac{T_{11}T_{22} - T_{12}T_{21}}{T_{22}} \\ \frac{1}{T_{22}} & -\frac{T_{12}}{T_{22}} \end{bmatrix}. \quad (3.50)$$

Tab. 3.1 shows the matrices of two selected circuit components, which will be needed later for data evaluation.

**Tab. 3.1:** S- and T-matrices of selected circuit components [84].

Component	S-matrix	T-matrix
Transmission line of length $l$ and characteristic impedance $Z_0$ 	$\begin{bmatrix} 0 & e^{-\gamma l} \\ e^{-\gamma l} & 0 \end{bmatrix}$	$\begin{bmatrix} e^{-\gamma l} & 0 \\ 0 & e^{\gamma l} \end{bmatrix}$
Change of characteristic impedance from $Z_1$ to $Z_2$ 	$\begin{bmatrix} \frac{Z_2 - Z_1}{Z_2 + Z_1} & \frac{2\sqrt{Z_2 Z_1}}{Z_2 + Z_1} \\ \frac{2\sqrt{Z_2 Z_1}}{Z_2 + Z_1} & \frac{Z_1 - Z_2}{Z_2 + Z_1} \end{bmatrix}$	$\begin{bmatrix} \frac{Z_1 + Z_2}{2\sqrt{Z_2 Z_1}} & \frac{Z_2 - Z_1}{2\sqrt{Z_2 Z_1}} \\ \frac{Z_2 - Z_1}{2\sqrt{Z_2 Z_1}} & \frac{Z_1 + Z_2}{2\sqrt{Z_2 Z_1}} \end{bmatrix}$

A network can be represented by any of the six parameter sets described in this section. However, sometimes the representation by means of another parameter set can be useful. Tables for the conversion from any two-port parameter set to another one can be found in [83, 85].

## 3.5 Vector Network Analyzer

### 3.5.1 Introduction

Network analyzers are most commonly used in communications and electrical engineering to characterize single rf and microwave devices or even entire networks of those in terms of scattering parameters. Since the typical operational frequencies of such devices lie in the GHz range and are identical to the ones in which magnetization dynamics occurs, network analyzers are perfectly suited devices for its investigation.

Various types of network analyzers exist which are quite different in their measurement capabilities. Scalar network analyzers (SNAs), for instance, are the least expensive ones, but also provide the least information by only being able to measure amplitudes. In contrast, vector network network analyzers (VNAs) have the added capability to detect the phase of a signal which is very important as both kinds of information are required to fully characterize a device or network. Moreover, the availability of the phase information unlocks many new features for complex measurements such as Smith charts, group delay, and time domain. Vector error correction, which improves measurement accuracy by removing the effects of inherent measurement-system errors, also requires phase information to build an effective error model. Furthermore, the measurement of the phase enables the calculation of both real and imaginary part of the dynamic susceptibility  $\chi$ .

### 3.5.2 Principle of Operation

In this thesis, an Agilent PNA E8364B two-port VNA with a frequency range of 10 MHz to 50 GHz has been used. Its principle architecture is schematically shown in Fig. 3.7.

The network analyzer's built-in hf source [synthesized voltage-controlled oscillator (VCO)] generates a sinusoidally swept, stepped, or continuous-wave signal with a

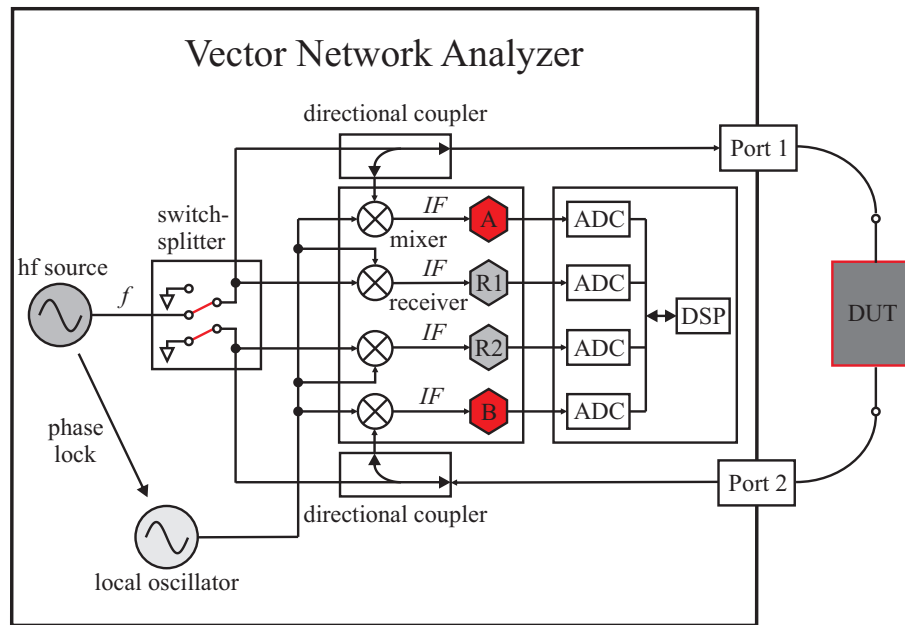


**Fig. 3.7:** Fundamental architecture of a VNA as used for a measurement of  $S_{21}$  and  $S_{11}$ .

frequency  $f$  between 10 MHz and 50 GHz. The maximum leveled source output power depends on the chosen frequency range and lies between +5 dBm and  $-10$  dBm. This signal then passes through a two-way solid-state switch splitter which fulfills two functions. First, it switches between the Port 1 and Port 2 measurement paths, automatically enabling alternate forward and reverse measurements. Thereby an internal termination for the measurement port that is inactive is provided. Second, it splits the hf signal into a test port signal and a reference signal. The test port signal goes into the through-line arm of a directional coupler, and from there out through one of the test ports to the DUT. The coupled arm of the directional couplers carries the signal reflected from or transmitted through the DUT to the receiver A or B, respectively. The reference signal is routed directly to the appropriate receiver R1 or R2.

For detecting and processing signals, the VNA uses a tuned receiver approach in which an additional, local yttrium-iron-garnet (YIG) oscillator (LO) is phase locked to the reference signal  $f$ . In a first step, the first LO signal is mixed with the reference, transmitted, and reflected hf signals to a first intermediate frequency (IF) signal in the single-digit MHz range. The first IF signal is filtered using a band pass filter, which narrows the receiver bandwidth and greatly improves sensitivity and dynamic range. Moreover, if applicable, it is amplified in order to increase the signal-to-noise ratio (SNR). In a second step taking place in the receiver modules A, B, R1, and R2, the first IF signal is mixed with the second LO signals to produce a constant second IF signal at 41.667 kHz. Finally, analog-to-digital converters (ADC) and digital signal processing (DSP) are applied to extract magnitude and phase information from the IF signals. More details about the architecture of a VNA can be found in [86, 87].

The measurement speed of the VNA is mainly determined by the number of data

points as well as the IF bandwidth and only depends to a smaller extent on the chosen frequency range. For instance, a complete frequency sweep from 10 MHz to 30 GHz at an IF bandwidth of 35 kHz using 3201 points takes approximately 96 ms, which corresponds to 30  $\mu\text{s}$ /point. If using the averaging function to increase the (SNR), this time has to be multiplied by the number of averaging cycles.

### 3.5.3 Calibration and Error Correction

Every measurement made with a VNA typically includes three different types of errors: systematic errors, random errors, and drift errors [88].

Systematic errors are caused by hardware imperfections in the VNA and test equipment. Assuming that these errors are time invariant and repeatable, they can be characterized through calibration and mathematically removed during the measurement process. Example of systematic errors are not perfectly directive couplers, signal leakage due to finite insulation, and parasitic reflections at discontinuities.

Random errors are unpredictable, vary as a function of time, and can thus not be removed by calibration. The main contributions to random errors stem from instrument noise (e.g., the IF noise floor) as well as switch and connector repeatability. Noise errors can often be reduced by increasing source power, narrowing the IF bandwidth, or by averaging over multiple sweeps. Furthermore, it is advantageous to use a torque wrench for tightening coaxial connectors and adapters in order to achieve repeatability and to extend connector life. Some torque wrench designs encompass a break-over feature which prevents over-torquing of a coupled junction.

Drift errors occur when a test system's performance changes after a calibration has been performed. They are primarily caused by temperature variation and can be removed by recalibration. The rate of drift determines how frequently additional calibrations are needed. However, by constructing a test environment with stable ambient temperature, drift errors can usually be minimized.

For performing a calibration, the VNA is connected to a calibration kit consisting of a set of standards such as short, open, load, and thru. These provide the reference for vector error correction as each of them has a precisely known definition stored in the VNA that includes electrical delay, impedance, and loss. The VNA then measures all the standards and compares the results with their ideal models. From this data, the error terms of the chosen error model are calculated which are finally used to remove the effects of systematic errors from subsequent measurements. The signal flow graph of a possible two-port network error model is shown in Fig. 3.8. It assumes that the four scattering parameters can be determined by a reflection and a transmission measurement, respectively, in both forward ( $S_{11m}, S_{21m}$ ) and reverse ( $S_{12m}, S_{22m}$ ) direction. For each of the two signal propagation directions, six error

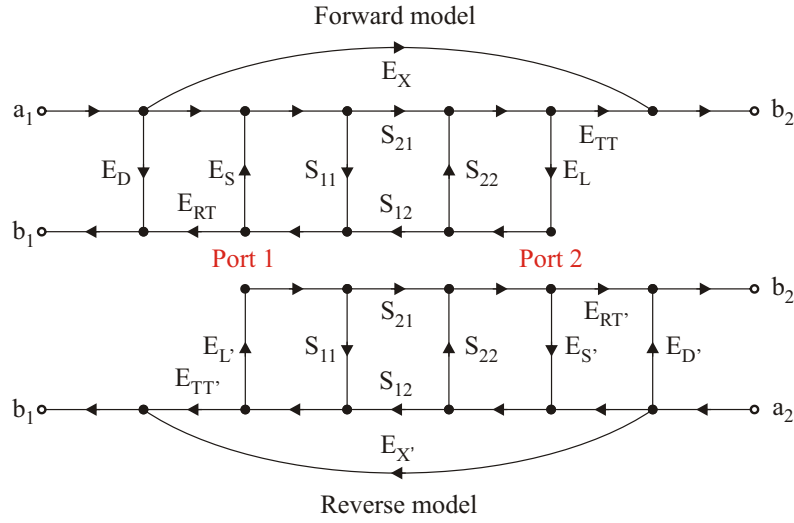


**Fig. 3.8:** Two-port error correction model.

terms occur according to the model which have the following meaning [88]:

$E_S, E_{S'}$  = Forward/Reverse Source Mismatch

$E_L, E_{L'}$  = Forward/Reverse Load Mismatch

$E_X, E_{X'}$  = Forward/Reverse Crosstalk

$E_D, E_{D'}$  = Forward/Reverse Directivity

$E_{RT}, E_{RT'}$  = Forward/Reverse Reflection Tracking

$E_{TT}, E_{TT'}$  = Forward/Reverse Transmission Tracking.

Since a total of 12 unknown error terms are taken into account, this model is also called 12-term error model. When performing measurements using the calibration, each actual S-parameter, which is a function of all four measured S-parameters  $S_{ijm}$  and the 12 error terms, is given by the following equations [88]:

$$S_{11} = \frac{\left(\frac{S_{11m}-E_D}{E_{RT}}\right) \left(1 + \frac{S_{22m}-E_{D'}}{E_{RT'}} E_{S'}\right) - E_L \left(\frac{S_{21m}-E_X}{E_{TT}}\right) \left(\frac{S_{12m}-E_{X'}}{E_{TT'}}\right)}{\left(1 + \frac{S_{11m}-E_D}{E_{RT}} E_S\right) \left(1 + \frac{S_{22m}-E_{D'}}{E_{RT'}} E_{S'}\right) - E_{L'} E_L \left(\frac{S_{21m}-E_X}{E_{TT}}\right) \left(\frac{S_{12m}-E_{X'}}{E_{TT'}}\right)} \quad (3.51)$$

$$S_{21} = \frac{\left(\frac{S_{21m}-E_X}{E_{TT}}\right) \left(1 + \frac{S_{22m}-E_{D'}}{E_{RT'}} (E_{S'} - E_L)\right)}{\left(1 + \frac{S_{11m}-E_D}{E_{RT}} E_S\right) \left(1 + \frac{S_{22m}-E_{D'}}{E_{RT'}} E_{S'}\right) - E_{L'} E_L \left(\frac{S_{21m}-E_X}{E_{TT}}\right) \left(\frac{S_{12m}-E_{X'}}{E_{TT'}}\right)} \quad (3.52)$$

$$S_{12} = \frac{\left(\frac{S_{12m}-E_{X'}}{E_{TT'}}\right) \left(1 + \frac{S_{11m}-E_D}{E_{RT}} (E_S - E_{L'})\right)}{\left(1 + \frac{S_{11m}-E_D}{E_{RT}} E_S\right) \left(1 + \frac{S_{22m}-E_{D'}}{E_{RT'}} E_{S'}\right) - E_{L'} E_L \left(\frac{S_{21m}-E_X}{E_{TT}}\right) \left(\frac{S_{12m}-E_{X'}}{E_{TT'}}\right)} \quad (3.53)$$

$$S_{22} = \frac{\left(\frac{S_{22m}-E_{D'}}{E_{RT'}}\right) \left(1 + \frac{S_{11m}-E_D}{E_{RT}} E_S\right) - E_{L'} \left(\frac{S_{21m}-E_X}{E_{TT}}\right) \left(\frac{S_{12m}-E_{X'}}{E_{TT'}}\right)}{\left(1 + \frac{S_{11m}-E_D}{E_{RT}} E_S\right) \left(1 + \frac{S_{22m}-E_{D'}}{E_{RT'}} E_{S'}\right) - E_{L'} E_L \left(\frac{S_{21m}-E_X}{E_{TT}}\right) \left(\frac{S_{12m}-E_{X'}}{E_{TT'}}\right)} \quad (3.54)$$

At the point where the calibration standards are connected, a reference or calibration plane is created. However, lots of measurement setups do not allow to

connect a DUT directly to the test ports of the VNA, but require additional test fixtures, adapters, or interconnecting cables. For the highest measurement accuracy, the reference planes should be located where the DUT is connected in order to remove the errors associated with the test setup. If this is not possible, the measured S-parameters do not only include the response of the DUT, but that of part of the test setup as well. Since only the DUT characteristics are of interest, a de-embedding process has to be performed which mathematically removes the test fixture contribution to the overall measurement [89]. More details about this step can be found in section 5.1.3. This approach does not allow for real-time feedback because the measured data needs to be captured and post-processed in order to remove the effects of the test fixture. If real-time de-embedded measurements are required, the process of de-embedding two-port networks can be performed directly on the VNA making use of its vector error correction capabilities.

As the number of DUT ports increases, the required number of calibration measurements also increases. When using mechanical calibration standards, this leads to a significantly higher probability of bad connections and bad calibrations. Moreover, test port cable repeatability and stability errors are amplified. For this reason, an electronic calibration kit (ECal) has been used in this thesis which is an all-in-one solution requiring only two connections in the case of a two-port network. The various impedance states, typically four, in the ECal modules are switched with PIN-diode or FET switches, so the calibration standards never wear out. The characteristics of these impedance states are stored in the ECal module and can be read by the VNA or a PC controller to perform a calibration. The provided accuracy is excellent, with results generally better than SOLT (Short-Open-Load-Thru) calibration, but somewhat less than a properly performed TRL (Thru-Reflect-Line) calibration [90].

# 4 The Experimental VNA-FMR Setups

In this chapter, the VNA-FMR technique and its experimental realization are presented. In order to underline the advantages of VNA-FMR, the chapter begins with a comparison of conventional FMR and VNA-FMR. In the following, an extensive description of the two VNA-FMR spectrometers built within this thesis is given.

## 4.1 Conventional Ferromagnetic Resonance

One of the most established and most commonly used techniques to study magnetization dynamics is conventional ferromagnetic resonance (FMR). Microwave radiation with a fixed frequency in the range of 1–80 GHz generated by a Klystron or a Gunn diode is coupled into a resonant cavity with a magnetic sample mounted inside. Depending on the used frequency band, different types of cavities such as rectangular or cylindrical resonators are employed. Within the cavity, the sample can be brought into several positions in order to realize different pumping geometries. By sweeping the external magnetic field generated by an electromagnet, the sample can be driven through ferromagnetic resonance at which the absorption of microwave power by the sample is maximum. The absorbed power, given by

$$P_{\text{abs}} = \pi f \chi'' \int_{\text{sample}} |\vec{h}_{\text{rf}}|^2 dV, \quad (4.1)$$

is directly proportional to the imaginary part  $\chi''$  of the dynamic magnetic susceptibility. In order to enhance the SNR, the external magnetic field is additionally modulated with amplitudes of up to  $B = 0.2$  mT at frequencies of 100–200 Hz which allows for lock-in detection.

Due to its very high SNR of 90 and sensitivity of  $10^{13} \mu_B$  [91] arising from the high quality factors of the employed resonators, conventional FMR is excellently suited to study spin waves in bulk magnetic material as well as extended thin films with single-domain configurations. The disadvantage of this technique is its limitation to a fixed frequency by the cavity. However, this problem can be solved by using a vector network analyzer and a coplanar waveguide as discussed in the next section.

## 4.2 Vector Network Analyzer Ferromagnetic Resonance

A novel approach to investigate magnetization dynamics at high frequencies is vector network analyzer ferromagnetic resonance (VNA-FMR). In contrast to conventional FMR, it offers the possibility to sweep the frequency of the oscillating magnetic field that excites the precession of the magnetization at a constant external bias field. In this way, the magnetization state is conserved, which is beneficial for the investigation of magnetic samples with complex domain configuration or effects such as exchange bias. For this purpose, a high-bandwidth CPW is employed instead of a microwave cavity with a fixed resonance frequency. The VNA, which acts as both source and detector of the sinusoidal rf signal, sweeps the frequency of the outgoing signal across a specified frequency range. If the excitation frequency matches the resonance frequency of the sample at a given bias field, microwave power is absorbed in order to maintain the precessional motion of the magnetization. Moreover, the phase of the signal is shifted by  $\pi$  at resonance leading to a destructive interference with the incident signal. Together with the attenuation in the cables connecting VNA and CPW, this leads to a decrease of the amplitude of the transmitted signals. With a VNA-FMR spectrometer, it is of course also possible to measure the dynamic response of a sample by sweeping the external field through resonance at a fixed excitation frequency, just as for conventional FMR.

In order to increase the SNR of the VNA-FMR technique, a reference measurement is performed. By applying an in-plane magnetic field perpendicular to the CPW, the magnetization of the sample is pinned parallel to the excitation field. As a consequence, the precession of the magnetization is suppressed. Subsequently, the reference data is subtracted from the measurement at an applied bias field.

## 4.3 Construction and Components of the VNA-FMR Spectrometers

Within this thesis, two VNA-FMR spectrometers have been built. The one shown in Fig. 4.1a, VNA-FMR Setup 1, was set up first and was rather simply designed, mainly served to get hands-on experience with this new technique and to produce first scientific results. It used a pair of Helmholtz coils to generate an external in-plane magnetic bias field with  $B_{\max} = 0.08$  T, which in turn limited the maximum usable frequency to 15 GHz. Angle-dependent measurements were not possible with this spectrometer.

However, these drawbacks were overcome with the construction of a second, much more sophisticated VNA-FMR Setup 2, depicted in Fig. 4.1b. It utilizes an electromagnet, which can generate magnetic fields up to  $B = 2.2$  T, is capable of polar and azimuthal angle-dependent measurements, and is fully automated. In the following, the several components of both setups will be discussed in detail.



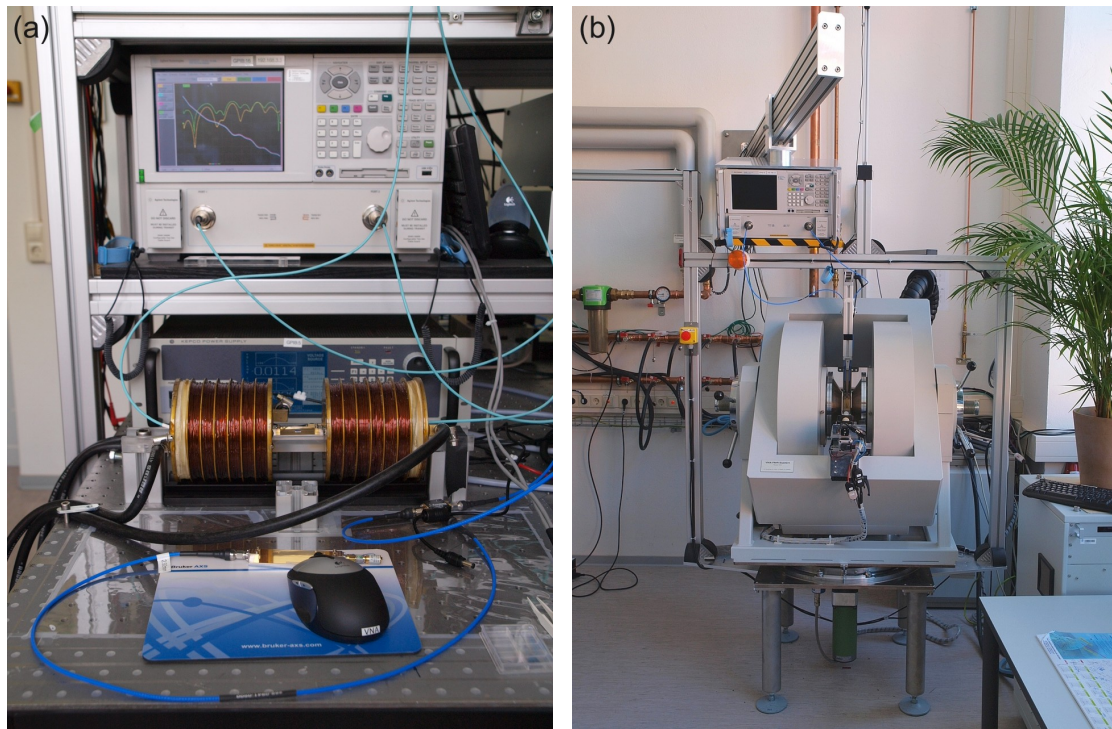


**Fig. 4.1:** The two VNA-FMR spectrometers constructed within this thesis: (a) Setup 1 and (b) Setup 2.

### 4.3.1 Magnet Systems

To generate the external magnetic bias fields for the VNA-FMR setups, two different approaches have been used.

For VNA-FMR Setup 1, a pair of Helmholtz coils connected in series was employed. Their maximum generated magnetic field was limited by the voltage available from the power supply (Kepco BOP 10-100MG) to approximately  $B = 0.08$  T. Because of ohmic losses in the coils, the power supply was operated in current control mode, which automatically adjusts the voltage to maintain a given current value. Moreover, water cooling was required to remove the heat generated by the ohmic losses that would otherwise heat up the surrounding parts of the setup and would lead to a decrease of the available current.

For VNA-FMR Setup 2, a commercial electromagnet (Bruker B-E 25v) capable of generating much higher fields was chosen. Its main component is a H-yoke magnet consisting of magnetically soft steel of low C-, P-, and S-content. The air gap is continuously adjustable and the pole pieces can be locked in any position, thus allowing for rapid and simple air gap variation. Three cooling discs are mounted on two soft iron cylinders which in turn are fitted into the two yoke arms, resulting in two coil chambers for the energizing coils. Heat generated in the energizing coils is removed through a cooling system requiring only normal tap water. The energizing coils are protected from overheating by thermal relays, which automatically turn off the power supply if the temperature exceeds a certain limit. The two coils attached

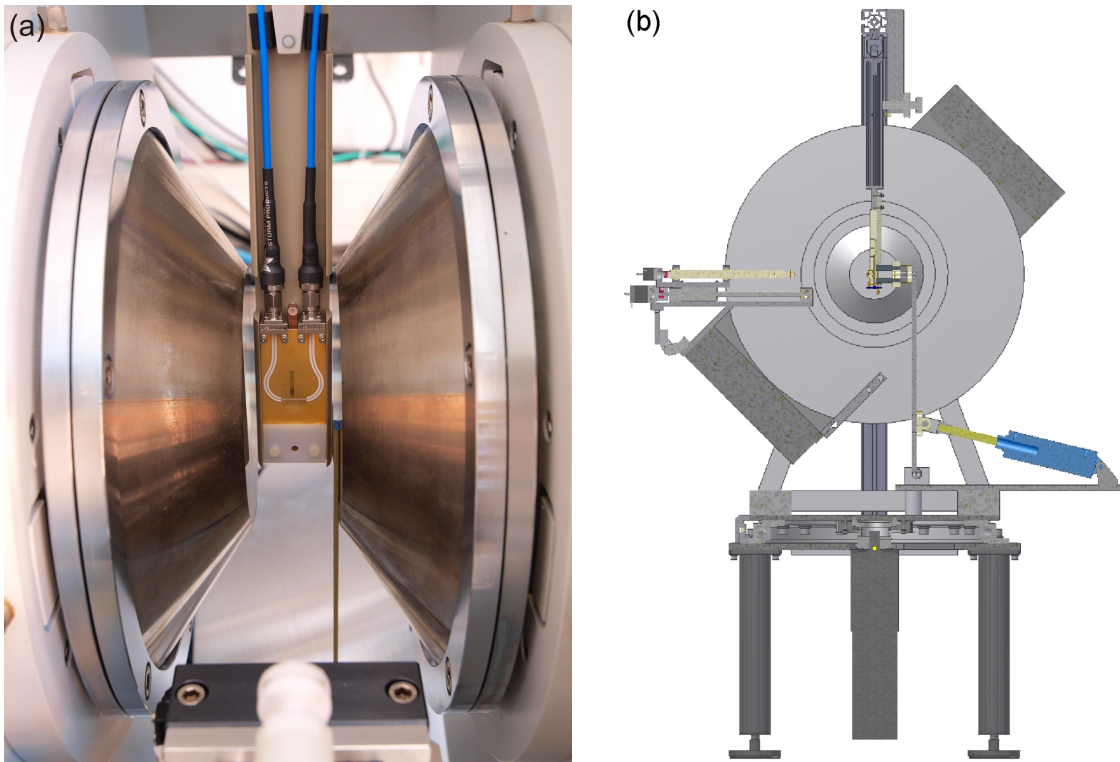


**Fig. 4.2:** (a) CPW located in the 40 mm gap between the two tapered pole caps. To the right pole cap, a transversal hall probe is attached. (b) Cross-section view of VNA-FMR Setup 2 with the pneumatic cylinder (right), the reference magnets and the CPW holder (center), and the azimuthal sample holder (left).

to each of the poles are taken separately to the outside, where they can be connected for either series or parallel operation. The magnet is fixed on a trunnion mount enabling rotation about the field axis. The yoke position is set to  $45^\circ$  representing the best compromise between air gap accessibility, space consumption, and mounting of additional parts for the VNA-FMR setup. The other main component of the electromagnet is the bipolar power supply (BSMPS BIP 200/60 4Q) offering 4-quadrant operation, and delivering maximum voltages of  $\pm 200$  V and a maximum current of 60 A. Its control unit (B-EC1) is equipped with a 20 bit ADC/DAC as well as various interfaces and allows for either field- or current-controlled operation. The field control unit (B-HHz) covering a range of  $\pm 2.2$  T with a resolution of  $10 \mu\text{T}$  is connected to a digital teslameter (Projekt Elektronik Berlin FM 3000-BB-10). Its transversal probe is attached to the center of the magnet's right pole cap and has an accuracy of 0.01 % or better. The actual field value is read out in real time and is shown on the display of the power supply controller.

The maximum field at  $I = 60$  A without pole caps at 10 mm air gap amounts to  $B = 2.2$  T, which is enough to saturate Fe. However, since this gap width is too small to house a CPW including connectors and cables, tapered pole caps of 100 mm diameter are used in addition, which allow to increase the gap to 40 mm while reaching the same field value (see Fig. 4.2a).

To perform reference measurements, a pair of NdFeB permanent magnets is employed in both VNA-FMR setups, respectively. The magnets are spaced a couple of centimeters apart and their stray fields of approximately 100 mT are used to pin the magnetization of the samples parallel to the microwave excitation field. In the case of VNA-FMR Setup 1, the magnets are put manually above the CPW with the sample located in their center. For VNA-FMR Setup 2, the reference magnets are automatically moved by a pneumatic cylinder from their idle position to a cut-out on the backside of the swiveling CPW holder (see Fig. 4.2b).

### 4.3.2 Coplanar Waveguides

The most crucial part of a VNA-FMR spectrometer is probably the CPW. Its importance does not only lie in providing the excitation field for the precessional motion of the magnetization, but it determines the usable frequency range and the SNR as well.

Upon designing a CPW, multiple aspects (geometrical, electrical, mechanical, physical) have to be considered in order to get the optimum result for a given purpose. First, the CPW should have a characteristic impedance of  $Z_0 = 50 \Omega$  in order to ensure maximum power transfer and to prevent losses due to undesirable reflections. Second, the width of the center conductor has to be small enough to provide a sufficiently high excitation field amplitude. Third, based on the desired mechanical stability, a suitable substrate thickness has to be chosen. Deciding upon the substrate material itself, its physical properties such as relative permittivity, loss tangent, and thermal conductivity have to be taken into account. Finally, the CPW layout should comply with the design rules of the manufacturer.

The CPWs employed within this thesis have been designed, simulated, and optimized by a rf engineering company according to the desired specifications and have been manufactured using state-of-the-art technologies. In principle, it would have been possible to perform the design process by oneself. But as electromagnetic simulation software is expensive, complex, and requires a certain level of training and experience to produce accurate and reliable results, it was decided to better have this done by professionals.

The types of transmission lines used in both VNA-FMR setups are grounded coplanar waveguides (GCPWs), which are shown in Fig. 4.3. Both of them have dimensions of 50 mm  $\times$  30 mm and are made from alumina ( $\text{Al}_2\text{O}_3$  99.5%) with a thickness of 0.254 mm (Type 1) and 0.381 mm (Type 2), respectively. The length of the CPWs represents a trade-off between end launch connectors and rf cable ends being preferably positioned far away from the regions of highest magnetic fields and losses due to increasing center conductor length. Their width is limited by the 40 mm gap between the pole caps and is set to provide 5 mm space on either side for the rotation of the electromagnet and the Hall probe attached to the right pole cap.

The metallization on either side of the CPWs consists of 50 nm of TiW followed by 3  $\mu\text{m}$  of Au. The latter is chosen to be greater than the skin depth in order to keep attenuation due to conduction loss small. Thereby, gold was given the preference over copper since it is not prone to corrosion. The width  $w$  of the center conductor

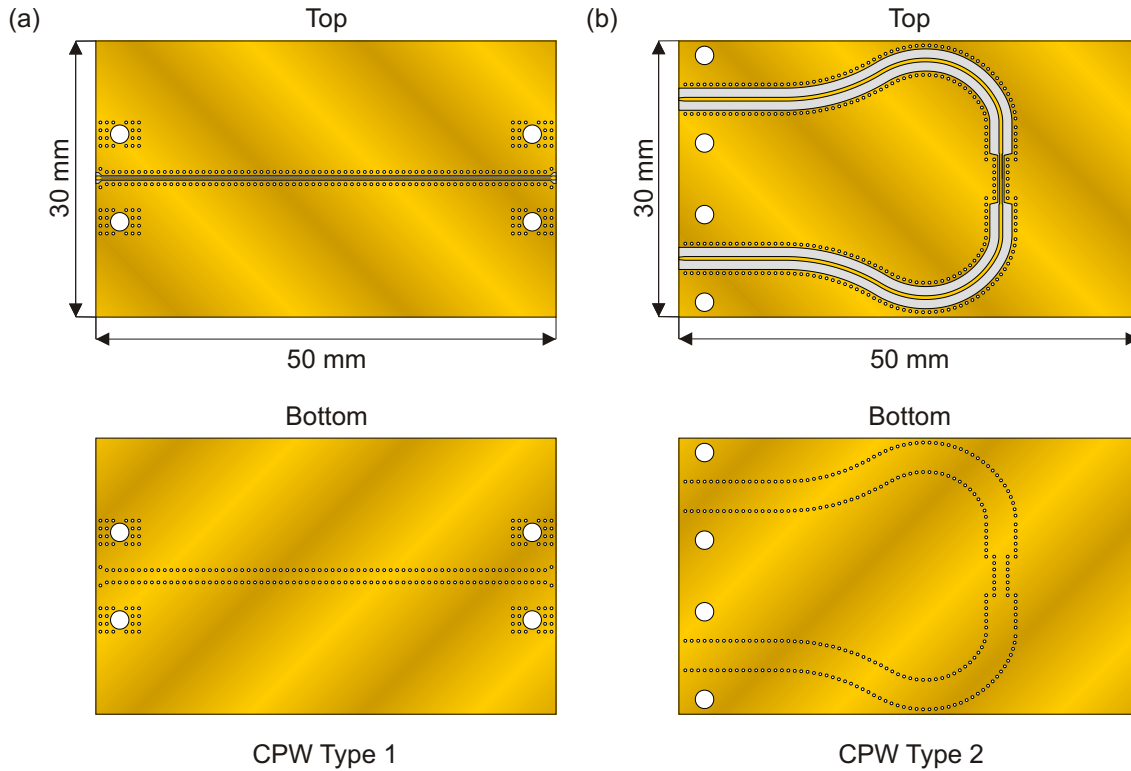


**Fig. 4.3:** Top and bottom view of the CPWs employed in (a) VNA-FMR Setup 1 and (b) VNA-FMR Setup 2.

amounts to 100  $\mu\text{m}$  and 200  $\mu\text{m}$  for CPW Type 1 and Type 2, respectively. The big holes at either end of the center conductor allow for inserting 2.4 mm female or male end launch connectors (Southwest Microwave, Model Numbers 1492-01A-5 and 1492-02A-5). The small holes in both structures are metal-filled vias.

The center conductor of CPW Type 1 runs straight from one end to the other, whereas for CPW Type 2 it is U-shaped. The latter is due to the fact that the 40 mm gap between the pole caps of the electromagnet is not only too narrow to horizontally accommodate two end launch connectors, but also offers not enough space to connect microwave cables and not to bend them beyond their minimum bending radius. Furthermore, it is not possible to drill two holes into the pole caps and the H-yoke to provide a cable feed-through. For these reasons, the center strip starts and ends at the upper edge of the CPW, which allows to attach the two end launch connectors in a vertical position and offers best accessibility within the electromagnet. The transition from the two vertical center conductor sections to the short horizontal one is realized by wide bends, which finally gives rise to the U shape. Another point in which both types of CPW differ from each other is that the width of the center conductor and the gaps to ground are not constant throughout the entire CPW Type 2, but reduce in the short straight section where the sample is located. The purpose of this variable geometry is to decrease losses connected with the rather long center conductor (about 90.8 mm). Therefore, the feed lines are designed for a low stray field, whereas the section for the DUT has a three times

larger stray field in air. Both geometries are optimized for a nonreflecting transition and the near fields close above the substrate. A point that has to be addressed as well in the context of optimum performance is the rf launch section [79]. Since the metal pins of the end launch connectors introduce an additional capacitance, the width of the center strip was narrowed in order to compensate for this. This method is called *tapering* and involves adjusting the length of the launch taper and the final dimension at the edge of the substrate, all of which is best done by using electromagnetic (EM) simulation software.

As described in section 3.3.2, the current traveling along the CPW generates a transverse magnetic field above the conductors and a perpendicular field near their edges (see Fig. 3.3). The amplitudes of both fields can be approximated by the Karlqvist equations [92]:

$$h_{\parallel} = -\frac{\mu_0}{\pi} \frac{i}{2w} \left[ \arctan\left(\frac{(w/2) + x}{z}\right) + \arctan\left(\frac{(w/2) - x}{z}\right) \right], \quad (4.2)$$

$$h_{\perp} = -\frac{\mu_0}{\pi} \frac{i}{4w} \log \frac{(x+w)^2 + y^2}{(x-w)^2 + y^2}. \quad (4.3)$$

For CPW Type 1 with a center conductor width of 100  $\mu\text{m}$  and a microwave input power of 0 dBm (= 1 mW), which corresponds to a current of  $I = 4.5$  mA, the amplitudes are calculated to  $h_{\parallel} \approx 28$   $\mu\text{T}$  in the middle of the center conductor 1  $\mu\text{m}$  above the metalization and to  $h_{\perp} \approx 16$   $\mu\text{T}$  in the middle of the gap between center conductor and ground planes. The real values are lower since the current density across the CPW is nonuniform and the signal attenuation in the microwave cables has not been taken into account. A more precise estimation, such as in Refs. [91, 93], requires a simulation using EM software. However, these amplitudes are small enough to ensure that the excitation only leads to small cone angles of the precessional motion and that data analysis in the linear regime of the LLG equation is justified.

The S-parameters of CPW Type 1 for a frequency range of 10 MHz to 15 GHz are shown in Fig. 4.4 and 4.5. According to Tab. 3.1, it is expected that the transmission parameters  $S_{21}$  and  $S_{12}$  are equal to  $e^{-\gamma l_{\text{CPW}}}$  and the reflection parameters  $S_{11}$  and  $S_{22}$  are both zero. As the CPW is a reciprocal device,  $S_{21}$  and  $S_{12}$  coincide and their logarithmic magnitudes decrease from 0 dB at 10 MHz to  $-3.5$  dB at 15 GHz, which is attributed to losses due to the rather long center conductor. For the phase, a continuous decrease with increasing frequency is observed. As it will be shown in section 5.1.4, magnitude and phase of the transmission parameters  $S_{ij}$  are related to the real and imaginary part of the propagation constant  $\gamma$  as follows:

$$\text{Re}(\gamma) = \alpha = -\frac{\ln(|S_{ij}|)}{l_{\text{CPW}}}, \quad (4.4)$$

$$\text{Im}(\gamma) = \beta = -\frac{\arg(S_{ij})}{l_{\text{CPW}}}. \quad (4.5)$$

By fitting the slope of the phase of  $S_{21}$ , the phase velocity is calculated to  $v_P \approx 114000$  km/s. From Eqs. (3.32) and (3.35), the relative permeability of

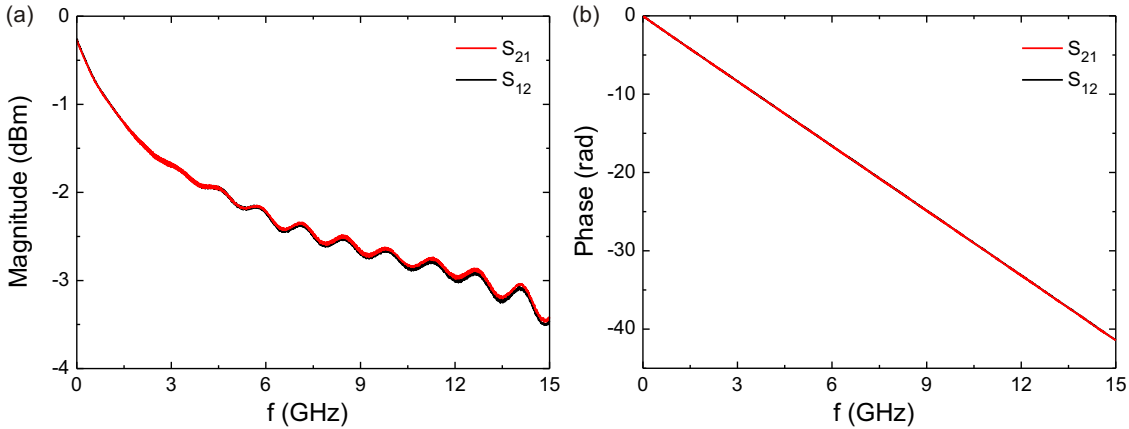


**Fig. 4.4:** Magnitude (a) and phase (b) of the transmission parameters  $S_{21}$  and  $S_{12}$  of CPW Type 1 in the frequency range of 10 MHz to 15 GHz.

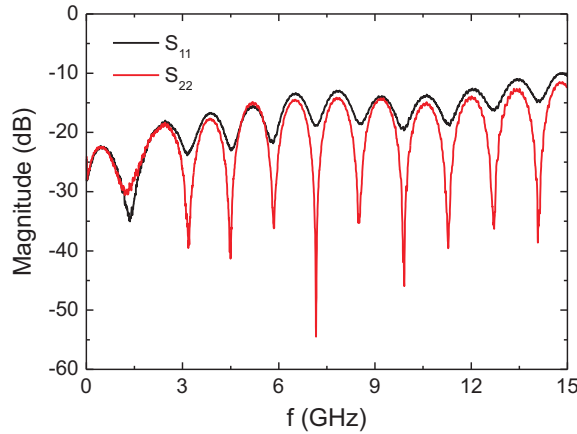


**Fig. 4.5:** Magnitude of the reflection parameters  $S_{11}$  and  $S_{12}$  of CPW Type 1 in the frequency range of 10 MHz to 15 GHz.

the substrate is determined to  $\epsilon_r = 12.9$ , which is larger than the value of  $\epsilon_r = 9.9$  given by the manufacturer.

The reflection parameters  $S_{11}$  and  $S_{22}$  differ somewhat from each other which is most likely caused by finite calibration errors. Their amplitudes are always below  $-10$  dB and thus,  $S_{11}$  and  $S_{22}$  can be considered as zero in good approximation. At frequencies which are integer multiples of approximately 1.36 GHz, a strong decrease of their amplitudes can be observed, which is slightly more pronounced for  $S_{22}$ . The same feature is also visible in a different way as oscillations in the transmission parameters. Using the phase velocity of the CPW, the corresponding wavelength is determined to  $\lambda = 8.4$  cm. Since the S-parameters of another CPW Type 1 with a length of  $l_{\text{CPW}} = 8$  cm show a similar behavior and lead to the same wavelength, dimensional resonances, which would occur at frequencies whose wavelength is an integer multiple of the CPW length, can be ruled out. Instead, it is supposed that the reflections are caused by an impedance mismatch between the CPW and the rest of the microwave equipment. This mismatch is probably caused by

manufacturing tolerances, which can amount up to 10 %. From microscopic images, the center conductor width  $w$  and the gap to the grounds have been determined to be 100  $\mu\text{m}$  and 70  $\mu\text{m}$ , respectively. This yields a characteristic impedance of  $Z_0 = 54 \Omega$  which explains the observed reflections. Another contribution to these resonances might stem from a non-optimized rf launch section [79]. However, despite this issue, the CPWs have been used without any problems for measurements up to 15 GHz, whereby this value was determined by the maximum magnetic field generated by the two Helmholtz coils.

The S-parameters of CPW Type 2 are quite similar to the ones of Type 1. Although there is no frequency limit on the part of the electromagnet, its practical use was limited to frequencies in the range of 20–25 GHz. The reason for this is that above these frequencies, the transmission characteristics of the CPW gets significantly noisier and drastically deteriorates. On the one hand, this is caused by the difficulties in making a calibration at such high frequencies. On the other hand, it is supposed that antenna effects contribute as well since the total length of the center conductor is almost 91 mm.

The CPW employed in VNA-FMR Setup 2 is attached to a plastic mounting that vertically extends into the magnet. It can be swiveled out of the magnet by up to 90° and locked in any position in order to make adjustments. The mounting also provides guidance for the microwave cables and is equipped with an end switch to ensure the CPW is exactly aligned vertically for measurements. The mounting itself is connected to a frame made from aluminum profiles. For enhanced mechanical stability, the latter are connected to the wall located behind the electromagnet.

In VNA-FMR Setup 1, a rod with milling grooves is used to house the CPW and microwave cables. The rod is connected by two short aluminum profiles to an optical table such that the CPW is located right in the middle between the two Helmholtz coils.

### 4.3.3 Sample Holders for Angle-Dependent Measurements

The unique feature of VNA-FMR Setup 2 is its capability to perform both polar and azimuthal angle-dependent measurements, which allows for a much more precise investigation of magnetic anisotropies.

Polar measurements can be realized by either vertically rotating CPW and sample inside the magnet or by rotating the magnetic around them since exciting rf field and external bias field always have to be perpendicular. Despite of the heavy weight of the magnet, the second option has been pursued which was not only easier to implement from the engineering point of view, but also prevents unfavorable twisting and bending of the microwave cables as it would have occurred in option one. For this purpose, a gearbox with a transmission ratio of 10 to 1 is used that easily rotates the magnet by 100° clockwise and counterclockwise, respectively, with a resolution of 1°. At +100° and –100°, two end switches are located which when reached stop further rotation of the magnet. At 0°, a photoelectric barrier is installed that is used to determine the reference position of the electromagnet. To quickly read off the actual position of the electromagnet, an indicator and a degree disk are attached to

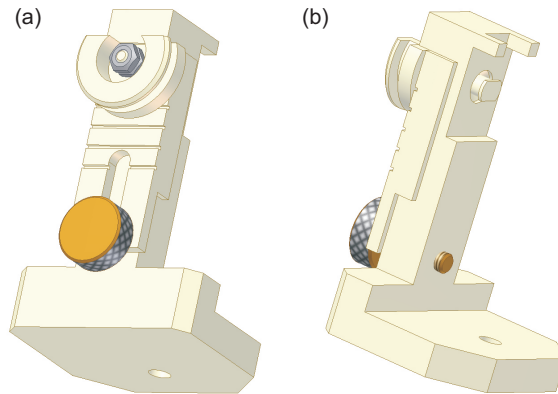


**Fig. 4.6:** Front (a) and rear (b) view of the sample holder for polar measurements.

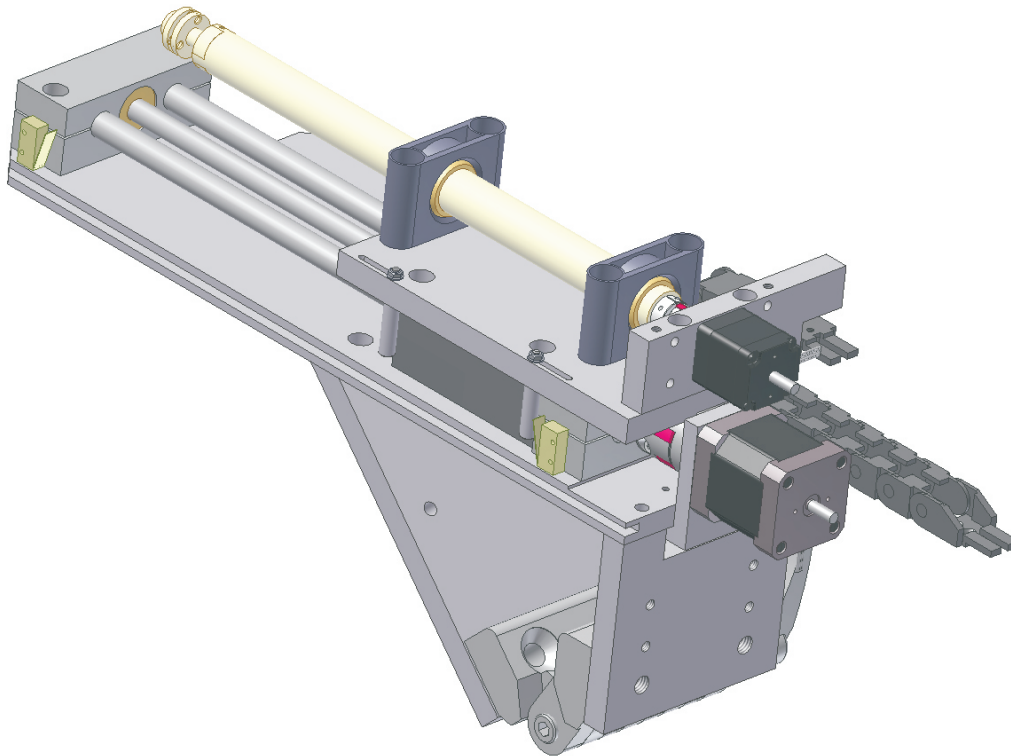


**Fig. 4.7:** Sample holder for azimuthal measurements.

its frame.

The sample holder for polar measurements, depicted in Fig. 4.6, is mounted at the bottom of the CPW holder. It uses a stamp to which the sample is attached by double-sided adhesive tape. The stamp can be brought into an upper position 5 mm away from the CPW and into a lower one in which the sample is in contact with it.

For azimuthal measurements, during which the sample is rotated in-plane, the magnet is positioned at  $0^\circ$  and another sample holder, shown in Fig. 4.7, is used. This one consists of a plastic rod with a removable head that can be rotated around its axis by a linear motor, all of which are mounted onto a sliding carriage powered by a second linear motor. The rod can make an arbitrary number of revolutions with



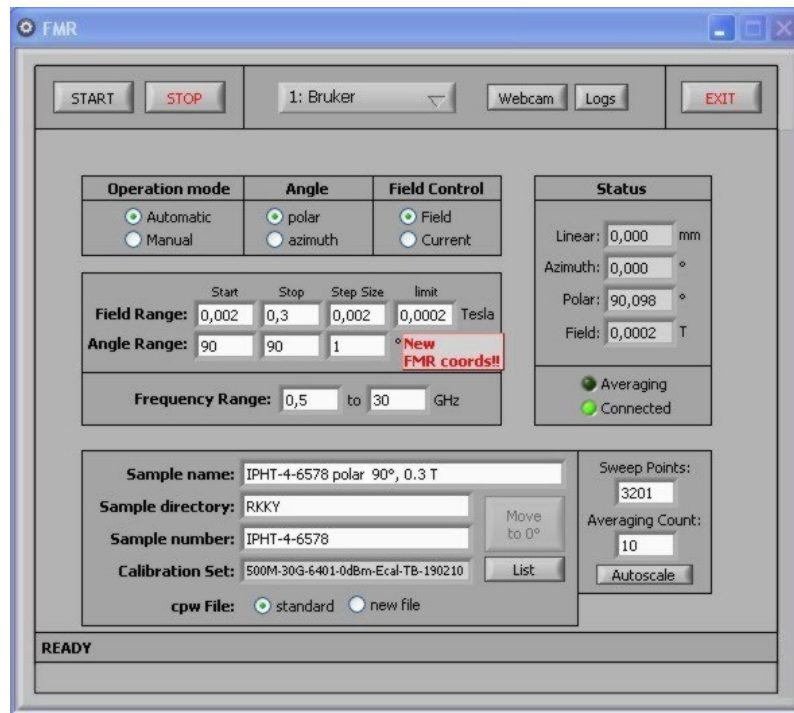


**Fig. 4.8:** Screenshot of the control software of VNA-FMR Setup 2 for frequency-swept mode of operation.

an accuracy of better than  $1^\circ$ . The removable head of the rod is made of two pieces connected by three nonmagnetic beryllium springs that should prevent scratching and damaging the CPW. Like for the polar sample holder, double-sided adhesive tape is used to mount a sample to the head of the rod. A switch on the right-hand side of the sliding carriage allows to manually move it back and forth, which is required for bringing the sample in contact with the CPW. On the left-hand side two end switches are located, which stop the motion of the sliding carriage when it reaches its idle position or comes to close to the CPW, respectively. The entire azimuthal sample holder is mounted onto the yoke of the magnet, can be flipped in and out of the magnet, and can be locked in any position.

#### 4.3.4 Automation and Control Software

The two VNA-FMR setups built in this thesis have been automated in order to make the measurement process as fast and convenient as possible. For this purpose, an automation software using LabVIEW has been written that controls three different setups: VNA-FMR Setup 1 and 2 as well as a wafer-prober setup. In addition, the software allows to check or modify the settings of all individual components and to operate them manually.

The control window of VNA-FMR Setup 2 is depicted in Fig. 4.8. The upper panel allows to select the operation and field control mode as well as the type of angle-dependent measurement. In the panel below, the frequency, field, and angle range and their corresponding step size can be specified. In the lower panel, the

sample name and number as well as the directory in which the data will be saved can be entered. Moreover, the number of sweep points and averaging cycles can be chosen and it can be selected from a list of calibration sets. Furthermore, there is the option to measure the S-parameters of the empty CPW, which is necessary each time a new calibration has been made. The panel in the upper right corner provides information about the status of the VNA and displays the actual values of the polar and azimuthal angles, the magnetic field, and the position of the azimuthal sample holder.

Polar measurements start with a reference measurement unless it is desired to measure the empty CPW which will then be performed first. This is followed by a reference run of the magnet around its  $0^\circ$  position and the rotation of the magnet to the starting angle. After setting the magnetic field to its specified value, the S-parameters are measured and the magnet moves one step further. After the measurement has finished, the magnetic field is set back to zero, the magnet rotates back to its original position, and the data is copied from the VNA to the control PC.

The first step of an azimuthal measurement is to bring sample and CPW in contact. This is done by manually rotating the sample into the  $0^\circ$  position and then approaching the CPW using the switch for the linear motor on the right-hand side of the sliding carriage. The software memorizes the position at which the contact is made for the rest of the measurement and always moves the sample 5 mm away from the CPW to rotate it one step further. Since the sample changes its position relative to the CPW with every new angle, it is necessary to perform a reference measurement each time.

# 5 Data Evaluation: From S-Parameters to Magnetic Susceptibility

This chapter deals with the evaluation of the raw data acquired by two-port VNA-FMR measurements. First, the method used in this thesis to convert the S-parameters into the dynamic magnetic susceptibility will be described in detail. Second, other data evaluation methods will be briefly introduced. Finally, the accuracy of all these methods will be addressed.

## 5.1 Full Two-Port Data Evaluation

The evaluation method used in this thesis has recently been developed by Bilzer *et al.* [84], but is principally based on works published already several decades ago [94–96]. It is a transmission/reflection method in which the sample is put on top of the CPW, or generally speaking, inserted into a segment of a transmission line. From the S-parameters of the CPW segment loaded with the sample, the relative permeability, relative permittivity, and finally the dynamic susceptibility of the sample can be determined. In the following, the different evaluation steps will be outlined.

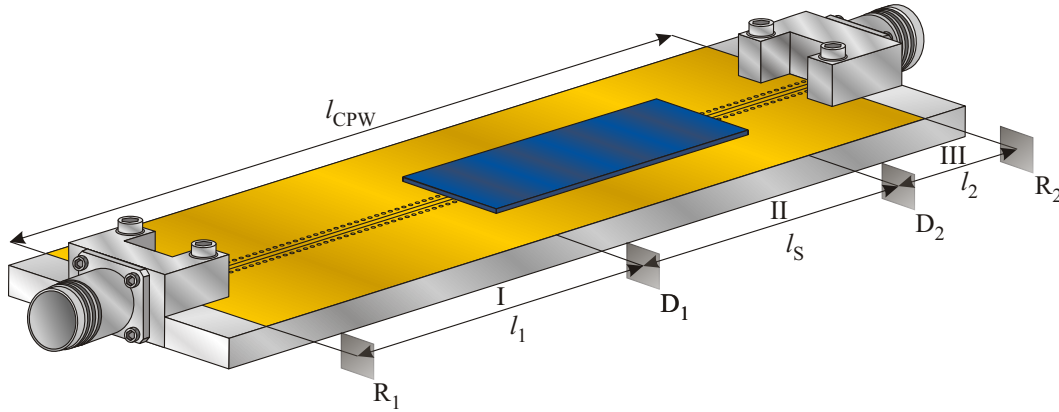
### 5.1.1 Raw Data: S-Parameter

Fig. 5.1 shows the typical measurement configuration. The CPW, equipped with two 2.4 mm end launch connectors, is connected to rf cables at the calibration reference planes  $R_1$  and  $R_2$ , and loaded with a sample of length  $l_S$ , unknown relative permittivity  $\epsilon_r$ , and unknown relative permeability  $\mu_r$ . The reference planes  $R_1$  and  $R_2$  are determined by the points at which the E-Cal kit has been connected to the rf cables. The CPW is designed to have a characteristic impedance of  $Z_0 = 50 \Omega$  in the free space regions (I and III), which when loaded with the sample (II) becomes  $Z$ , where

$$Z = Z_0 \sqrt{\frac{\mu_r}{\epsilon_r}}. \quad (5.1)$$

In the unloaded regions, the propagation constant is  $\gamma_0 = \omega \sqrt{\mu_0 \epsilon_0}$ , while in the loaded region, it is given by

$$\gamma = \gamma_0 \sqrt{\mu_r \epsilon_r}. \quad (5.2)$$



**Fig. 5.1:** CPW loaded with a magnetic sample of length  $l_S$ .

At the boundaries between the regions I and II, and the regions II and III, there will be reflections due to the impedance mismatch. The reflection coefficient ( $\Gamma$  or  $-\Gamma$ , respectively) is given by

$$\Gamma = \frac{Z - Z_0}{Z + Z_0}. \quad (5.3)$$

Combining the above three equations allows to extract the relative permeability and the relative permittivity which are then given by

$$\epsilon_r = \frac{\gamma}{\gamma_0} \frac{1 + \Gamma}{1 - \Gamma}, \quad (5.4)$$

$$\mu_r = \frac{\gamma}{\gamma_0} \frac{1 - \Gamma}{1 + \Gamma}. \quad (5.5)$$

These two equations are part of the *Nicolson–Ross–Weir* (NRW) algorithm [94, 95], the most commonly used method to calculate permeability and permittivity. It can be seen that  $\mu_r$  and  $\epsilon_r$  only depend on  $\Gamma$  and  $\gamma$ , quantities which can be determined from the S-parameters measured with the VNA. In order to get an analytical expression for the S-parameters, the two-port network consisting of the CPW loaded with the sample is split into the following five segments, each representing an individual two-port network:

- Region I of the CPW with length  $l_1$  between the left 2.4 mm connector and the left edge of the sample
- Impedance change from  $Z_0$  to  $Z$  at the left edge of the sample
- Region II of the CPW loaded with a sample of length  $l_S$
- Impedance change from  $Z$  back to  $Z_0$  at the right edge of the sample
- Region III of the CPW with length  $l_2$  between the right edge of the sample and the right 2.4 mm connector.

The T-matrices of every section are given in Tab. 3.1. As described in Sec. 3.4.3, the T-matrix of the entire network is found by multiplying the T-matrices of every individual section of the CPW:

$$[\mathbf{T}] = \begin{bmatrix} e^{-\gamma_0 l_1} & 0 \\ 0 & e^{\gamma_0 l_1} \end{bmatrix} \begin{bmatrix} \frac{1}{\sqrt{1-\Gamma^2}} & \frac{\Gamma}{\sqrt{1-\Gamma^2}} \\ \frac{\Gamma}{\sqrt{1-\Gamma^2}} & \frac{1}{\sqrt{1-\Gamma^2}} \end{bmatrix} \times \begin{bmatrix} e^{-\gamma l_S} & 0 \\ 0 & e^{\gamma l_S} \end{bmatrix} \begin{bmatrix} \frac{1}{\sqrt{1-\Gamma^2}} & \frac{-\Gamma}{\sqrt{1-\Gamma^2}} \\ \frac{-\Gamma}{\sqrt{1-\Gamma^2}} & \frac{1}{\sqrt{1-\Gamma^2}} \end{bmatrix} \begin{bmatrix} e^{-\gamma_0 l_2} & 0 \\ 0 & e^{\gamma_0 l_2} \end{bmatrix}. \quad (5.6)$$

Converting the T-matrix into an S-matrix using Eq. (3.49) gives the desired description of the two-port network:

$$\begin{bmatrix} S_{11} & S_{12} \\ S_{21} & S_{22} \end{bmatrix} = \begin{bmatrix} R_1^2 \frac{\Gamma(1-T^2)}{1-T^2\Gamma^2} & R_1 R_2 \frac{T(1-\Gamma^2)}{1-T^2\Gamma^2} \\ R_1 R_2 \frac{T(1-\Gamma^2)}{1-T^2\Gamma^2} & R_2^2 \frac{\Gamma(1-T^2)}{1-T^2\Gamma^2} \end{bmatrix}, \quad (5.7)$$

where

$$R_1 = e^{-\gamma_0 l_1}, \quad (5.8)$$

$$R_2 = e^{-\gamma_0 l_2} \quad (5.9)$$

are the reference plane transformations, and

$$T = e^{-\gamma l_S} \quad (5.10)$$

is the transmission coefficient.

### 5.1.2 Correction of Sample Position

From Eq. (5.7), it can be seen that the two-port network is reciprocal as its transmission parameters  $S_{12}$  and  $S_{21}$  are equal. Thus, it is sufficient for further evaluation to only use one of both transmission parameters,  $S_{21}$ . However, the reflection parameters  $S_{11}$  and  $S_{22}$  are generally different which is caused by the sample not being exactly aligned in the center of the CPW ( $l_1 \neq l_2$ ), leading to different reference plane transformations  $R_1$  and  $R_2$ . This can be corrected mathematically by calculating the geometric mean of  $S_{11}$  and  $S_{22}$ :

$$S_{11/22} = \sqrt{S_{11}S_{22}} = R_1 R_2 \frac{\Gamma(1-T^2)}{1-T^2\Gamma^2}. \quad (5.11)$$

$S_{11/22}$  and  $S_{21}$  now have the same reference plane transformations  $R_1 R_2 = e^{-\gamma_0(l_1+l_2)}$ . This term contains the sum of the two unloaded regions of the CPW which is equal to the length of the CPW minus the sample length:  $l_1 + l_2 = l_{\text{CPW}} - l_S$ . In this way, a possible misalignment of the sample can be corrected.

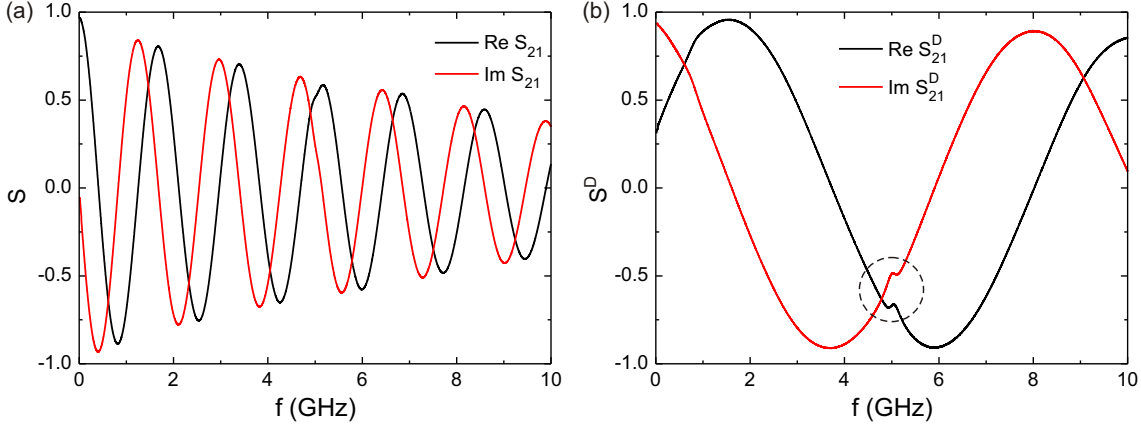


**Fig. 5.2:** Comparison of the measured (a) and the de-embedded (b) transmission parameters  $S_{21}$  and  $S_{21}^D$  of a 20 nm thick Py film at an applied field of 40 mT. After the de-embedding process, the resonance at  $f = 4.98$  GHz becomes clearly visible.

### 5.1.3 De-embedding

As described in Sec. 3.5.3, the VNA is calibrated at the coaxial interface representing the reference plane. Thus, the measured S-parameters are those of CPW and sample together. Since only the sample properties are of interest, the CPW's rf characteristics have to be removed from the measured results. This can be done by performing a de-embedding process which shifts the reference planes from the edges of the CPW ( $R_1$  and  $R_2$ ) to the edges of the sample ( $D_1$  and  $D_2$ ). The de-embedding procedure is done mathematically by multiplying  $S_{21}$  and  $S_{11/22}$  with the inverse of  $R_1 R_2$ . For this purpose, the propagation constant  $\gamma_0$  has to be determined, which can be obtained from measuring the transmission parameter  $S_{21}^{\text{CPW}}$  of the CPW without any sample. In this case, the CPW represents nothing but a impedance matched transmission line of length  $l_{\text{CPW}}$ . According to Tab. 3.1, the transmission parameter  $S_{21}^{\text{CPW}}$  is given by

$$S_{21}^{\text{CPW}} = e^{-\gamma_0 l_{\text{CPW}}} = R_1 R_2 e^{-\gamma_0 l_S}, \quad (5.12)$$

from which the inverse of  $R_1 R_2$  can be calculated as

$$(R_1 R_2)^{-1} = e^{\gamma_0 (l_{\text{CPW}} - l_S)} = \exp\left(\frac{l_{\text{CPW}} - l_S}{l_{\text{CPW}}} \ln S_{21}^{\text{CPW}}\right). \quad (5.13)$$

The expressions for the two de-embedded S-parameters are then given by

$$S_{21}^D = (R_1 R_2)^{-1} S_{21} = \frac{T(1 - \Gamma^2)}{1 - T^2 \Gamma^2}, \quad (5.14)$$

$$S_{11/22}^D = (R_1 R_2)^{-1} S_{11/22} = \frac{\Gamma(1 - T^2)}{1 - T^2 \Gamma^2}, \quad (5.15)$$

which are now independent of the lengths  $l_1$  and  $l_2$ . A comparison of the measured and the de-embedded transmission parameter  $S_{21}$  and  $S_{21}^D$  of a 20 nm thick Py film

at an applied field of 40 mT is shown in Fig. 5.2.

#### 5.1.4 Extraction of Reflection Coefficient and Propagation Constant

According to the NRW algorithm [94, 95], the reflection coefficient  $\Gamma$  is given by

$$\Gamma = K \pm \sqrt{K^2 + 1}, \quad (5.16)$$

where

$$K = \frac{1 + (S_{11/22}^D)^2 - (S_{21}^D)^2}{2S_{11/22}^D}. \quad (5.17)$$

The appropriate sign in front the root in Eq. (5.16) is chosen such that  $|\Gamma| \leq 1$ . The transmission coefficient  $T$  can be found from  $S_{11/22}^D$ ,  $S_{21}^D$ , and  $\Gamma$ :

$$T = \frac{S_{11/22}^D + S_{21}^D - \Gamma}{1 - (S_{11/22}^D + S_{21}^D)\Gamma}. \quad (5.18)$$

Using Eq. (5.10), the propagation constant  $\gamma$  can then be calculated as

$$\text{Re}(\gamma) = -\frac{\ln(|T|)}{l_s}, \quad (5.19)$$

$$\text{Im}(\gamma) = -\frac{\arg(T)}{l_s}. \quad (5.20)$$

The real part of  $\gamma$  is unique and single valued, whereas the imaginary part of  $\gamma$  is multivalued since adding integer multiples of  $2\pi$  does not change the phase of the transmission coefficient  $T$ . This problem of the phase ambiguity can be solved using either the group delay method [95] or the phase-unwrapping method [97]. In this thesis, the latter one is employed which consists of two steps: determination of the initial phase, and subsequent removal of discontinuities marked by phase jumps of  $2\pi$ . This procedure is implemented in the evaluation software which automatically selects the correct additive constant of  $2\pi n$  for the logarithm of the complex quantity  $T$ , such that  $\arg(T)$  continuously decreases with increasing frequency. For the sake of completeness, it should be noted that there is a similar way to determine  $\Gamma$  and  $\gamma$  using trigonometric functions [96].

#### 5.1.5 Calculation of Permittivity and Permeability

Besides the phase ambiguity discussed above, the NRW algorithm leads to spurious peaks in  $\epsilon_r$  and  $\mu_r$  for low-loss samples at frequencies corresponding to an integer multiple of the half wavelength inside the sample. In this case, the reflection parameters  $S_{11}$  and  $S_{22}$  become very small and their phase uncertainty is rather large, leading to algebraically unstable equations. Possible solutions to eliminate these instabilities are reducing the sample length to less than half of the wavelength or

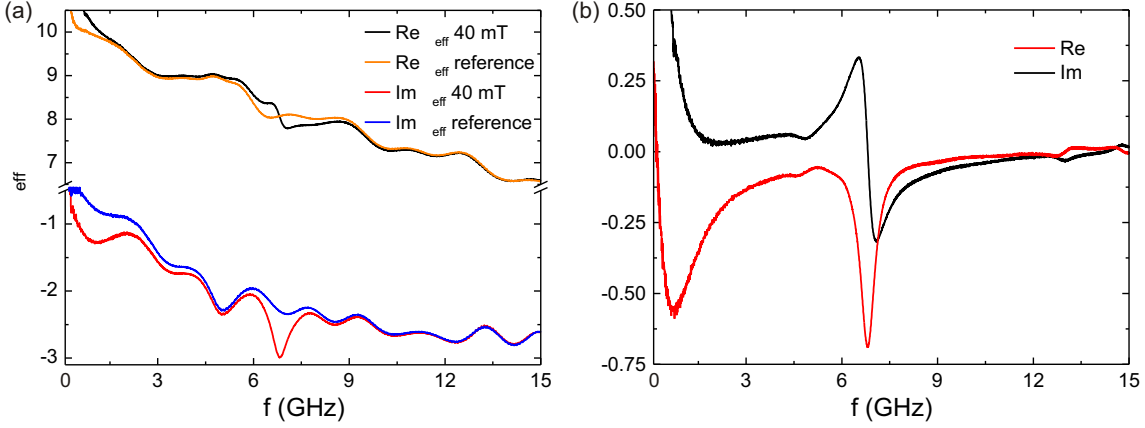


**Fig. 5.3:** (a) Effective permeability  $\mu_{\text{eff}}$  of a Py/Ru/Co trilayer for an applied in-plane field of 40 mT as well as for the corresponding reference measurement and (b) their difference, which is proportional to the dynamic susceptibility  $\chi$ .

using an iterative procedure to determine  $\epsilon_r$  and  $\mu_r$  [98]. However, the practicability of both methods is limited as the former detracts the accuracy and the latter requires an correct estimate of  $\epsilon_r$  and  $\mu_r$  prior to starting the actual calculation of these quantities.

A much more convenient method has been proposed by Boughriet *et al.* [99] which is not only non-iterative and independent of the sample length, but can also be used for various types of transmission lines including CPWs. It uses the same equations as the NRW algorithm to derive  $K, \Gamma, T$ , and  $\gamma$ , but introduces an effective permittivity  $\epsilon_{\text{eff}}$  and an effective permeability  $\mu_{\text{eff}}$ . It is shown that calculating the electromagnetic parameters from equations with terms including  $\Gamma$ , like (5.4) and (5.5), gives rise to inaccuracy peaks. However, calculating  $\epsilon_{\text{eff}}$  or  $\mu_{\text{eff}}$  from an expression exclusively consisting of a term with the propagation constants leads to a complete suppression of the spurious peaks. These results have been combined in the general equation

$$\mu_{\text{eff}} \propto \mu_{\text{eff}}(\epsilon_{\text{eff}})^n = \left(\frac{\gamma}{\gamma_0}\right)^{n+1} \cdot \left(\frac{1-\Gamma}{1+\Gamma}\right)^{n-1}, \quad (5.21)$$

where the exponent  $n$  is a positive or negative real number. It is found that the amplitudes of the inaccuracy peaks decrease as  $n$  approaches the value of one, and completely vanish for  $n = 1$  which simplifies Eq. (5.21) to

$$\mu_{\text{eff}} \propto \left(\frac{\gamma}{\gamma_0}\right)^2. \quad (5.22)$$

The general equation (5.21) includes the Stuchly method [100] ( $n = -1$ ), the NRW method [94,95] ( $n = 0$ ), and Eq. (5.22) [99] ( $n = 1$ ). The derivation of Eq. (5.21) is based on the assumption that the effective permittivity  $\epsilon_{\text{eff}}$  is not a complex number, but only a constant. This condition holds as the calculation of  $\epsilon_r$  of the investigated samples using Eq. (5.4) showed that both its real and imaginary part are practically constant over the measured frequency range, and that  $\text{Re } \epsilon_r \gg \text{Im } \epsilon_r \simeq 0$ . The real



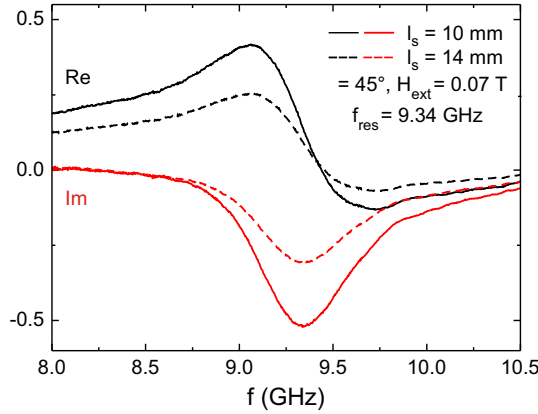


**Fig. 5.4:** Influence of the sample length  $l_S$  on the dynamic susceptibility  $\chi$ .

and imaginary part of the effective permeability  $\mu_{\text{eff}}$  for a Py/Ru/Co trilayer at an applied in-plane field of 40 mT as calculated from Eq. (5.22) are shown in Fig. 5.3a.

The effective permeability  $\mu_{\text{eff}}$  is composed of the relative permeability  $\mu_r$  of the sample and relative permeability of the surrounding materials which is equal to one as these are nonmagnetic. Since  $\mu_{\text{eff}}$  is a linear function of the relative permeability  $\mu_r$ , the rf susceptibility  $\chi$  of the sample is given by

$$\chi = \mu_r - 1 \propto \mu_{\text{eff}} - \mu_{\text{eff}}^{\text{ref}}, \quad (5.23)$$

where  $\mu_{\text{eff}}$  has been calculated from measurements with a magnetic field applied along the CPW, and  $\mu_{\text{eff}}^{\text{ref}}$  belongs to the reference measurement at which a field applied parallel to the exciting microwave field suppresses the resonance. Fig. 5.3b shows an example of the real and imaginary part of the dynamic susceptibility  $\chi$  as calculated from Eq. (5.23).

The two quantities that can be directly derived from  $\chi$  are the ferromagnetic resonance frequency  $f_{\text{res}}$  and the frequency linewidth  $\Delta f$ . Fitting  $f_{\text{res}}$  as a function of the applied magnetic field  $H_{\text{ext}}$ , the effective magnetization, the anisotropy fields and the  $g$ -factor of the sample can be determined. From the frequency linewidth  $\Delta f$ , information about the damping processes can be obtained.

Upon evaluating the data from angular measurements, it has to be considered that the length on which the sample is in contact with the CPW depends on the azimuthal angle unless a circular sample is used. All samples investigated either had a quadratic or rectangular shape, i.e., at  $\varphi = 0^\circ$  the contact length with the CPW is minimum and equal to  $l_S$ , whereas for  $\varphi = 45^\circ$  it is maximum. It was checked whether it is necessary to calculate the appropriate contact length for every angle or if it is sufficient to just use the sample length  $l_S$ , and the result is shown in Fig. 5.4. For this purpose, the susceptibility of a quadratic sample with  $l_S = 10$  mm for an azimuthal angle of  $\varphi = 45^\circ$  has been calculated. It can be seen that the only difference which results from using either  $l_S = 14$  mm, which is the correct value, or  $l_S = 10$  mm is a change in the amplitude of  $\chi$ . However,  $f_{\text{res}}$  and  $\Delta f$  remain unaffected, which is why one value of  $l_S$  can be used for all calculations.

## 5.2 Evaluation Software

The aforementioned full two-port data evaluation method has been implemented into a Matlab program, which also includes a fitting routine for extracting the resonance frequency and linewidth.

A screenshot of the conversion program is depicted in Fig. 5.5a. In the upper half the data input dialog is located, which allows to select the raw data and the corresponding reference files and to set CPW and sample length. If the option “graphical output” is chosen, a pseudocolor plot of the frequency vs. field dependence, displayed in the lower left corner, is created, which offers the possibility to evaluate a measurement at first glance. The panel on the right-hand side provides various options of the pseudocolor plot such as axes settings and color scheme.

A screenshot of the fitting program is shown in Fig. 5.5b. On the left-hand side of the window options for the raw data input are located. These include the selection of a directory containing the converted S-parameters, various sorting criteria such as “field/current”, and the possibility to subtract files from each other. Moreover, it can be chosen whether the real or imaginary part of the dynamic susceptibility  $\chi$  should be plotted in the graph at the bottom and be fitted. Furthermore, the displayed frequency range as well as the minimum and maximum cutoff frequencies (indicated by red and green vertical lines, respectively) for the fitting routine can be specified. The fitted curve (purple) is shown together with the fit parameters on the right-hand side of the window. In order to achieve best results, the type of fit function and weighting options can be selected. In addition, each fit parameter can be accessed and modified manually which allows for fine-tuning.

## 5.3 Other Evaluation Methods

Apart from the full two-port data evaluation presented in the previous section, several other methods to process the raw data can be found in literature. In the following, some of these methods will be briefly outlined.

### 5.3.1 Methods only using $S_{21}$

Kalarickal *et al.* [48] presented a model to analyze two-port VNA-FMR data neglecting reflections. Based on Ref. [96], an uncalibrated microwave permeability parameter

$$U(f) = \pm \frac{i \ln[S_{21-H}(f)/S_{21-ref}(f)]}{\ln[S_{21-ref}(f)]} \quad (5.24)$$

is calculated from the complex transmission parameter  $S_{21}$  of the measurements at an applied magnetic field and of the reference measurement. The sign is chosen such that  $\text{Im}[U(f)]$  is negative in the vicinity of the FMR peak. It is emphasized that  $\text{Re}[U(f)]$  and  $\text{Im}[U(f)]$  are related, but do not correspond strictly to the loss and dispersion profile that would be expected from FMR theory. A combination of additional offsets and distortions occurring in  $U(f)$  is the result of the neglected

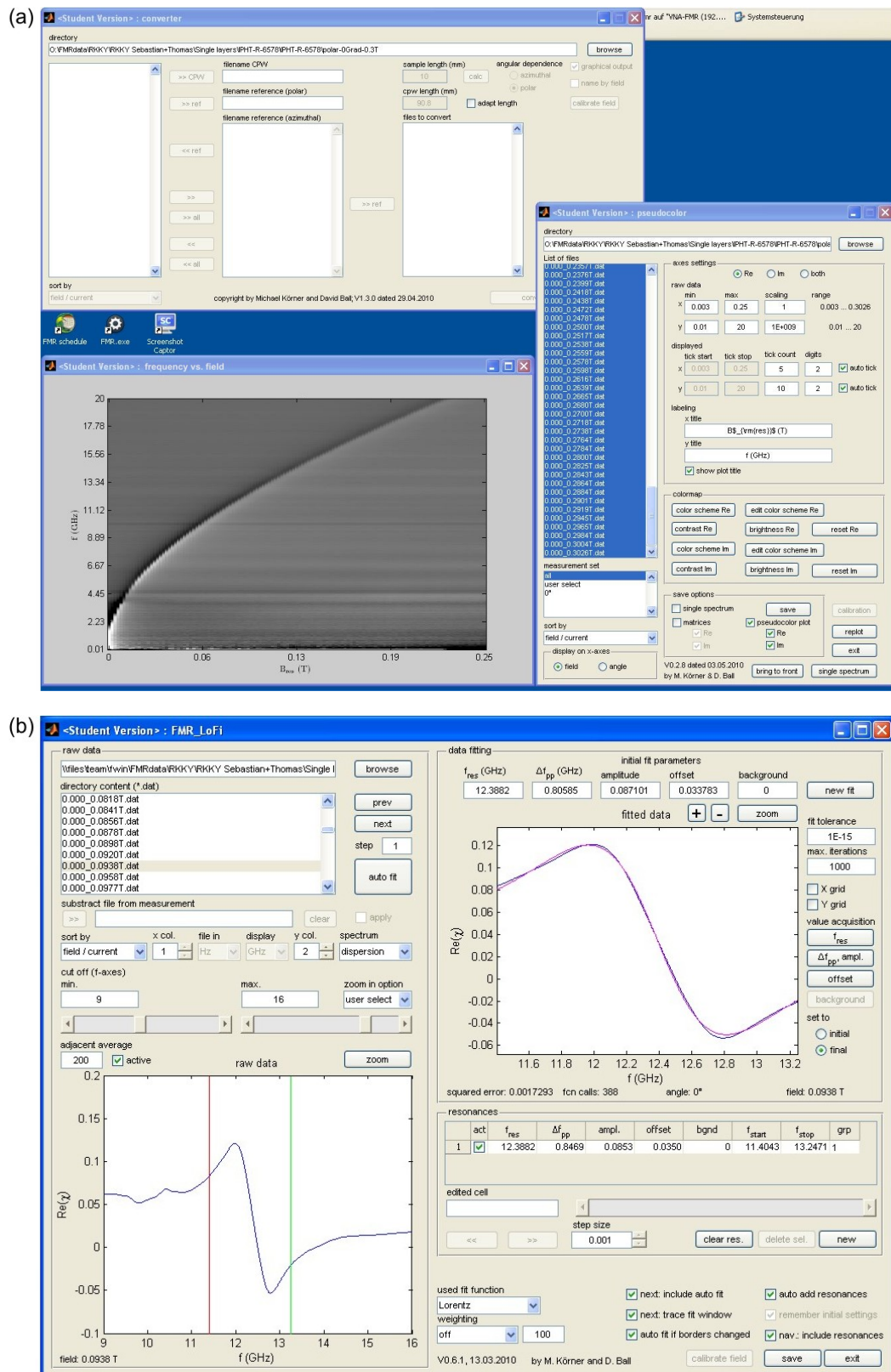


**Fig. 5.5:** Screenshots of the VNA-FMR data evaluation software written with Matlab for (a) the conversion from S-parameters into dynamic magnetic susceptibility and (b) fitting the data with Lorentzians.

reflections and the proximity of the reference field to the fields applied during the measurements. Fitting  $U(f)$  to a modified susceptibility response function, the resonance frequency  $f$  and the frequency linewidth  $\Delta f$  are obtained.

Kuanr *et al.* [101] only used the magnitude of the measured transmission parameter  $S_{12}$  to derive  $\Delta f$ . However, it is pointed out that the linewidth of the peaks seen in  $S_{12}$  is not necessarily directly related to the linewidth obtained from the permeability as the generation of spin waves with  $k \neq 0$  can substantially influence the absorption of energy [102].

### 5.3.2 Methods only using $S_{11}$

Another frequently used approach is based on measuring the single reflection parameter  $S_{11}$  in a one-port geometry [91, 103–107]. Among the advantages of a one-port setup in comparison to a two-port geometry are a less time-consuming calibration, faster measurements, and a higher SNR in certain cases. On the down side, the calibration is less efficient and the data evaluation is more complex than in the case of using transmission parameters only. Most implementations of a one-port geometry employ a short-circuited CPW, but it is also possible to use an open-circuited setup. A detailed treatment of the latter can be found in [84].

## 5.4 Accuracy of the Different Evaluation Methods

A detailed comparison of the accuracy of the evaluation methods presented in this chapter can be found in Ref. [84]. Assuming that the full two-port data evaluation method offers the highest accuracy as it is the only one taking into account both reflection and transmission, it was taken as reference. The ferromagnetic resonance frequencies  $f_{\text{res}}$  determined by the different methods were found to differ by less than 1 %. However, in the case of the frequency linewidths  $\Delta f$ , the relative error with respect to the full two-port data evaluation amounts up to 10 %. In general, the relative errors decrease with increasing applied magnetic field  $H_{\text{ext}}$ , and the method only using the magnitude of  $S_{21}$  showed the largest relative error.

## 6 Magnetostatics and Dynamics of Ion Irradiated Py/Ta Multilayers

As mentioned in the introduction, ion irradiation of ferromagnetic films, multilayers, and nanostructures is a popular and relatively simple method to tailor their magnetic properties and structural composition in a post-deposition process. However, some properties like the effective magnetic volume after irradiation of a sample might be unknown or inaccessible by conventional techniques such as cross-section transmission electron microscopy (TEM) due to vanishing chemical contrast.

Another problem arises for elements which tend to intermix. Transition metals like Ta are widely used as seed and cap layers in spintronic devices like GMR sensors or MTJs because Ta is chemically stable. Moreover, it helps to tune the precessional motion of the magnetization after a switching event [108]. In this context the structural and magnetic properties of various kinds of Py/Ta structures (Py = Permalloy:  $\text{Ni}_{80}\text{Fe}_{20}$ ) have been already investigated [109–115]. For example it was shown experimentally [112, 114] and verified theoretically [112, 113, 116] that Ta leads to magnetically dead layers of 0.6–1.2 nm thickness just by intermixing due to self-diffusion. Already 12 % of Ta intermixing are sufficient to suppress the entire magnetic moment of the Ni atoms in Py [112]. These dead layers make it difficult to determine the correct magnetic volume, which is needed to obtain the saturation magnetization from the magnetic moment measured, e.g., by SQUID magnetometry. This is especially true for multilayer samples, which typically have a large number of interfaces and therefore a strongly reduced effective magnetic volume. Therefore, the influence of ion irradiation on the saturation magnetization could only be investigated qualitatively up to now [117, 118].

In order to study the effects of interfacial mixing and to find a way to qualitatively determine the saturation magnetization of ion irradiated samples, a series of Py/Ta thin films and multilayers has been investigated. Since Py does not exhibit a perpendicular anisotropy, polar MOKE and VNA-FMR measurements can be used to directly measure the saturation magnetization, circumventing the problem of the unknown effective magnetic volume, which would arise using conventional, magnetic-moment-based magnetometry. The saturation magnetization is not evaluated from calibrated MOKE measurements nor from its proportionality to the FMR amplitude, as these methods are cumbersome and error-prone. Instead,  $\mu_0 M_S$  is directly determined from the magnetic anisotropy energy. In addition, the magnetic damping parameter  $\alpha_{\text{eff}}$  has been evaluated and the ion fluence for which magnetism vanishes has been determined.

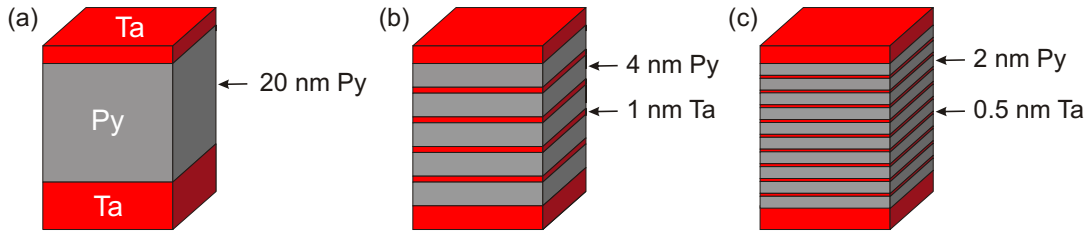


**Fig. 6.1:** The Py/Ta stacks: (a)  $1\times\text{Py}$ , (b)  $5\times\text{Py}$ , and (c)  $10\times\text{Py}$ .

## 6.1 Sample Preparation and Composition

The Py/Ta thin films and multilayers used in this study were deposited on a Si/SiO<sub>2</sub> substrate using dc magnetron sputtering in a multi-source high vacuum system (base pressure below  $2\times 10^{-7}$  mbar) at an Ar pressure of  $7.5\times 10^{-4}$  mbar. Three sample sets were investigated, which are referred to as  $1\times\text{Py}$ ,  $5\times\text{Py}$ , and  $10\times\text{Py}$ . The nominal overall thickness of Py and Ta in all samples was 20 nm and 38 nm, respectively, which was then divided into multilayers according to Fig. 6.1. The  $1\times\text{Py}$  series consists of a 35 nm thick Ta seed layer, followed by a single Py layer of 20 nm thickness and a 3 nm thick protective Ta cap layer. For the  $5\times\text{Py}$  samples the Py is divided into five layers of 4 nm Py, each separated by 1 nm thick Ta film. The  $10\times\text{Py}$  contains ten Py layers of 2 nm thickness, which are separated by 0.5 nm thick Ta layers. For both multilayer systems, the seed layer thickness was chosen such that the total thickness of Ta including the 3 nm protective cap layer and the spacer layers also corresponds to 38 nm. After sputtering all but the reference samples were irradiated at room temperature with Ne ions of 40 keV and fluences in the range of  $5\times 10^{13}$  to  $5\times 10^{16}$  Ne/cm<sup>2</sup>. According to SRIM simulations [119] the mean projected range of the Ne ions in the  $1\times\text{Py}$ ,  $5\times\text{Py}$ , and  $10\times\text{Py}$  systems corresponds to 33.8 nm, 34.3 nm, and 34.4 nm, respectively (straggle: 23.0 nm), i.e., the Ne ions penetrate the entire stacks and lead to an intermixing of all Py/Ta interfaces.

## 6.2 Structural Investigation and Simulation of the Interfacial Mixing

The structural characterization of the as-deposited and selected ion irradiated samples has been performed by cross-sectional transmission electron microscopy (TEM) using a Philips CM300 microscope. In Fig. 6.2a a bright-field image of the unirradiated  $1\times\text{Py}$  sample is shown. The Si/SiO<sub>2</sub> substrate, the Ta seed layer, the Py layer, and the Ta cap layer can be clearly distinguished due to the mass contrast and the well-defined interfaces. Even in the case of the unirradiated  $10\times\text{Py}$  sample, displayed in Fig. 6.2b, with its subnanometer thick Ta spacer layers this is still possible. Moreover, it is found that the actual thickness of the Py and Ta layers in all investigated samples (also the  $5\times\text{Py}$ , which is not shown) differs from its nominal value and is generally smaller than this. The reason for this deviation might be a not perfectly calibrated sputtering system or samples taken from the edge of the

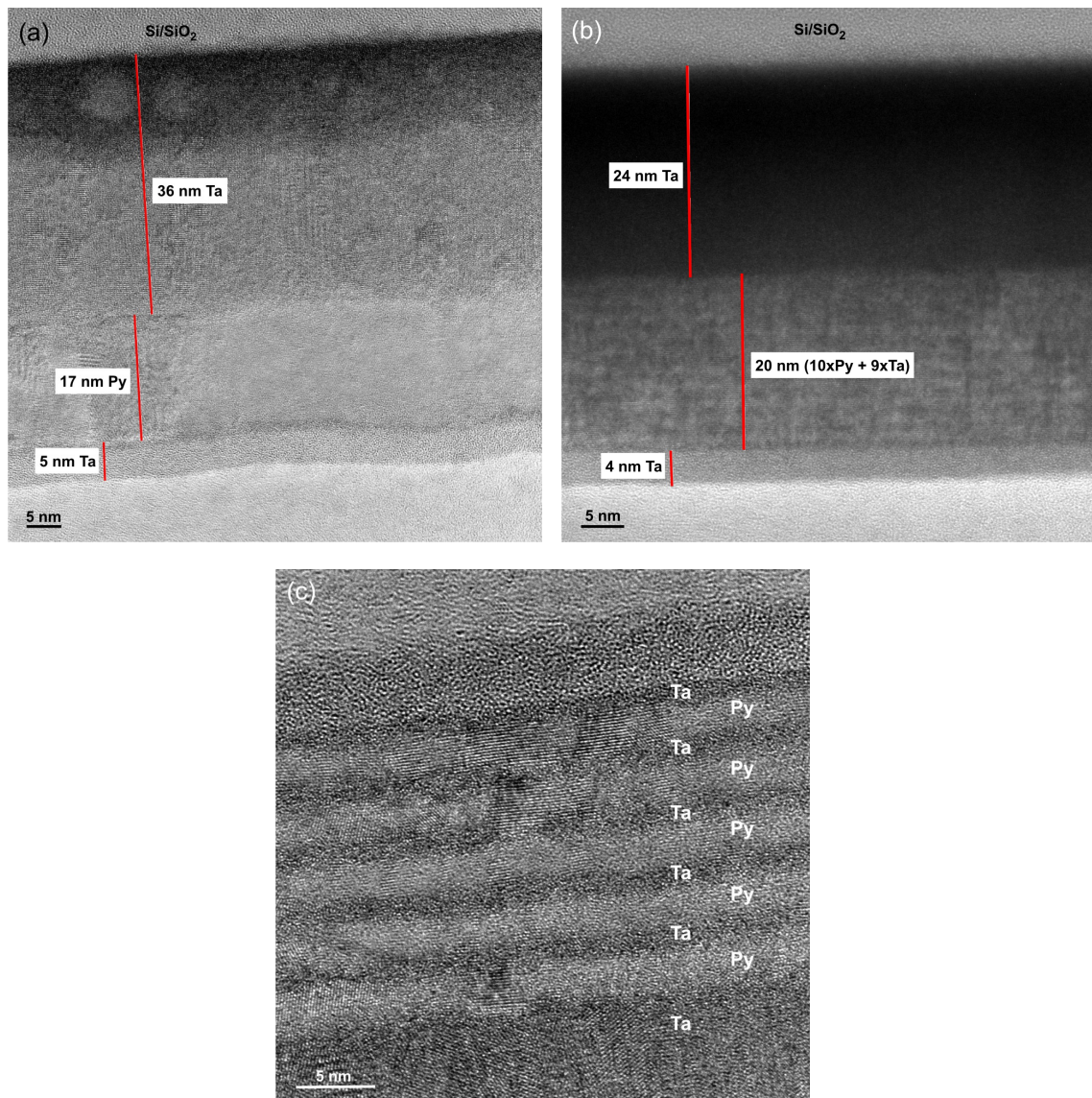


**Fig. 6.2:** Cross-sectional TEM images of the unirradiated  $1\times\text{Py}$  sample (a) and  $10\times\text{Py}$  sample (b) as well as (c) the  $5\times\text{Py}$  sample irradiated with a fluence of  $3\times 10^{14}$  Ne ions/cm<sup>2</sup>. The Py/Ta interfaces can be clearly distinguished. However, it can be seen, that the actual thickness of the Py and Ta layers in the samples is smaller than its nominal value.

sputtered Si wafer. The overall Py thickness in the unirradiated samples, which is later needed for calculating the saturation magnetization  $M_S$ , as determined from the TEM images amounts to 17 nm, 16.0 nm, and 16.5 nm for the  $1\times\text{Py}$ ,  $5\times\text{Py}$ , and  $10\times\text{Py}$ , respectively.

As mentioned in the introduction, Ta tends to intermix with Py thus reducing the magnetic moment at the interface. Since intermixing occurs only on a length scale of roughly 1 nm, it is in principle still possible to determine the active magnetic volume of a multilayer by subtracting the estimated amount of dead layers. However,

errors could be significant. It is known, that whenever ion irradiation is used the intermixing effect is strongly enhanced. This is shown in Fig. 6.2c using the example of the  $5\times\text{Py}$  sample irradiated with a fluence of  $3\times 10^{14}$  Ne ions/cm<sup>2</sup>. The individual Py and Ta layers can still be distinguished, but their interfaces have become blurred. The reason for this is an increase of the Ta concentration in the Py layers close to the interfaces, which in turn increases the thickness of the magnetically dead layers.

In addition to the TEM investigations, the result of irradiating the Py/Ta samples with Ne ions has been simulated using the TRIDYN code [120]. In Fig. 6.3, the depth profile of the relative concentration of the individual elements in the Py/Ta samples before and after irradiation with selected fluences is depicted. For the simulations, the Py has been replaced by its constituents Ni and Fe and only Si was used as substrate due the limited number of elements available in the employed TRIDYN code.

Starting from sharp interfaces at which the intermixing begins, the Ta concentration in the Py layers increases towards their center. The thinner the Py layers and the higher the number of interfaces, respectively, the stronger this effect. It is clear that no valid assumption for the active magnetic volume can be made in such cases. For regions of the Py layers in which the Ta concentration exceeds 10 % [121], an amorphization of the crystalline alloy takes place [122–124]. This case is shown in the lower panels of each sample system in Fig. 6.3. The corresponding fluence at which amorphization occurs depends on the number of interfaces and amounts to  $5\times 10^{16}$  Ne/cm<sup>2</sup> for the  $1\times\text{Py}$  samples,  $0.5\times 10^{16}$  Ne/cm<sup>2</sup> for the  $5\times\text{Py}$  samples, and  $0.1\times 10^{16}$  Ne/cm<sup>2</sup> for the  $10\times\text{Py}$  samples, respectively. The three sample systems then only differ with respect to the gradient of the Ta concentration at the interfaces to the compound of Ni, Fe, and Ta, which is largest for the  $10\times\text{Py}$ . In addition to the interface mixing, sputtering effects occur reducing the overall thickness of the Py/Ta stacks. Whereas for the multilayers samples the thickness of the Ta cap layer only reduces by about 1 nm, it is completely sputtered away in the case of the  $1\times\text{Py}$  due to the high ion fluence. Furthermore, even 4 nm of the Py layer itself have vanished.

### 6.3 Static Magnetic Characterization

The static magnetic properties of the samples have been investigated by means of longitudinal magneto-optical Kerr effect (MOKE). The easy axis magnetization reversal curves of selected  $1\times\text{Py}$  samples, depicted in Fig. 6.4a, show the typical behavior of a soft-magnetic material as it is expected for Py. It can be seen that with increasing ion fluence the magnitude of the Kerr rotation and thus the magnetic moment of the samples is subsequently reduced. The same is true for the uniaxial anisotropy field of the samples, which can be determined from the corresponding hard axis hysteresis loops shown in Fig. 6.4b. However, the coercivity of the samples, which is very small, remains virtually unchanged. The magnetic anisotropy was further investigated by measurements of the full angular dependence of the magnetization reversal behavior. The remanence of the hysteresis loops of the  $1\times\text{Py}$  samples is shown in Fig. 6.4c. For all samples a clear two-fold symmetry, which reflects a



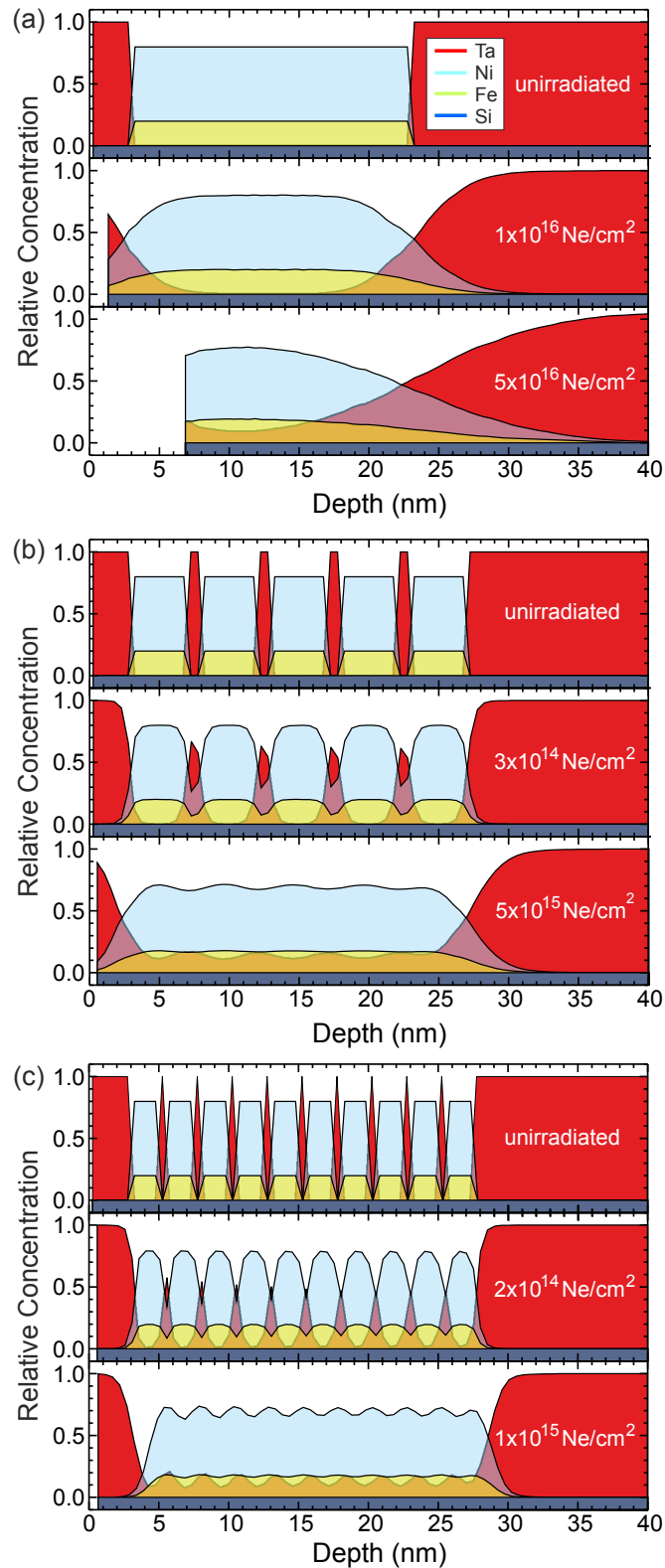


**Fig. 6.3:** TRIDYN [120] simulations of the depth profiles of the relative atomic concentrations in the (a) 1xPy, (b) 5xPy, and (c) 10xPy samples before and after irradiation with different fluences.

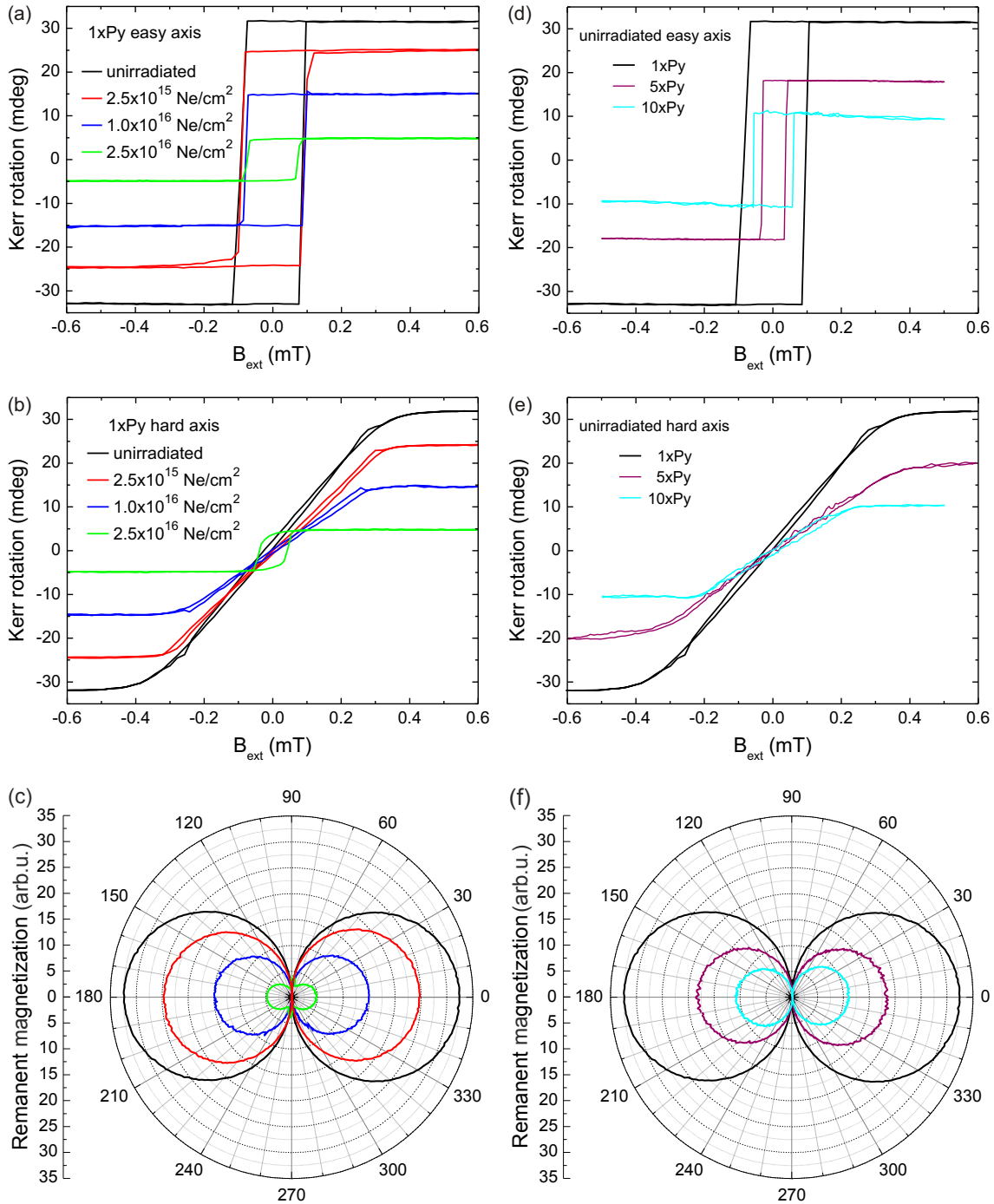


**Fig. 6.4:** Easy axis and hard axis hysteresis loops as well as full angular dependence of the remanent magnetization of selected 1xPy samples (a,b,c) and the unirradiated 1xPy, 5xPy, and 10xPy samples (d,e,f).

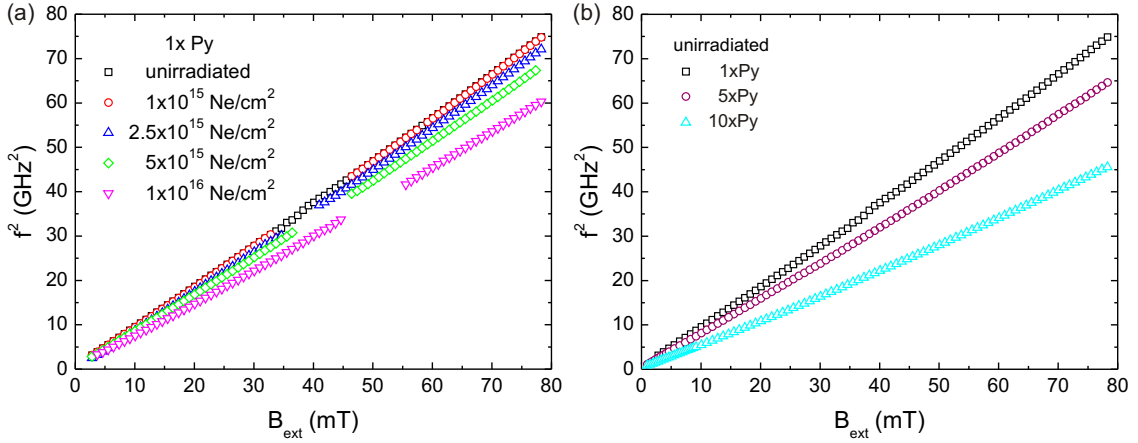


**Fig. 6.5:** Squared frequency dependence of the resonance field of (a) selected 1×Py samples and (b) the unirradiated Py/Ta samples measured along the easy axis.

uniaxial anisotropy and remains unaffected by ion irradiation, is observed.

The influence of the number of interfaces on the static magnetic properties of the samples is quite similar to the one of ion irradiation. From the easy axis and hard axis hysteresis loops of the unirradiated 1×Py, 5×Py, and 10×Py, depicted in Fig. 6.4d and Fig. 6.4e, respectively, it can be seen that with increasing number of interfaces both the magnetic moment and the uniaxial anisotropy field decrease. Moreover, the angular dependence of the remanent magnetization, plotted in Fig. 6.4f, also shows a two-fold symmetry. Only the decrease of coercivity is in contrast to the effects of ion irradiation. However, its values are almost zero in any case.

## 6.4 Dynamic Magnetic Characterization

The magnetization dynamics of the samples has been investigated by VNA-FMR as well. In Fig. 6.5a, the square of the resonance frequency  $f_{\text{res}}^2$  of the 1×Py samples as a function of the magnetic field  $B_{\text{ext}}$  applied along the easy axis is plotted. Whereas there is virtually no difference between the unirradiated sample and the samples irradiated with fluences up to  $1 \times 10^{15}$  Ne/cm<sup>2</sup>, a significant decrease of the resonance frequency  $f$  can be observed for fluences of  $2.5 \times 10^{15}$  Ne/cm<sup>2</sup> and higher. The discontinuities are due to a disturbing resonance coming from the experimental setup. Fig. 6.5b depicts the case for the three unirradiated samples. Here, the resonance frequency strongly decreases with an increasing number of Py/Ta interfaces. Both effects were expected due to the creation of dead layers leading to a reduction of the effective ferromagnetic film thickness close to the interfaces [21, 112–114, 116].

The frequency–field dependences of Fig. 6.5 are given by the resonance equation

$$f = \frac{|\gamma|}{2\pi} \sqrt{\mu_0 H \left( \mu_0 H + \mu_0 M_{\text{eff}} + \frac{K_{2\parallel}}{M_S} \right)}. \quad (6.1)$$

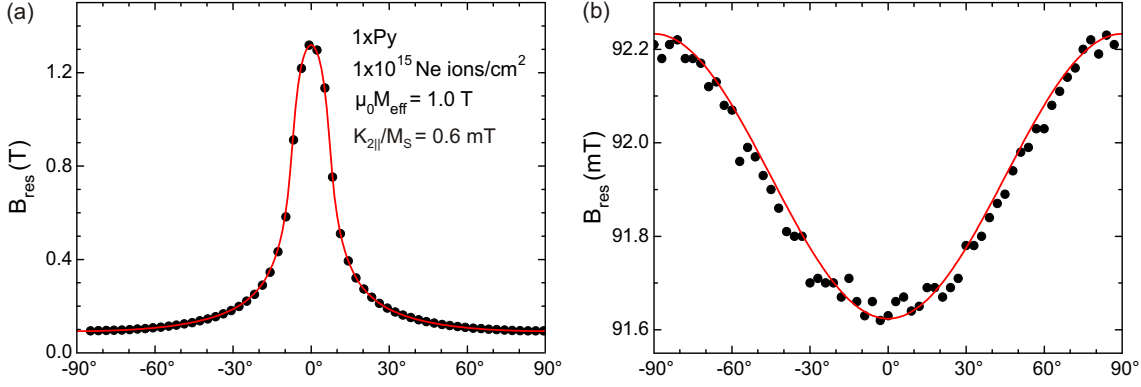


**Fig. 6.6:** (a) Polar and (b) azimuthal angular dependence of the resonance field of the  $1 \times \text{Py}$  sample irradiated with  $1 \times 10^{15} \text{ ions/cm}^2$  measured at X-band. The red solid lines are fits.

In general, only the *effective* magnetization

$$\mu_0 M_{\text{eff}} = \mu_0 M_S - \frac{2K_{2\perp}}{M_S}, \quad (6.2)$$

but not  $\mu_0 M_S$  itself, can be determined from MOKE and FMR measurements. However, if the samples do not exhibit a perpendicular anisotropy, i.e.,  $2K_{2\perp}/M_S \approx 0$ ,  $\mu_0 M_{\text{eff}}$  can be replaced with  $\mu_0 M_S$  and is entirely determined by the shape anisotropy field. In the present case, this would allow to determine the saturation magnetization simply from the slope of the resonance frequency without having to know the magnetically active volume. In order to verify that there is really no perpendicular anisotropy contribution, angle-dependent X-band FMR measurements have been performed. The polar and azimuthal angular dependence of the resonance field for the  $1 \times \text{Py}$  sample irradiated with a fluence of  $1 \times 10^{15} \text{ Ne/cm}^2$  are shown in Fig. 6.6a and Fig. 6.6b, respectively. The solid lines are fits using the resonance equation as described elsewhere [125].  $\mu_0 M_{\text{eff}}$  amounts to 1.016 T. A uniaxial in-plane anisotropy field of  $K_{2\parallel}/M_S = 0.65 \text{ mT}$ , but no fourfold or perpendicular anisotropy contribution is found. In the case of the multilayers, only a single resonance line is observed, which means that these behave like a strongly coupled, effective single film.

### Determination of the Saturation Magnetization

Using Eq. (6.1), the uniaxial in-plane anisotropy field  $K_{2\parallel}/M_S$  and the saturation magnetization  $\mu_0 M_S$  have been fitted from the VNA-FMR data. For this analysis, a  $g$ -factor for Py of  $g = 2.10$  (Ref. [126]) was assumed for all samples as exact values for the irradiated samples are unknown. However, increasing  $g$  by 0.01 would decrease  $\mu_0 M_S$  by 1 % only. The results are given in Tab. 6.1.

Complementary,  $\mu_0 M_S$  is also determined from MOKE measurements. In Fig. 6.7a magnetization reversal curves of selected  $1 \times \text{Py}$  samples measured in polar geometry are shown. Since the loops do not show any hysteresis, the samples do not possess

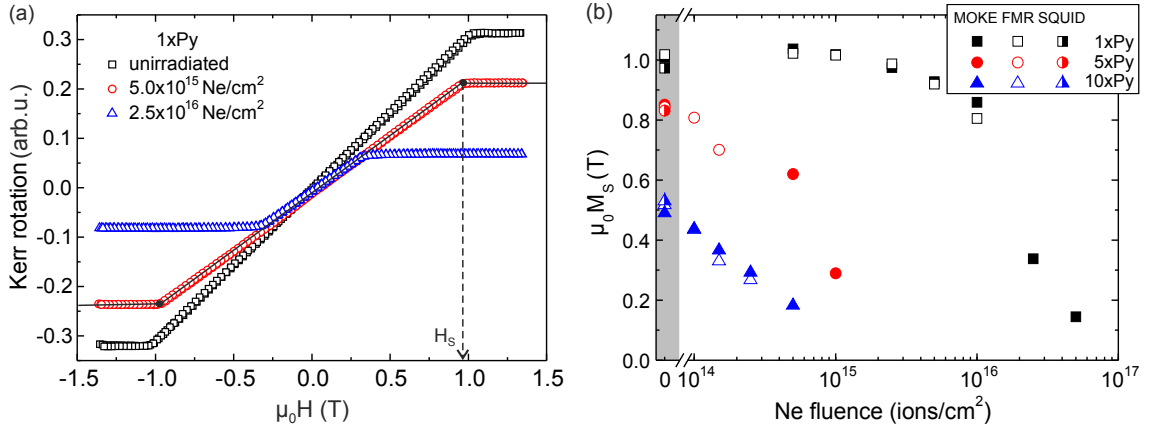


**Fig. 6.7:** (a) Magnetization reversal curves of selected 1×Py samples measured in polar MOKE geometry. (b) Saturation magnetization  $\mu_0 M_S$  determined by FMR, polar MOKE, and SQUID magnetometry. Data of the unirradiated samples are shown in the gray-shaded area on the left-hand side. Error bars are 10 % for the 10×Py samples, otherwise within symbol size.

a perpendicular anisotropy, which is in line with the X-band FMR results. In this case, the saturation magnetization  $\mu_0 M_S$  can be determined from the intersection of the steep reversal region and the horizontal saturation branch. The values of  $\mu_0 M_S$  are shown in Fig. 6.7b.

The usual approach to determine the saturation magnetization of ferromagnets is to use SQUID magnetometry. However, as mentioned in the introduction, this magnetic-moment-based technique requires the knowledge of the effective magnetic volume, which is practically impossible to determine in the case of ion irradiated multilayers containing Ta. In the present case, SQUID magnetometry is therefore only employed to determine  $\mu_0 M_S$  of the unirradiated 1×Py, 5×Py, and 10×Py

**Tab. 6.1:** Uniaxial in-plane anisotropy field  $K_{2\parallel}/M_S$  and saturation magnetization  $\mu_0 M_S$  (both in mT) determined from VNA-FMR.

Ion fluence (Ne/cm <sup>2</sup> )	1×Py		5×Py		10×Py	
	$K_{2\parallel}/M_S$	$\mu_0 M_S$	$K_{2\parallel}/M_S$	$\mu_0 M_S$	$K_{2\parallel}/M_S$	$\mu_0 M_S$
unirradiated	0.70	1018	0.01	841	0.31	517
$1.0 \times 10^{14}$	–	–	0.31	808	0.19	435
$1.5 \times 10^{14}$	–	–	0.00	701	0.36	330
$2.5 \times 10^{14}$	–	–	–	–	0.21	267
$5.0 \times 10^{14}$	0.71	1022	–	–	–	–
$1.0 \times 10^{15}$	0.65	1016	–	–	–	–
$2.5 \times 10^{15}$	0.64	987	–	–	–	–
$5.0 \times 10^{15}$	0.67	920	–	–	–	–
$1.0 \times 10^{16}$	0.74	805	–	–	–	–

samples, since their overall Py thickness has been determined by TEM.

In Fig. 6.7b, the comparison of MOKE, FMR, and SQUID data of the unirradiated samples (datapoints in gray area) shows consistent results. For the irradiated samples no SQUID data can be achieved, as explained earlier. However, MOKE and FMR represent suitable alternatives since they allow to determine the saturation magnetization  $\mu_0 M_S$  without the knowledge of any film thickness. The good agreement with the SQUID data of the non-irradiated samples supports this. With increasing ion fluence,  $\mu_0 M_S$  subsequently reduces, which can be explained by the increased interfacial mixing due to the ion irradiation. However, the way the saturation magnetization decreases strongly depends on the number of interfaces. In the case of the 10×Py samples, a linear decrease of  $\mu_0 M_S$  sets in already at small ion fluences. However, for the 1×Py and 5×Py samples, the saturation magnetization remains constant up to a certain ion fluence, but then starts to decrease even faster. For instance, after irradiation with a fluence of  $1 \times 10^{15}$  Ne/cm<sup>2</sup>, the 1×Py sample still possesses 100 %  $\mu_0 M_S$ , whereas the 10×Py is already magnetically dead. The extrapolated ion fluences for which  $\mu_0 M_S = 0$  are  $1.5 \times 10^{15}$  Ne/cm<sup>2</sup>,  $2.5 \times 10^{15}$  Ne/cm<sup>2</sup>, and  $6 \times 10^{16}$  Ne/cm<sup>2</sup> for the 1×Py, 5×Py, and 10×Py samples, respectively. These values are close to the ones determined from the TRIDYN simulations.

## 6.5 Linewidth and Damping

As the number of interfaces or the amount of irradiation modifies the magnetic properties, a similar impact is expected on the magnetic relaxation [14, 108]. The damping parameters can be directly calculated from the resonance linewidth.

In Fig. 6.8a, the frequency-swept linewidth  $\Delta f$ , as directly determined from VNA-FMR, is shown. It can be seen that for all samples the linewidth first decreases and reaches a minimum before it levels off again with increasing resonance frequency.  $\Delta f$  is of the order of 240 – 400 MHz and increases with both increasing ion fluence as well as with increasing number of interfaces. The minimum of the linewidth shifts to higher frequencies the larger the ion fluence or number of Py/Ta interfaces.

Since the amount of information of the measured, frequency-swept linewidth  $\Delta f$  is limited, it is converted into the field-swept linewidth  $\Delta B$  by [48]:

$$\Delta B = \frac{2\pi\Delta f}{|\gamma| \sqrt{1 + \left(\frac{|\gamma|\mu_0 M_S}{4\pi f}\right)^2}}. \quad (6.3)$$

Fig. 6.8b shows its frequency dependence for the different samples. The linear slope indicates that there is no magnon-magnon scattering [23]. The damping constant  $\alpha$  and inhomogeneous broadening  $\Delta B_0$ , are obtained from fitting

$$\Delta B = \Delta B_0 + \frac{2}{\sqrt{3}} \frac{\alpha}{|\gamma|} 2\pi f \quad (6.4)$$

to the data and are summarized in Tab. 6.2. For 1×Py,  $\alpha$  slightly increases with

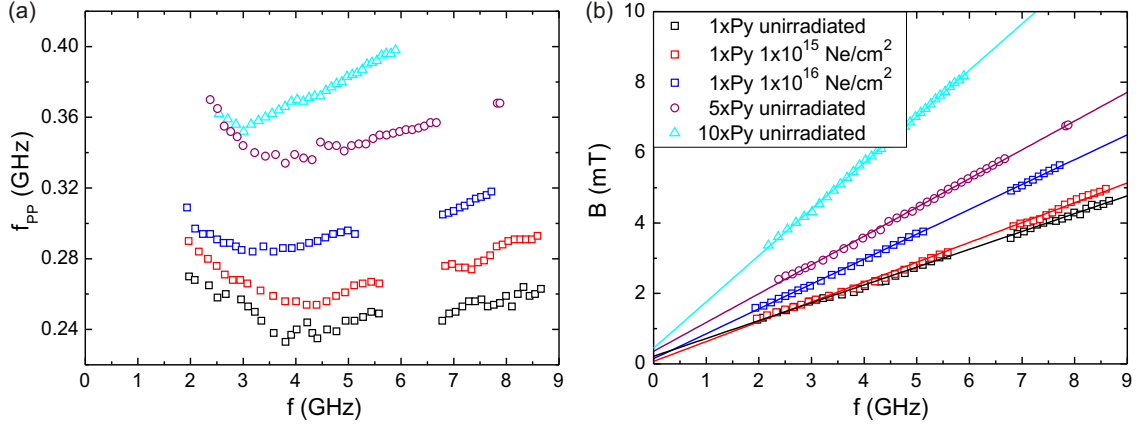


**Fig. 6.8:** Frequency dependence of (a) the frequency linewidth  $\Delta f_{PP}$  and (b) the field linewidth  $\Delta B$ . The solid lines are fits according to Eq. (6.4).

ion fluence from a typical Py value [101] of  $\alpha=0.013$  (unirradiated) to 0.018 at  $1 \times 10^{16}$  Ne/cm<sup>2</sup> due to Py–Ta intermixing caused by the irradiation. For higher numbers of Py/Ta interfaces (unirradiated)  $\alpha$  is much higher: 0.021 (0.034) for 5×Py (10×Py). This is explained again by the even higher fraction of intermixed Py–Ta compared to the pure Py fraction as the Py layers get thinner in the 5×Py and 10×Py samples. The  $\Delta B_0$  contribution is quite small ranging from 0.07 mT for 1×Py irradiated with  $1 \times 10^{15}$  Ne/cm<sup>2</sup> to 0.45 mT for the unirradiated 10×Py sample. It slightly decreases with increasing ion fluence, but increases with increasing number of interfaces. The latter is likely caused by mosaicity, i.e., an angular spread in the sample parameters due to a higher roughness caused by strain in the increasing number of interfaces.

## 6.6 Conclusion

The magnetostatics and dynamics of ion irradiated, soft magnetic Py/Ta single and multilayer films have been studied with the main objective of finding a way to determine their saturation magnetization. Both polar MOKE and FMR measurements

**Tab. 6.2:** Effective damping parameter  $\alpha$  and inhomogeneous linewidth broadening  $\Delta B_0$  of selected Py/Ta samples.

Sample	$\alpha$	$\Delta B_0$ (mT)
1×Py unirradiated	0.013	0.22
1×Py $1.0 \times 10^{15}$	0.014	0.07
1×Py $1.0 \times 10^{16}$	0.018	0.15
5×Py unirradiated	0.021	0.36
10×Py unirradiated	0.034	0.45

have proven to be suitable methods to determine  $\mu_0 M_S$ , circumventing the problem of the unknown effective magnetic volume that causes conventional techniques like SQUID or VSM to fail. Provided there is no perpendicular anisotropy contribution in the samples, the saturation magnetization can be determined even in the case of strong interfacial mixing due to an inherently high number of Py/Ta interfaces and/or ion irradiation with high fluences.

With both increasing ion fluence and number of Py/Ta interfaces, a decrease of saturation magnetization and an increase of damping has been observed. In the case of the  $10\times$ Py samples, a linear decrease of  $\mu_0 M_S$  sets in already at small ion fluences. However, for the  $1\times$ Py and  $5\times$ Py samples, the saturation magnetization remains constant up to a certain ion fluence, but then starts to rapidly decrease. Ne ion irradiation causes a mixing and broadening of the interfaces. Thus, the Py/Ta stacks undergo a transition from being polycrystalline to amorphous at a critical fluence depending on the number of interfaces. The saturation magnetization is found to vanish at a Ta concentration of about 10 – 15 at.% in the Py layers. The samples possess a small uniaxial anisotropy, which remains virtually unaffected by the ion fluence, but slightly reduces with an increasing number of interfaces.

In addition to magnetostatics, the dynamic properties of the samples have also been investigated. The Gilbert damping parameter  $\alpha$  increases with both increasing number of Py/Ta interfaces and higher ion fluences, with the former having a stronger influence. The inhomogeneous linewidth broadening  $\Delta B_0$  increases as well with increasing number of Py/Ta interfaces, but slightly decreases for higher ion fluences.

Thus, ion irradiation offers the possibility to selectively modify saturation magnetization and damping in a post-deposition process.



# 7 Summary and Outlook

The main objective of this Ph.D. thesis was to construct a VNA-FMR spectrometer capable of performing both azimuthal and polar angle-dependent measurements using a magnet strong enough to saturate samples containing iron. Starting from scratch, this comprised numerous steps such as developing a suitable CPW design, and writing the control, evaluation, and fitting software before it has been successfully accomplished.

In a first step, a test setup (VNA-FMR Setup 1) has been constructed, which employed a pair of Helmholtz coils to generate magnetic fields of up to  $B = 0.08$  T and a straight CPW. With this setup, the scientific results presented herein have been obtained.

In a second step, the final setup (VNA-FMR Setup 2) has been built, which is much more sophisticated and is vastly improved in the following points: (i) The maximum available magnetic field, generated by an electromagnet, amounts to  $B = 2.2$  T and thus almost corresponds to 30 times the value generated by the Helmholtz coils. (ii) The employed CPW is designed and optimized for frequencies up to 50 GHz. (iii) Full azimuthal and polar angle-dependent measurements allow for a much more precise investigation of magnetic anisotropies. (iv) Measurements run fully automated and can be remotely controlled.

From the two possible modes of operation, the frequency-swept one has been used throughout this thesis and the measurements have been evaluated using the full two-port data evaluation method, which offers utmost accuracy.

The first samples extensively studied with VNA-FMR Setup 1 are soft magnetic Py/Ta single and multilayer films. The implications of ion irradiation on their magnetostatic and dynamic properties have been investigated with the main objective of finding a way to determine their saturation magnetization. Both polar MOKE and VNA-FMR measurements have proven to be suitable methods to determine  $\mu_0 M_S$ , circumventing the problem of the unknown effective magnetic volume that causes conventional techniques like SQUID or VSM to fail. Provided there is no perpendicular anisotropy contribution in the samples, the saturation magnetization can be determined even in the case of strong interfacial mixing due to an inherently high number of Py/Ta interfaces and/or ion irradiation with high fluences.

With both increasing ion fluence and number of Py/Ta interfaces, a decrease of saturation magnetization has been observed. In the case of the  $10 \times$ Py samples, a linear decrease of  $\mu_0 M_S$  already sets in at small ion fluences. However, for the  $1 \times$ Py and  $5 \times$ Py samples, the saturation magnetization remains constant up to a certain ion fluence, but then starts to rapidly decrease. Ne ion irradiation causes a mixing and broadening of the interfaces. Thus, the Py/Ta stacks undergo a transition from being polycrystalline to amorphous at a critical fluence depending on the number of

interfaces. The saturation magnetization is found to vanish at a Ta concentration of about 10–15 at.% in the Py layers. The samples possess a small uniaxial anisotropy, which remains virtually unaffected by the ion fluence, but slightly reduces with an increasing number of Py/Ta interfaces.

In addition to magnetostatics, the dynamic properties of the samples have been investigated as well. The Gilbert damping parameter  $\alpha$  increases with both increasing number of Py/Ta interfaces and higher ion fluences, with the former having a stronger influence. The inhomogeneous linewidth broadening  $\Delta B_0$  increases as well with increasing number of Py/Ta interfaces, but slightly decreases for higher ion fluences.

In the near future, VNA-FMR Setup 2 will experience several upgrades. First, an optimized version of the employed CPW, featuring a narrower center conductor for higher excitation field amplitudes, a smaller sample load section, and an improved launch taper geometry is under development. Second, the field-swept mode of operation is about to be implemented. Third, an all-in-one software solution combining the conversion from S-parameters to dynamic magnetic susceptibility, the extraction of resonance frequency and linewidth as well as fitting the data from angle-dependent measurements is planned.

Future scientific activities will focus on the investigation of magnetic damping in various sample systems such as Heusler alloys, with focus on two-magnon scattering. Apart from studying only extended thin films, it is a mid-term goal to investigate arrays of micron-sized elements like dots and squares, which are directly patterned on the CPW. The necessary tools, namely electron beam lithography and focused ion beam systems, are available for some time now and can be used to produce CPWs by oneself.

# Bibliography

- [1] J. Hirschenberger, “*Geschichte der Philosophie*,” Vol. 1, Verlag Herder, Freiburg im Breisgau, Germany (1980).
- [2] J. Needham, “*Science in Civilisation in China*”, Vol. 4, Cambridge University Press, UK (1962).
- [3] M. N. Baibich, J. M. Broto, A. Fert, F. N. Van Dau, F. Petroff, P. Etienne, G. Creuzet, A. Friederich and J. Chazelas, “*Giant Magnetoresistance of (001)Fe/(001)Cr Magnetic Superlattices*”, Phys. Rev. Lett. **61**, 2472 (1988).
- [4] G. Binasch, P. Grünberg, F. Saurenbach and W. Zinn, “*Enhanced magnetoresistance in layered magnetic structures with antiferromagnetic interlayer exchange*”, Phys. Rev. B **39**, 4828 (1989).
- [5] M. Jullière, “*Tunneling between ferromagnetic films*”, Phys. Lett. A **54**, 225 (1975).
- [6] J. S. Moodera, L. R. Kinder, T. M. Wong and R. Meservey, “*Large Magnetoresistance at Room Temperature in Ferromagnetic Thin Film Tunnel Junctions*”, Phys. Rev. Lett. **74**, 3273 (1995).
- [7] T. Miyazaki and N. Tezuka, “*Giant magnetic tunneling effect in Fe/Al<sub>2</sub>O<sub>3</sub>/Fe junction*”, J. Magn. Magn. Mater. **139**, L231 (1995).
- [8] J. M. Daughton, “*Magnetic tunneling applied to memory*”, J. Appl. Phys. **81**, 3758 (1997).
- [9] B. D. Terris, “*Fabrication challenges for patterned recording media*”, J. Magn. Magn. Mater. **321**, 512 (2009).
- [10] J. Fassbender, D. Ravelosona and Y. Samson, “*Tailoring magnetism by light-ion irradiation*”, J. Phys. D: Appl. Phys. **37**, R179 (2004).
- [11] C. Chappert, H. Bernas, J. Ferré, V. Kottler, J.-P. Jamet, Y. Chen, E. Cambril, T. Devolder, F. Rousseaux, V. Mathet and H. Launois, “*Planar Patterned Magnetic Media Obtained by Ion Irradiation*”, Science **280**, 1919 (1998).
- [12] M. O. Liedke, B. Liedke, A. Keller, B. Hillebrands, A. Mücklich, S. Facsko and J. Fassbender, “*Induced anisotropies in exchange-coupled systems on rippled substrates*”, Phys. Rev. B **75**, 220407 (2007).

- [13] J. Fassbender, T. Strache, M. O. Liedke, D. Markó, S. Wintz, K. Lenz, A. Keller, S. Facsko, I. Mönch and J. McCord, “*Introducing artificial length scales to tailor magnetic properties*”, *New Journal of Physics* **11**, 125002 (2009).
- [14] G. Woltersdorf, M. Kiessling, G. Meyer, J.-U. Thiele and C. H. Back, “*Damping by Slow Relaxing Rare Earth Impurities in  $Ni_{80}Fe_{20}$* ”, *Phys. Rev. Lett.* **102**, 257602 (2009).
- [15] S. O. Demokritov, C. Bayer, S. Poppe, M. Rickart, J. Fassbender, B. Hillebrands, D. I. Kholin, N. M. Kreines and O. M. Liedke, “*Control of Interlayer Exchange Coupling in Fe/Cr/Fe Trilayers by Ion Beam Irradiation*”, *Phys. Rev. Lett.* **90**, 097201 (2003).
- [16] S. Blomeier, P. Candeloro, B. Hillebrands, B. Reuscher, A. Brodyanski and M. Kopnarski, “*Micromagnetism and magnetization reversal of embedded ferromagnetic elements*”, *Phys. Rev. B* **74**, 184405 (2006).
- [17] J. Fassbender, L. Bischoff, R. Mattheis and P. Fischer, “*Magnetic domains and magnetization reversal of ion-induced magnetically patterned RKKY-coupled  $Ni_{81}Fe_{19}/Ru/Co_{90}Fe_{10}$  films*”, *J. Appl. Phys.* **99**, 08G301 (2006).
- [18] S. Blomeier, B. Hillebrands, B. Reuscher, A. Brodyanski, M. Kopnarski and R. L. Stamps, “*Exchange interaction and magnetic domain formation in periodically inhomogeneous magnetic media*”, *Phys. Rev. B* **77**, 094405 (2008).
- [19] E. Menéndez, M. O. Liedke, J. Fassbender, T. Gemming, A. Weber, L. J. Heyderman, K. V. Rao, S. C. Deevi, S. Suriñach, M. D. Baró, J. Sort and J. Nogués, “*Direct Magnetic Patterning due to the Generation of Ferromagnetism by Selective Ion Irradiation of Paramagnetic FeAl Alloys*”, *Small* **5**, 229 (2009).
- [20] J. McCord, L. Schultz and J. Fassbender, “*Hybrid Soft-Magnetic Lateral Exchange Spring Films Prepared by Ion Irradiation*”, *Adv. Materials* **20**, 2090 (2008).
- [21] J. Fassbender and J. McCord, “*Magnetic patterning by means of ion irradiation and implantation*”, *J. Magn. Magn. Mater.* **320**, 579 (2008).
- [22] U. Ebels, L. D. Buda, K. Ounadjela and P. E. Wigen, in *Spin Dynamics in Confined Magnetic Structures I*, Eds. B. Hillebrands and K. Ounadjela, Chap. Small amplitude dynamics of nonhomogeneous magnetization distributions: The excitation spectrum of stripe domains., p. 167–216, Springer-Verlag Berlin Heidelberg (2002).
- [23] K. Lenz, H. Wende, W. Kuch, K. Baberschke, K. Nagy and A. Jánossy, “*Two-magnon scattering and viscous Gilbert damping in ultrathin ferromagnets*”, *Phys. Rev. B* **73**, 144424 (2006).

- [24] F. Giesen, J. Podbielski, T. Korn, M. Steiner, A. van Staa and D. Grundler, “*Hysteresis and control of ferromagnetic resonances in rings*”, Appl. Phys. Lett. **86**, 112510 (2005).
- [25] F. Giesen, J. Podbielski, T. Korn and D. Grundler, “*Multiple ferromagnetic resonance in mesoscopic permalloy rings*”, J. Appl. Phys. **97**, 10A712 (2005).
- [26] I. Neudecker, G. Woltersdorf, B. Heinrich, T. Okuno, G. Gubbiotti and C. Back, “*Comparison of frequency, field, and time domain ferromagnetic resonance method*”, J. Magn. Magn. Mater. **307**, 148 (2006).
- [27] I. Neudecker, K. Perzlmaier, F. Hoffmann, G. Woltersdorf, M. Buess, D. Weiss and C. H. Back, “*Modal spectrum of permalloy disks excited by in-plane magnetic fields*”, Phys. Rev. B **73**, 134426 (2006).
- [28] I. Neudecker, M. Kläui, K. Perzlmaier, D. Backes, L. J. Heyderman, C. A. F. Vaz, J. A. C. Bland, U. Rüdiger and C. H. Back, “*Spatially Resolved Dynamic Eigenmode Spectrum of Co Rings*”, Phys. Rev. Lett. **96**, 057207 (2006).
- [29] J. Podbielski, F. Giesen and D. Grundler, “*Spin-Wave Interference in Microscopic Rings*”, Phys. Rev. Lett. **96**, 167207 (2006).
- [30] J. Podbielski, D. Heitmann and D. Grundler, “*Microwave-Assisted Switching of Microscopic Rings: Correlation Between Nonlinear Spin Dynamics and Critical Microwave Fields*”, Phys. Rev. Lett. **99**, 207202 (2007).
- [31] F. Giesen, J. Podbielski, B. Botters and D. Grundler, “*Vortex circulation control in large arrays of asymmetric magnetic rings*”, Phys. Rev. B **75**, 184428 (2007).
- [32] F. Giesen, J. Podbielski and D. Grundler, “*Mode localization transition in ferromagnetic microscopic rings*”, Phys. Rev. B **76**, 014431 (2007).
- [33] J. Stöhr and H. C. Siegbahn, “*Magnetism: From Fundamentals to Nanoscale Dynamics*”, Springer-Verlag Berlin Heidelberg (2006).
- [34] A. Hubert and R. Schäfer, “*Magnetic Domains: The Analysis of Magnetic Microstructures*”, Springer-Verlag Berlin Heidelberg 1998 (Corrected, 3rd Printing 2009).
- [35] H. Kronmüller and M. Fähnle, “*Micromagnetism and the microstructure of ferromagnetic solids*”, Chap. Magnetic Gibbs free energy, p. 11–39, Cambridge University Press (2003).
- [36] F. Cochran, in *Ultrathin Magnetic Structures II: Measurement Techniques and Novel Magnetic Properties*, Eds. J. A. C. Bland and B. Heinrich, Chap. Light scattering from ultrathin magnetic layers and bilayers, p. 222–257, Springer-Verlag Berlin-Heidelberg (1994).

- [37] B. Hillebrands and G. Güntherodt, in *Ultrathin Magnetic Structures II: Measurement Techniques and Novel Magnetic Properties*, Eds. J. A. C. Bland and B. Heinrich, Chap. Brillouin Light Scattering in Magnetic Superlattices, p. 258–279, Springer-Verlag Berlin-Heidelberg (1994).
- [38] R. C. O’Handley, “*Modern Magnetic Materials: Principles and Applications*”, John Wiley & Sons, Inc., New York, NY, USA (2000).
- [39] L. Landau and E. Lifshitz, “*On the theory of the dispersion of magnetic permeability in ferromagnetic bodies*”, Phys. Z. Sowjet. **8**, 153 (1935).
- [40] T. L. Gilbert, “*A Lagrangian formulation of the gyromagnetic equation of the magnetization field*”, Phys. Rev. **100**, 1243 (1955).
- [41] J. Mallinson, “*On Damped Gyromagnetic Precession*”, IEEE Trans. Magn. **23**, 2003 (1987).
- [42] R. Kikuchi, “*On the Minimum of Magnetization Reversal Time*”, J. Appl. Phys. **27**, 1352 (1956).
- [43] F. Bloch, “*Nuclear Induction*”, Phys. Rev. **70**, 460 (1946).
- [44] N. Bloembergen, E. M. Purcell and R. V. Pound, “*Relaxation Effects in Nuclear Magnetic Resonance Absorption*”, Phys. Rev. **73**, 679 (1948).
- [45] D. Polder, “*On the Quantum Theory of Ferromagnetic Resonance*”, Phys. Rev. **73**, 1116 (1948).
- [46] C. Kittel, “*On the Theory of Ferromagnetic Resonance Absorption*”, Phys. Rev. **73**, 155 (1948).
- [47] B. Heinrich, in *Ultrathin Magnetic Structures III: Fundamentals of Nanomagnetism*, Eds. J. A. C. Bland and B. Heinrich, Chap. Spin Relaxation in Magnetic Metallic Layers and Multilayers, p. 143–210, Springer-Verlag Berlin-Heidelberg (2005).
- [48] S. S. Kalarickal, P. Krivosik, M. Wu, C. E. Patton, M. L. Schneider, P. Kabos, T. J. Silva and J. P. Nibarger, “*Ferromagnetic resonance linewidth in metallic thin films: Comparison of measurement methods*”, J. Appl. Phys. **99**, 093909 (2006).
- [49] J. Smit and H. G. Beljers, “*Ferromagnetic resonance absorption in  $BaFe_{12}O_{19}$ , a highly anisotropic crystal*”, Philips Res. Rep. **10**, 113 (1955).
- [50] H. Suhl, “*Ferromagnetic Resonance in Nickel Ferrite Between One and Two Kilomegacycles*”, Phys. Rev. **97**, 555 (1955).
- [51] L. Baselgia, M. Warden, F. Waldner, S. L. Hutton, J. E. Drumheller, Y. Q. He, P. E. Wigen and M. Maryško, “*Derivation of the resonance frequency from the free energy of ferromagnets*”, Phys. Rev. B **38**, 2237 (1988).

- [52] D. D. Stancil and A. Prabhakar, “*Spin Waves: Theory and Applications*”, Springer Science+Business Media, New York, NY, USA (2009).
- [53] R. C. Fletcher, R. C. LeCraw and E. G. Spencer, “*Electron Spin Relaxation in Ferromagnetic Insulators*”, Phys. Rev. **117**, 955 (1960).
- [54] B. Hillebrands and K. Ounadjela, Eds., “*Spin Dynamics in Confined Magnetic Structures II*”, Springer-Verlag Berlin Heidelberg (2002).
- [55] W. S. Ament and G. T. Rado, “*Electromagnetic Effects of Spin Wave Resonance in Ferromagnetic Metals*”, Phys. Rev. **97**, 1558 (1955).
- [56] C. E. Patton, “*Effective Linewidth due to Porosity and Anisotropy in Polycrystalline Yttrium Iron Garnet and Ca-V-Substituted Yttrium Iron Garnet at 10 GHz*”, Phys. Rev. **179**, 352 (1969).
- [57] M. Sparks, R. Loudon and C. Kittel, “*Ferromagnetic Relaxation. I. Theory of the Relaxation of the Uniform Precession and the Degenerate Spectrum in Insulators at Low Temperatures*”, Phys. Rev. **122**, 791 (1961).
- [58] R. D. McMichael, D. J. Twisselmann, J. E. Bonevich, A. P. Chen, J. W. F. Egelhoff and S. E. Russek, “*Ferromagnetic resonance mode interactions in periodically perturbed films*”, J. Appl. Phys. **91**, 8647 (2002).
- [59] R. D. McMichael, D. J. Twisselmann and A. Kunz, “*Localized Ferromagnetic Resonance in Inhomogeneous Thin Films*”, Phys. Rev. Lett. **90**, 227601 (2003).
- [60] J. Lindner, K. Lenz, E. Kosubek, K. Baberschke, D. Spoddig, R. Meckenstock, J. Pelzl, Z. Frait and D. L. Mills, “*Non-Gilbert-type damping of the magnetic relaxation in ultrathin ferromagnets: Importance of magnon-magnon scattering*”, Phys. Rev. B **68**, 060102 (2003).
- [61] G. Woltersdorf and B. Heinrich, “*Two-magnon scattering in a self-assembled nanoscale network of misfit dislocations*”, Phys. Rev. B **69**, 184417 (2004).
- [62] N. Mo, Y.-Y. Song and C. E. Patton, “*High-field microwave effective linewidth in polycrystalline ferrites: Physical origins and intrinsic limits*”, J. Appl. Phys. **97**, 093901 (2005).
- [63] K. Zakeri, J. Lindner, I. Barsukov, R. Meckenstock, M. Farle, U. von Hörsten, H. Wende, W. Keune, J. Rocker, S. S. Kalarickal, K. Lenz, W. Kuch, K. Baberschke and Z. Frait, “*Spin dynamics in ferromagnets: Gilbert damping and two-magnon scattering*”, Phys. Rev. B **76**, 104416 (2007).
- [64] P. Krivosik, N. Mo, S. Kalarickal and C. E. Patton, “*Hamiltonian formalism for two magnon scattering microwave relaxation: Theory and applications*”, J. Appl. Phys. **101**, 083901 (2007).

- [65] S. S. Kalarickal, N. Mo, P. Krivosik and C. E. Patton, “*Ferromagnetic resonance linewidth mechanisms in polycrystalline ferrites: Role of grain-to-grain and grain-boundary two-magnon scattering processes*”, Phys. Rev. B **79**, 094427 (2009).
- [66] J.-M. Beaujour, D. Ravelosona, I. Tudosa, E. E. Fullerton and A. D. Kent, “*Ferromagnetic resonance linewidth in ultrathin films with perpendicular magnetic anisotropy*”, Phys. Rev. B **80**, 180415 (2009).
- [67] J. Lindner, I. Barsukov, C. Raeder, C. Hassel, O. Posth, R. Meckenstock, P. Landeros and D. L. Mills, “*Two-magnon damping in thin films in case of canted magnetization: Theory versus experiment*”, Phys. Rev. B **80**, 224421 (2009).
- [68] R. P. Erickson and D. L. Mills, “*Magnetic instabilities in ultrathin ferromagnets*”, Phys. Rev. B **46**, 861 (1992).
- [69] R. Arias and D. L. Mills, “*Extrinsic contributions to the ferromagnetic resonance response of ultrathin films*”, Phys. Rev. B **60**, 7395 (1999).
- [70] P. Landeros, R. E. Arias and D. L. Mills, “*Two magnon scattering in ultrathin ferromagnets: The case where the magnetization is out of plane*”, Phys. Rev. B **77**, 214405 (2008).
- [71] D. M. Pozar, “*Microwave Engineering*”, John Wiley & Sons, Inc., Hoboken, NJ, USA (2005).
- [72] M. Kummer, “*Grundlagen der Mikrowellentechnik*”, VEB Verlag Technik Berlin (1989).
- [73] C. P. Wen, “*Coplanar Waveguide: A Surface Strip Transmission Line Suitable for Nonreciprocal Gyromagnetic Device Applications*”, IEEE Trans. Microw. Theory Tech. **17**, 1087 (1969).
- [74] R. N. Simons, “*Coplanar Waveguide Circuits, Components, and Systems*”, John Wiley & Sons, Inc, New York, NY, USA (2001).
- [75] H. Klingbeil and W. Heinrich, “*Calculation of CPW A.C. Resistance and Inductance Using a Quasi-Static Mode-Matching Approach*”, IEEE Trans. Microw. Theory Tech. **42**, 1004 (1994).
- [76] G. E. Ponchak, J. Papapolymerou and M. M. Tentzeris, “*Excitation of Coupled Slotline Mode in Finite-Ground CPW with Unequal Ground-Plane Widths*”, IEEE Trans. Microw. Theory Tech. **53**, 713 (2005).
- [77] K. Bellenhoff and W. Heinrich, “*Excitation of the parasitic parallel-plate line mode at coplanar discontinuities*”, IEEE MTT-S International Microwave Symposium Digest. Vol 3. p. 1789 (1997).



- [78] R. W. Jackson, “*Mode Conversion at Discontinuities in Finite-Width Conductor-Backed Coplanar Waveguide*”, IEEE Trans. Microw. Theory Tech. **37**, 1582 (1989).
- [79] Southwest Microwave, Inc., Optimizing Test Boards for 50 GHz End Launch Connectors, Technical Report (2007).
- [80] V. Milanovic, M. Ozgur, D. C. Degroot, J. A. Jargon, M. Gaitan and M. E. Zaghloul, “*Characterization of Broad-Band Transmission for Coplanar Waveguide on CMOS Silicon Substrates*”, IEEE Trans. Microw. Theory Tech. **46**, 632 (1998).
- [81] F. Ellinger, “*Radio Frequency Integrated Circuits and Technology*”, Springer Verlag Berlin Heidelberg (2008).
- [82] K. Kurokawa, “*Power Waves and the Scattering Matrix*”, IEEE Trans. Microw. Theory Tech. **13**, 194 (1965).
- [83] D. A. Frickey, “*Conversion between S, Z, Y, h, ABCD, and T parameters which are valid for complex load and source impedances*”, IEEE Trans. Microw. Theory Tech. **42**, 205 (1994).
- [84] C. M. Bilzer, “*Microwave susceptibility of thin ferromagnetic films: metrology and insight into magnetization dynamics*”, Ph.D. thesis, Institut d’Electronique Fondamentale, Université Paris-Sud, France (2007).
- [85] G. P. Srivastava and V. L. Gupta, “*Microwave Devices and Circuit Designs*”, Prentice-Hall of India, New Dehli, India (2006).
- [86] Agilent Technologies, E8364-90026 - Service Guide E8362B, E8363B, E8364B Agilent Technologies PNA Series Microwave Network Analyzers, Technical Report (2007).
- [87] Agilent, 5965-7917E - Network Analyzer Basics (2004).
- [88] Agilent Application Note 1287-3, Applying Error Correction to Network Analyzer Measurements (2002).
- [89] Agilent Application Note 1364-1, De-embedding and Embedding S-Parameter Networks Using a Vector Network Analyzer (2004).
- [90] Agilent, Agilent Electronic vs. Mechanical Calibration Kits: Calibration Methods and Accuracy (2003).
- [91] I. Neudecker, “*Magnetization Dynamics of Confined Ferromagnetic Systems*”, Ph.D. thesis, Universität Regensburg (2006).
- [92] O. Karlqvist, “*Calculation of the magnetic field in the ferromagnetic layer of a magnetic drum*”, Trans. R. Inst. Technol. **86**, 3 (1954).

- [93] F. Giesen, “*Magnetization Dynamics of Nanostructured Ferromagnetic Rings and Rectangular Elements*”, Ph.D. thesis, Universität Hamburg, Germany (2005).
- [94] A. M. Nicolson and G. F. Ross, “*Measurement of the Intrinsic Properties of Materials by Time-Domain Techniques*”, IEEE Trans. Instrum. Meas. **19**, 377 (1970).
- [95] W. B. Weir, “*Automatic Measurement of Complex Dielectric Constant and Permeability at Microwave Frequencies*”, Proceedings of the IEEE **62**, 33 (1974).
- [96] W. Barry, “*A Broad-Band, Automated, Stripline Technique for the Simultaneous Measurement of Complex Permittivity and Permeability*”, IEEE Trans. Microw. Theory Tech. **34**, 80 (1986).
- [97] L. F. Chen, C. K. Ong, C. P. Neo and V. V. Varadan, “*Microwave Electronics: Measurement and Materials Characterization*”, John Wiley & Sons Ltd., Chichester, England (2004).
- [98] J. Baker-Jarvis, E. J. Vanzura and W. A. Kissick, “*Improved Technique for Determining Complex Permeability with Transmission/Reflection Method*”, IEEE Trans. Microw. Theory Tech. **38**, 1096 (1990).
- [99] A.-H. Boughriet, C. Legrand and A. Chapoton, “*Noniterative Stable Transmission/Reflection Method for Low-Loss Material Complex Permittivity Determination*”, IEEE Trans. Microw. Theory Tech. **45**, 52 (1997).
- [100] S. Stuchly and M. Matuszewski, “*A combined total reflection transmission method in application to dielectric spectroscopy*”, IEEE Trans. Instrum. Meas. **27**, 285 (1978).
- [101] B. K. Kuanr, R. E. Camley and Z. Celinski, “*Extrinsic contribution to Gilbert damping in sputtered NiFe films by ferromagnetic resonance*”, J. Magn. Magn. Mater. **286**, 276 (2005).
- [102] G. Council, J.-V. Kim, T. Devolder, C. Chappert, K. Shigeto and Y. Otani, “*Spin wave contributions to the high-frequency magnetic response of thin films obtained with inductive methods*”, J. Appl. Phys. **95**, 5646 (2004).
- [103] D. Pain, M. Ledieu, O. Acher, A. L. Adenot and F. Duverger, “*An improved permeameter for thin film measurements up to 6 GHz*”, J. Appl. Phys. **85**, 5151 (1999).
- [104] V. Bekker, K. Seemann and H. Leiste, “*A new strip line broad-band measurement evaluation for determining the complex permeability of thin ferromagnetic films*”, J. Magn. Magn. Mater. **270**, 327 (2004).

- [105] P.-M. Jacquarta and L. Roux, “*Influence of the electrical resistivity of a ferromagnetic thin film on its permeability measurement performed with a permeameter*”, J. Magn. Magn. Mater. **281**, 82 (2004).
- [106] M. Ledieu, F. Schoenstein, J.-H. L. Gallou, O. Valls, S. Queste, F. Duverger and O. Acher, “*Microwave permeability spectra of ferromagnetic thin films over a wide range of temperatures*”, J. Appl. Phys. **93**, 7202 (2003).
- [107] E. Moraitakis, L. Kompotiatis, M. Pissas and D. Niarchos, “*Permeability measurements of permalloy films with a broad band stripline technique*”, J. Magn. Magn. Mater. **222**, 168 (2000).
- [108] S. Ingvarsson, G. Xiao, S. S. P. Parkin and R. H. Koch, “*Tunable magnetization damping in transition metal ternary alloys*”, Appl. Phys. Lett. **85**, 4995 (2004).
- [109] E. W. Hill, J. P. Li and J. K. Birtwistle, “*Magnetic and structural properties of permalloy-tantalum multilayer thin films*”, J. Appl. Phys. **69**, 4526 (1991).
- [110] M. Ueno and S. Tanoue, “*Magnetic properties of ion-beam sputter deposited NiFe ultrathin films*”, J. Vac. Sci. Technol. A **13**, 2194 (1995).
- [111] M. Mao, Q. Leng, Y. Huai, P. Johnson, M. Miller, H.-C. Tong, L. Miloslavsky, C. Qian, J. Wang and H. Hegde, “*Characterization of ion beam and magnetron sputtered thin Ta/NiFe films*”, J. Appl. Phys. **85**, 5780 (1999).
- [112] M. Kowalewski, W. H. Butler, N. Moghadam, G. M. Stocks, T. C. Schulthess, K. J. Song, J. R. Thompson, A. S. Arrott, T. Zhu, J. Drewes, R. R. Katti, M. T. McClure and O. Escorcía, “*The effect of Ta on the magnetic thickness of permalloy Ni<sub>81</sub>Fe<sub>19</sub> films*”, J. Appl. Phys. **87**, 5732 (2000).
- [113] N. Y. Moghadam, G. M. Stocks, M. Kowalewski and W. H. Butler, “*Effects of Ta on the magnetic structure of permalloy*”, J. Appl. Phys. **89**, 6886 (2001).
- [114] G. H. Yu, H. C. Zhao, M. H. Li, F. W. Zhu and W. Y. Lai, “*Interface reaction of Ta/Ni<sub>81</sub>Fe<sub>19</sub> or Ni<sub>81</sub>Fe<sub>19</sub>/Ta and its suppression*”, Appl. Phys. Lett. **80**, 455 (2002).
- [115] H. Hurdequint, “*FMR studies of single permalloy layers sandwiched by Au*”, J. Magn. Magn. Mater. **310**, 2061 (2006).
- [116] N. Y. Moghadam and G. M. Stocks, “*Magnetic structure of Ni-rich Ni<sub>1-x</sub>Ta<sub>x</sub> and Py-Ta alloys*”, Phys. Rev. B **71**, 134421 (2005).
- [117] C. T. Rettner, S. Anders, T. Thomson, M. Albrecht, Y. Ikeda, M. E. Best and B. D. Terris, “*Magnetic characterization and recording properties of patterned Co<sub>70</sub>Cr<sub>18</sub>Pt<sub>12</sub> perpendicular media*”, IEEE Trans. Magn. **38**, 1725 (2002).
- [118] D. McGrouther and J. N. Chapman, “*Nanopatterning of a thin ferromagnetic CoFe film by focused-ion-beam irradiation*”, Appl. Phys. Lett. **87**, 022507 (2005).

- [119] J. F. Ziegler, J. P. Biersack and U. Littmark, “*The Stopping and Range of Ions in Matter*”, Vol. 1, Pergamon Press New York (1985), The SRIM code is available at <http://www.srim.org>.
- [120] W. Möller, W. Eckstein and J. P. Biersack, “*Tridyn-binary collision simulation of atomic collisions and dynamic composition changes in solids*”, Comput. Phys. Commun. **51**, 355 (1988).
- [121] J. Fassbender, A. Mücklich, K. Potzger and W. Möller, “*Mixing and subsequent amorphization of ultrathin  $Ni_{81}Fe_{19}/Ta$  bilayers by 30 keV Ni implantation*”, Nucl. Instrum. Meth. B **248**, 343 (2006).
- [122] B. X. Liu and Z. J. Zhang, “*Formation of nonequilibrium solid phases by ion irradiation in the Ni-Ta system and their thermodynamic and growth-kinetics interpretations*”, Phys. Rev. B **49**, 12519 (1994).
- [123] B. X. Liu, W. S. Lai and Q. Zhang, “*Irradiation induced amorphization in metallic multilayers and calculation of glass-forming ability from atomistic potential in the binary metal systems*”, Mater. Sci. Eng. **29**, 1 (2000).
- [124] B. X. Liu, Z. C. Li and H. R. Gong, “*Thermodynamic and atomistic modeling of irradiation-induced amorphization in nanosized metal-metal multilayers*”, Surf. Coat. Technol. **196**, 2 (2005).
- [125] K. Lenz, E. Kosubek, K. Baberschke, H. Wende, J. Herfort, H.-P. Schönherr and K. H. Ploog, “*Magnetic properties of  $Fe_3Si/GaAs(001)$  hybrid structures*”, Phys. Rev. B **72**, 144411 (2005).
- [126] J. P. Nibarger, R. Lopusnik, Z. Celinski and T. J. Silva, “*Variation of magnetization and the Landé  $g$  factor with thickness in Ni-Fe films*”, Appl. Phys. Lett. **83**, 93 (2003).

# Publications

## Articles

- **Measuring the Saturation Magnetization in Samples with Unknown Magnetic Volume**  
D. Markó, K. Lenz, T. Strache, R. Kaltofen, and J. Fassbender  
[IEEE Trans. Mag. 46, 1711 \(2010\)](#)  
DOI:10.1109/TMAG.2010.2040141
- **Photon Counting System for Time-resolved Experiments in Multi-bunch Mode**  
A. Puzic, T. Korhonen, B. Kalantari, J. Raabe, C. Quitmann, P. Jüllig, L. Bommer, D. Goll, G. Schütz, S. Wintz, T. Strache, M. Körner, D. Markó, C. Bunce, and J. Fassbender  
[Synchrotron Radiation News 23, 26 \(2010\)](#)  
DOI:10.1080/08940881003702056
- **Determination of the Saturation Magnetization of Ion Irradiated Py/Ta samples using Polar Magneto-Optical Kerr Effect and Ferromagnetic Resonance**  
D. Markó, T. Strache, K. Lenz, J. Fassbender, and R. Kaltofen  
[Appl. Phys. Lett. 96, 022530 \(2010\)](#)  
DOI:10.1063/1.3291051
- **Introducing artificial length scales to tailor magnetic properties**  
J. Fassbender, T. Strache, M. O. Liedke, D. Markó, S. Wintz, K. Lenz, A. Keller, S. Facsko, I. Mönch, and J. McCord  
[New Journal of Physics 11, 125002 \(2009\)](#)  
DOI:10.1088/1367-2630/11/12/125002
- **Paramagnetism in Co-doped ZnO films**  
Q. Xu, S. Zhou, D. Markó, K. Potzger, J. Fassbender, M. Vinnichenko, M. Helm, H. Hochmuth, M. Lorenz, M. Grundmann, and H. Schmidt  
[J. Phys. D: Appl. Phys. 42, 085001 \(2009\)](#)  
DOI:10.1088/0022-3727/42/8/085001
- **Spinel ferrite nanocrystals embedded inside ZnO: Magnetic, electronic, and magnetotransport properties**  
S. Zhou, K. Potzger, Q. Xu, K. Küpper, G. Talut, D. Markó, A. Mücklich, M. Helm, J. Fassbender, E. Arenholz, and H. Schmidt  
[Phys. Rev. B 80, 094409 \(2009\)](#)  
DOI:10.1103/PhysRevB.80.094409

## Talks

- J. Fassbender, M. O. Liedke, M. Körner, **D. Markó**, K. Lenz, and S. Facsko, “*Ion-erosion-induced pattern as templates for layers with magnetic anisotropy and coupling*”, Joint European Magnetic Symposia JEMS 2010, Symposium “Surfaces and Interfaces of Magnetic Thin Films”, August 23 – 28, 2010, Kraków, Poland
- J. Fassbender, T. Strache, **D. Markó**, S. Wintz, K. Lenz, A. Keller, S. Facsko, and J. McCord, “*Nanomagnets – created and tailored by ions*”, 6<sup>th</sup> Nanoscience and Nanotechnology Conference, June 15 – 18, 2010, Izmir, Turkey
- K. Lenz, **D. Markó**, T. Strache, R. Kaltofen, and J. Fassbender, “*Determination of the Saturation Magnetization from Perpendicular Magnetic Anisotropy Measurements of Ion Irradiated Multilayers*”, 11<sup>th</sup> Joint MMM-Intermag Conference, January 18 – 22, 2010, Washington, DC, USA
- K. Lenz, **D. Markó**, T. Strache, and J. Fassbender, “*Spin wave excitations: coupling and damping effects in ultrathin films*”, 448<sup>th</sup> WE-Heraeus-Seminar: Excitement in magnetism: Spin-dependent scattering and coupling of excitations in ferromagnets, November 22 – 25, 2009, Ringberg, Germany
- J. Fassbender, M. O. Liedke, M. Körner, **D. Markó**, K. Lenz, and S. Facsko, “*Ion-erosion-induced pattern as templates for layers with magnetic anisotropy and coupling*”, MRS Fall Meeting, November 30 – December 04, 2009, Boston, MA, USA
- J. Fassbender, M. O. Liedke, T. Strache, **D. Markó**, K. Lenz, A. Keller, S. Facsko, S. Tibus, F. Springer, M. Albrecht, and H. Rohrmann, “*Periodically modulated surfaces and interfaces: Introducing artificial length scales to tailor magnetic properties*”, 2<sup>nd</sup> International Conference on Physics at Surfaces and Interfaces, February 23 – 27, 2009, Puri, Orissa, India and Symposium “Ion Beams and Nano-Engineering”, MRS Spring Meeting, April 13 – 17, 2009, San Francisco, CA, USA
- T. Strache, L. Reichel, S. Wintz, M. Fritzsche, I. Mönch, J. Raabe, N. Martin, J. McCord, M. Körner, **D. Markó**, F. Romstedt, and J. Fassbender, “*Ion irradiation of permalloy: From thin magnetic films to lateral exchange spring nanostructures*”, Workshop Ionenstrahlphysik, April 06 – 08, 2009, Friedrich-Schiller-Universität Jena, Jena, Germany
- **D. Markó**, T. Strache, K. Lenz, J. Fassbender, and R. Kaltofen, “*Ion Irradiation Induced Modification of Magnetic Properties in Py-Ta-Multilayers*”, DPG Spring Meeting of the Condensed Matter Section, March 22 – 27, 2009, Dresden, Germany
- M. O. Liedke, B. Liedke, **D. Markó**, A. Keller, A. Mücklich, S. Facsko, J. Fassbender, E. Cizmar, S. Zvyagin, and J. Wosnitza, “*Magnetic anisotropies*”

*in ferromagnetic and exchange-coupled systems on rippled surfaces*”, DPG Spring Meeting of the Condensed Matter Section, February 25 – 29, 2008, Berlin, Germany

- J. Fassbender, M. O. Liedke, A. Keller, S. Facsko, **D. Markó**, A. Hanisch, J. Grenzer, E. Cizmar, and S. Zvyagin, “*Self-organized surface ripples as a source of magnetic anisotropies*”, DPG Spring Meeting of the Condensed Matter Section, February 25 – 29, 2008, Berlin, Germany
- M. O. Liedke, V. Cantelli, J. Grenzer, **D. Markó**, A. Mücklich, and J. Fassbender, “*The strong correlation between structural properties of the buffer layer and the exchange bias phenomena*”, DPG Spring Meeting of the Condensed Matter Section, February 25 – 29, 2008, Berlin, Germany
- K. Küpper, **D. Markó**, M. Buess, J. Raabe, C. Quitmann, and J. Fassbender, “*Magnetization dynamics of a single cross-tie wall*”, DPG Spring Meeting of the Condensed Matter Section, March 26 – 30, 2007, Regensburg, Germany

## Posters

- S. Wintz, A. Puzic, T. Strache, M. Körner, C. Bunce, **D. Markó**, J. Grebing, M. Fritzsche, I. Mönch, R. Mattheis, A. Erbe, J. Raabe, C. Quitmann, and J. Fassbender, “*Magnetization Dynamics of Coupled Vortices*”, MML 2010 - IEEE 7<sup>th</sup> International Symposium on Magnetic Multilayers, September 19 – 24, 2010, Berkeley, CA, USA
- K. Lenz, **D. Markó**, T. Strache, and J. Fassbender, “*Determination of the Saturation Magnetization from Perpendicular Magnetic Anisotropy Measurements*”, Advances in Magnetic Nanostructures, September 04 – 09, 2009, Vail, CO, USA
- **D. Markó**, K. Potzger, K. Küpper, Q. Xu, S. Zhou, H. Schmidt, J. Fassbender, M. Lorenz, E. Arenholz, and J. D. Denlinger, “*Determination of charge state in Co- and Mn-doped ZnO films*”, DPG Spring Meeting of the Condensed Matter Section, February 25 – 29, 2008, Berlin, Germany





# Acknowledgements

Last but not least, I want to thank everyone who contributed to this work in terms of sample preparation, measurements, simulations, or any other kind of support. In particular I would like to thank:

- Prof. Dr. Jürgen Faßbender for giving me the opportunity to pursue my Ph.D. at the FZD, for his interest in my work, and for making the construction of the VNA-FMR setups possible without financial restrictions
- Prof. Dr. Jochen Wosnitza for being referee of my dissertation
- Dr. Kilian Lenz, my supervisor, who arrived at the right time at the FZD and does not only know everything about FMR, but about Corel Draw and L<sup>A</sup>T<sub>E</sub>X as well
- Dr. Karsten Küpper for his supervision during the first one and a half years and for introducing me into the world of synchrotron radiation
- Andreas Henschke, who was an invaluable help for the construction of the final VNA-FMR Setup 2 and made sure, that it does not only work as intended and looks good, but also complies with all safety rules
- Thomas Strache for performing the MOKE measurements as well as the TRIDYN simulations
- Matthias Wieser for writing the control and automation software of the two VNA-FMR setups during his internship
- David Ball and Michael Körner for writing the new version of the conversion software as well as the fitting software
- Dr. Jörg Grenzer for his assistance with all things related to microwave engineering, especially during the early stage of my thesis
- Rainer Kaltoven for preparing the Py/Ta samples
- Ingolf Winkler for the ion irradiation
- Dr. Arndt Mücklich for the TEM investigations
- Mykhaylo Ozerov and Dr. Sergei Zvyagin for the X-band FMR measurements
- Sebastian Wintz for regularly supplying me with Clif bars and the world's greatest cookies from Berkeley Bowl

Additionally, I would like to remark, that enjoying and profiting from the friendly and cooperative atmosphere within the old and new FWIN division was a great pleasure.

Financial support from the DFG (Grant No. FA 314/3-1) is gratefully acknowledged.

Finally, many thanks are addressed to my parents for their continuous support.

# Erklärung

Diese Dissertation wurde am Institut für Ionenstrahlphysik und Materialforschung des Forschungszentrums Dresden-Rossendorf e.V. unter wissenschaftlicher Betreuung von Prof. Dr. Jürgen Faßbender angefertigt.

Hiermit versichere ich, dass ich die vorliegende Arbeit ohne unzulässige Hilfe Dritter und ohne Benutzung anderer als der angegebenen Hilfsmittel angefertigt habe; die aus fremden Quellen direkt oder indirekt übernommenen Gedanken sind als solche kenntlich gemacht. Die Arbeit wurde bisher weder im Inland noch im Ausland in gleicher oder ähnlicher Form einer anderen Prüfungsbehörde vorgelegt.

Ich versichere weiterhin, dass bislang keine Promotionsverfahren stattgefunden haben.

Ich erkenne die Promotionsordnung der Fakultät Mathematik und Naturwissenschaften an der Technischen Universität Dresden vom 20.03.2000, in der Fassung der vom Fakultätsrat am 19.06.2002 und 12.07.2002 beschlossenen und mit Erlass des Sächsischen Staatsministeriums für Wissenschaft und Kunst vom 18.03.2003 genehmigten Änderungen gemäß Satzung vom 16.04.2003 sowie gemäß der Änderungssatzung vom 17.07.2008, an.

Daniel Markó  
Dresden, den 17.08.2010